University of Alberta

Direct simulations of spherical particle motion in non-Newtonian liquids

by

Prashant

A thesis submitted to the Faculty of Graduate Studies and Research
in partial fulfillment of the requirements for the degree of

Master of Science
in
Chemical Engineering

Department of Chemical and Materials Engineering

Fall 2009

Edmonton, Alberta

Examining Committee

Dr. Jos Derksen, Chemical and Materials Engineering

Dr. Natalia Semagina, Chemical and Materials Engineering

Dr. Sean Sanders, Chemical and Materials Engineering

Dr. Carlos F. Lange, Mechanical Engineering

Dedicated to

My parents

Abstract

The present work deals with the development of a direct simulation strategy for solving the motion of spherical particles in non-Newtonian liquids. The purely viscous (non-elastic) non-Newtonian liquids are described by Bingham and thixotropy models. Validation of the strategy is performed for single phase (lid driven cavity flow) and two phase flows (sphere sedimentation). Lid driven cavity flow results illustrate the flow evolution of thixotropic liquid and subtle differences between thixotropic rheology and pseudo Bingham rheology. Single sphere sedimentation in Bingham liquid is shown to be influenced by the yield stress of the liquid. Time-dependent properties such as aging prominently affect the settling of a sphere in thixotropic liquid. The hydrodynamic interactions between two spheres are also studied at low and moderate Reynolds numbers. In thixotropic liquid, an intriguing phenomenon is observed where the separation distance between the spheres first increases and then rapidly decreases.

Acknowledgement

> In ordinary life we hardly realize that we receive a great deal more than we give, and that it is only with gratitude that life becomes rich. It is very easy to overestimate the importance of our achievements in comparison with what we owe others.
>
> *Dietrich Bonhoeffer*

I wish to wholeheartedly thank my mentor and supervisor Dr. J. J. Derksen for his guidance, ideas and supportive nature throughout this research degree. Working with a dedicated expert and good individual like him has been a great learning experience of my life.

I also want to thank my friend and fellow colleague Srinath Madhavan who was always there to discuss and help me in understanding the concepts of computational fluid dynamics. I would also like to thank my colleagues Elorm Sekyi and Mrinal Jain for all the helpful discussions and comments. I also want to acknowledge Bob Barton and Jack Gibeau for their help with department computing facilities. Thanks to all of my friends for their best wishes. Financial support from Chemical & Materials Engineering department is sincerely appreciated.

Probably words are not enough to thank my family members for their unconditional love, support and encouragement. Thank you mom, dad, didi and jija ji to let me go down the road I wanted. A special thanks to my little nephews Anku and Chinku whose innocent talks are one of the major sources of my happiness.

Contents

List of Tables

List of Figures

List of Symbols

Bn	Bingham number [-]
Bn_s	Bingham number based on Stokes velocity [-]
Bn_T	Bingham number based on terminal velocity [-]
C_d	Drag coefficient [-]
$\mathbf{c}_i$	velocity vector in ith direction $[m.s^{-1}]$
D	Drag force $[kg.m.s^{-2}]$
d	diameter of sphere $[m]$
d_{ij}	deformation rate tensor [-]
Db	purely viscous Deborah number [-]
e	mathematical constant [-]
$\mathbf{f}$	external force vector $[kg.m.s^{-2}]$
f_0	external body force $[kg.m.s^{-2}]$
F_B	buoyancy force on single sphere $[kg.m.s^{-2}]$
F_D	drag force on single sphere $[kg.m.s^{-2}]$
$F_D^{'}$	drag force on sphere doublet $[kg.m.s^{-2}]$
F_G	force due to gravity on single sphere $[kg.m.s^{-2}]$

F_W	force on single sphere due to wall effects $[kg.m.s^{-2}]$
$F_W^{'}$	force on sphere doublet due to wall effects $[kg.m.s^{-2}]$
g	gravitational acceleration $[m.s^{-2}]$
H	distance $[m]$
k_1	thixotropic parameter [-]
k_2	thixotropic parameter/inverse time scale $[t^{-1}]$
L	side of a square cross section $[m]$
m_i	weight factor for ith direction [-]
$N_i(\mathbf{x}, t)$	dimensionless mass density in ith direction [-]
P	pressure $[kg.m^{-1}.s^{-2}]$
Re_s	Reynolds number based on Stokes velocity [-]
Re_T	Reynolds number based on terminal velocity [-]
t	time $[t]$
$\mathbf{u}$	velocity vector $[m.s^{-1}]$
u_0	lid velocity $[m.s^{-1}]$
U_1	terminal velocity of single sphere in finite size medium $[m.s^{-1}]$
$U_{1\infty}$	terminal velocity of single sphere in unbounded medium $[m.s^{-1}]$
U_2	terminal velocity of sphere doublet in finite size medium $[m.s^{-1}]$
$U_{2\infty}$	terminal velocity of sphere doublet in unbounded medium $[m.s^{-1}]$
U_c	characteristic velocity $[m.s^{-1}]$
U_∞	terminal velocity in an unbounded medium $[m.s^{-1}]$

U_s	Stokes velocity $[m.s^{-1}]$
U_w	terminal velocity in a bounded medium $[m.s^{-1}]$
U_x	velocity in x direction $[m.s^{-1}]$
V	terminal velocity $[m.s^{-1}]$
v_r	velocity ratio [-]
V_{tr}	average terminal velocity of the trailing sphere in two sphere settling $[m.s^{-1}]$
W	Separation distance between the centers of spheres $[m]$
$\mathbf{x}$	position vector $[m]$
x, y, z	cartesian coordinates [-]
α	thixotropic parameter/viscosity ratio [-]
$\beta_k^{\pm}$	solution vector [-]
δ	correction factor [-]
$\dot{\gamma}$	shear rate $[t^{-1}]$
$\dot{\gamma}_c$	critical shear rate $[t^{-1}]$
κ	a proportionality constant $[kg.s^{-2}]$
λ	scalar network parameter [-]
λ_{ss}	steady state network parameter [-]
μ	dynamic viscosity $[kg.m^{-1}.s^{-1}]$
μ_0	zero shear viscosity $[kg.m^{-1}.s^{-1}]$
μ_a	apparent viscosity $[kg.m^{-1}.s^{-1}]$
μ_∞	infinite shear viscosity $[kg.m^{-1}.s^{-1}]$

μ_p	plastic viscosity $[kg.m^{-1}.s^{-1}]$
μ_r	viscosity ratio $[kg.m^{-1}.s^{-1}]$
μ_{ss}	steady state viscosity $[kg.m^{-1}.s^{-1}]$
ν	kinematic viscosity $[m^2.s^{-1}]$
ν_0	zero shear kinematic viscosity $[m^2.s^{-1}]$
ν_p	plastic kinematic viscosity $[m^2.s^{-1}]$
Ω_i	mass density collision operator in ith direction $[t^{-1}]$
ρ	density $[kg.m^{-3}]$
ρ_l	density of liquid $[kg.m^{-3}]$
ρ_s	density of solid sphere $[kg.m^{-3}]$
ψ	stream function $[m^2.s^{-1}]$
σ_{ij}	stress tensor [-]
ψ^*	dimensionless stream function [-]
τ	shear stress $[kg.m^{-1}.s^{-2}]$
τ_0	yield stress of a liquid $[kg.m^{-1}.s^{-2}]$
τ_{ij}	deviatoric part of stress tensor $[kg.m^{-1}.s^{-2}]$

Chapter 1

Introduction

1.1 Project concept

Multiphase flows represent a wide range of flow conditions and applications in present world. They can be classified according to the physical state of the components such as liquid-gas, solid-gas and solid-liquid. Slurry flows, hydrotransport, sedimentation, fluidization and particulate conveying are the prime examples of solid-liquid multiphase flows. Other examples of solid-liquid flows found in nature include quicksand, silt carried by a river and avalanches. Gravitational settling, used as method of separation, is an important aspect of many industrial processes. Sometimes the objective is to recover the solid particles from liquid and other times to extract the liquid (such as water) so that it can be reused in the process.

There are ample applications of solid-liquid suspensions in oil sands industry. The hot water process, most general process used in industry to extract bitumen from the oil sands, involves the use of hot water which has a tendency to activate the clay particles originally found in oil sand [1]. These activated clay particles combine together and make a card house like structure. This card house like structure coupled with water gives rise to a network which exhibit complex rheological behavior similar to time-dependent non-Newtonian liquids. This multiphase mixture possesses a yield stress which influences the design, operation and efficiency of oil sands processing, especially in those parts of

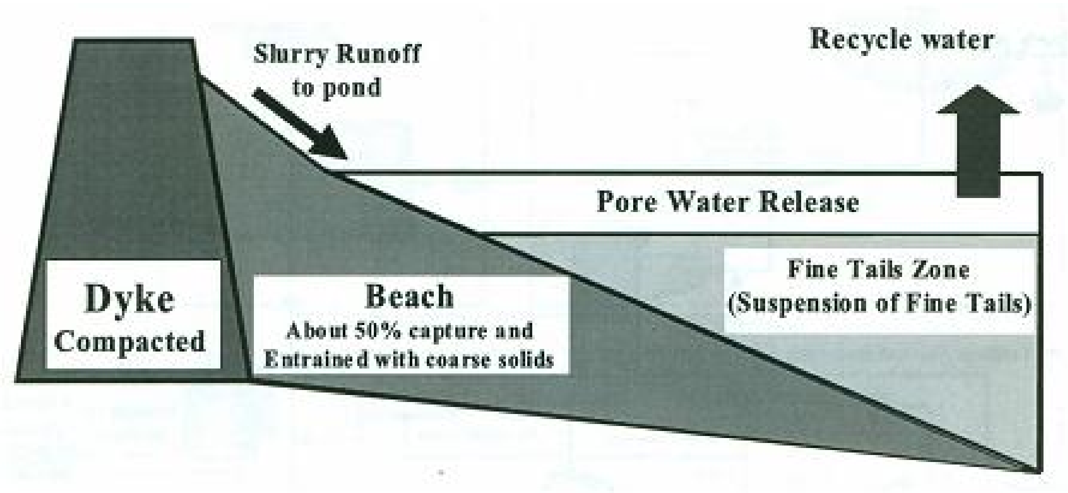

Figure 1.1: Schematic of the oil sands tailings suspensions (Mikula et al. [2])

the process related to separation and to tailings (process residuals).

The process residuals dumped to tailings pond contain sand particles, clay, water and residual bitumen mainly. When the tailings stream is dumped, the coarse solid particles segregate quickly and form a dyke and beach (refer to Figure 1.1), while the remaining slurry consisting of finer particles and residual bitumen flows over the already formed beach. For initial few days, a faster settling of particles takes place, creating a free water zone at the top. However after initial rapid settling, the suspension develops a consistency with time exhibiting non-Newtonian properties (Sheeran [2]). This suspension is usually known as mature fine tails (MFT) which has very high viscosity with high yield stress (Mackinnon [3]). If the net gravity force acting on the fine particles are not enough to overcome the yield stress, sand particles and/or bitumen droplets are trapped into the clay network hindering the gravity based separation. In practical conditions, consolidation rate of MFT is very slow therefore it remains in that state for decades (Kasperski [4]) which is a major environmental issue due to the problem associated with land reclamation and recovery of water .

The present work is motivated by the issues related to clay network formation and hindered gravity based separation occurring in oil sands process and concentrates on the motion of particles in non-Newtonian liquids. In order to mimic the network with stable consistency, the clay-water mixture is treated as non-Newtonian liquid. The inert particles (usually sand particles) are considered explicitly and their sedimentation in the clay network is the focal point of this thesis. In the simulations, the physics of a solid particle is governed by the net gravity and hydrodynamics forces (particularly drag) acting on it. Throughout this work, the particles are treated as solid spheres for convenience.

1.2 Literature review

The sedimentation of particles through Newtonian liquid has been exhaustively researched with theoretical, experimental and numerical studies easily available in literature. However research activities concentrating on sedimentation of multi-particles and of clusters of particles in non-Newtonian liquids are a matter of few studies. The past three to four decades have seen an increased interest in research activities related to non-Newtonian solid-liquid suspensions due to two basic reasons. First is the development of various industries like polymer, oil sands and petroleum where behavior of non-Newtonian solid-liquid suspensions is critical to the growth of respective industry. The second reason is the tremendous growth in computing power coupled with development of ingenious numerical methods. Here, first we provide a brief overview of studies based on solid-liquid suspensions with viscoelastic liquids and later we explore the same with purely viscous liquids.

In 1977, Caswell [5] theoretically examined the sedimentation of two spheres in a viscoelastic liquid and reported that attraction or separation of two spheres depends upon the chosen liquid's parameters and initial separation distance between the spheres. This behavior was experimentally confirmed by Riddle et al. [6]. Allen and Uhlherr [7] conducted an experimental study of sedimentation of particles in moderately shear-thinning viscoelastic fluids and reported the aggregation of settling particles. Similar results were reported by Bobroff and Phillips [8] who experimentally examined the sedimentation of concentrated, non-colloidal suspensions in viscoelastic fluids in the viscous flow regime. They observed that apart from catalyzing the aggregative sedimentation, shear-thinning and elastic properties of liquids could cause time-dependent settling velocity. Joseph et al. [9] studied the sedimentation of two spheres with small side-by-side separation distance and reported an attraction between the spheres which resulted in chaining of spheres. Qualitatively similar chain formation of particles sedimenting in non-Newtonian viscoelastic media have been reported by Singh et al. [10] and Patankar and Hu [11]. Recently Phillips and Talini [12] proposed an asymptotic theory based on multipole expansions to represent weak hydrodynamic interactions between widely separated particles sedimenting in a viscoelastic liquid and predicted that the distant particles above, below and at similar vertical positions attract each other during settling process.

Moving on to solid-liquid suspension studies with purely viscous liquids, Kawase and Ulbrecht [13] predicted the settling velocity of suspensions of spheres in power-law fluids by employing free surface cell model. However as pointed out by Chabbra [14], their solution obtained with $n = 1$ deviated from the well-established results for Newtonian fluids. Chabbra et al. [15] experimentally examined the hindered settling velocity of particle suspensions in power-law liquids as a function of particle size, concentration, and the liquid rheology ($n \geq 0.8$). Jaiswal et al. [16] used free surface cell model to obtain the theoretical solution of creeping flow of power law liquids through assemblages of spherical particles. Their theoretical predictions of the total drag coefficient were satisfactory in the range of $1 \geq n \geq 0.6$. Other notable studies related to solid-liquid suspension in power law based shear-thinning liquids include Zhu and Clark [17], Daugan et al. [18, 19], Zhu et al. [20] and Huang et al. [21].

Hydrodynamic interaction of two or more particles in non-Newtonian liquids possessing yield stress is a matter of recent research and was tackled numerically by Liu et al. [22] and later Merkak et al. [23], Peng et al. [24] and Yu et al. [25], all using time-independent rheologies. Similarly the motion of solid particles through thixotropic liquids has received extensive attention in recent experimental/numerical work (Ferroir et al. [26], Gueslin et al. [27, 28], Yu et al. [29] and Tabuteau et al. [30]) which demonstrate the sedimentation velocities of spherical particles as a function of time or distance traveled and the hydrodynamic interaction between the spherical particles.

1.3 Thesis outline

Chapter 2 provides an introduction to the numerical flow solver (lattice-Boltzmann method) and non-Newtonian liquid models used in this research. We describe the constitutive equations and implementation of lattice-Boltzmann method and non-Newtonian liquid models.

Chapter 3 is devoted to the validation of numerical procedure by testing it against two benchmark problems, namely channel flow and lid driven cavity flow. Since thixotropic liquid exhibits a complex time-dependent rheological behavior, initially the simulations were performed for comparatively easier to understand time-independent Bingham rheology. Later in the chapter we extend the scope of study by performing the simulations with a thixotropic liquid.

In chapter 4, we test our simulation tool for two phase systems, studying the sedimentation of a single spherical particle in non-Newtonian liquids. In order to build credibility, first the validation is done for sphere sedimentation in a Newtonian liquid. Further we study the cases of Bingham liquid flow past a fixed sphere and the sedimentation of a sphere in Bingham liquid. The last study in this chapter discusses single sphere sedimentation in a thixotropic liquid. In this we study the effect of aging and Reynolds number on the sedimentation of a sphere.

Taking the complexity of two phase system to next level, we then examined the motion of two spheres (one above the other) in Newtonian and non-Newtonian liquids at low and moderate Reynolds numbers (chapter 5). The first study in this chapter is devoted to the hydrodynamic interaction of two spheres sedimenting in a Newtonian liquid at low and moderate Reynolds number. At low Reynolds numbers two spheres are found to move with equal velocity while at moderate Reynolds number, the trailing sphere moves faster than the leading sphere. Further we consider the sedimentation of two spheres in Bingham liquid at low and moderate Reynolds numbers and show the same qualitative behavior as observed with Newtonian liquid. Finally the study of two spheres sedimentation in thixotropic liquid is performed with two different Reynolds number and an intriguing behavior is observed with both Reynolds numbers. We explain this intriguing behavior by considering the effect of various properties of thixotropic liquids (yield stress, memory and shear-thinning) at different time periods.

The final chapter of this thesis is devoted to concluding remarks and consists of a brief discussion of results and proposed directions for future work.

Bibliography

[1] J. Masliyah, Z. J. Zhou, Z. Xu, J. Czarnecki, H. Hamza, Understanding water-based bitumen extraction from Athabasca oil sands, *Can. J. Chem. Eng.*, 82 (2004) 628.

[2] R. J. Mikula, K. L. Kasperski, K. L. Burns, R. D. MacKinnon, M. D. MacKinnon, Nature of fate of oil sands fine tailings, in *Advances in chemistry series 251, Suspensions: Fundamentals and applications in the petroleum industry*, L. L. Schramm, Ed., (1996) 677.

[3] D. Sheeran, An improved understanding of fine tailings structure and behavior, *Oil Sands - Our petroleum future conference, Proceedings of the fine tailings symposium*, J. K. Liu, Ed., Edmonton (1993).

[4] M. Mackinnon, Development of the tailings pond at Syncrude's oil sands plant: 1978-1987, *AOSTRA J. of Research*, 5 (1989) 109.

[5] K. L. Kasperski, A review of properties and treatment of oil sands tailings, *J. Research*, 8 (1992) 11.

[6] B. Caswell, Sedimentation of particles in non-Newtonian fluids, *The Mechanics of Viscoelastic Fluids*, Rivlin, R.S., Ed., ASME, AMD, 22 (1977) 19.

[7] M. J. Riddle, C. Narvaez, R. B. Bird, Interactions between two spheres falling along their line of centers in a viscoelastic fluid, *J. Non-Newt. Fluid Mech.*, 2 (1977) 23.

[8] E. Allen, P. H. T. Uhlherr, Non-homogeneous sedimentation in viscoelastic fluids, *J. Rheol.*, 33 (1989) 627.

[9] S. Bobroff, R. J. Phillips, NMR imaging investigation of sedimentation of concentrated suspensions in non-Newtonian fluids, *J. Rheol.*, 42 (1998) 1419.

[10] D. D. Joseph, Y. J. Liu, M. Poletto, J. Feng, Aggregation and dispersion of spheres falling in viscoelastic liquids, *J. Non-Newt. Fluid Mech.*, 54 (1994) 45.

[11] P. Singh, D.D. Joseph, T.I. Hesla, R. Glowinski, T.-W. Pan, A distributed Lagrange multiplier/fictitious domain method for viscoelastic particulate flows, *J. Non-Newtonian Fluid Mech.*, 91 (2000) 165.

[12] N. A. Patankar, H. H. Hu, Rheology of a suspension of particles in viscoelastic fluids, *J. Non-Newt. Fluid Mech.*, 96 (2001) 427.

[13] R. J. Phillips, L. Talini, Chaining of weakly interacting particles suspended in viscoelastic fluids, *J. Non-Newt. Fluid Mech.*, 147 (2007) 175.

[14] Y. Kawase, J. Ulbrecht, Sedimentation of particles in non-Newtonian fluids, *Chem. Eng. Commun.*, 13 (1981) 55.

[15] R. P. Chabbra, Bubbles, drops and particles in non-Newtonian fluids, *CRC Press Inc.* (1993).

[16] R. P. Chhabra, A. Unnikrishnan, V. R. U. Nair, Hindered settling in non-Newtonian power law liquids, *Canadian J. Chem. Eng.*, 70 (1992) 716.

[17] A. K. Jaiswal, T. Sundararajan, R. P. Chhabra, Hydrodynamics of creeping flow of power law fluids through particle assemblages, *Inter. J. Eng. Sci.*, 31 (1993) 293.

[18] Q. Zhu, P. E. Clark, Wall effects in multiparticle settling, *Rheology and Fluid Mechanics of non-Newtonian Materials (ASME) FED*, 246 (1998) 7.

[19] S. Daugan, L. Talini, B. Herzhaft, C. Allain, Aggregation of particles settling in shear-thinning fluids. Part 1. Two particle aggregation, *Eur. Phys. J.*, 7 (2002a) 73.

[20] S. Daugan, L. Talini, B. Herzhaft, C. Allain, Aggregation of particles settling in shear-thinning fluids. Part 2. Three-particle aggregation, *Eur. Phys. J.*, 9 (2002b) 55.

[21] C. Zhu, K. Lam, H. H. Chu, X. D. Tang, G. L. Liu, Drag forces of interacting spheres in power law fluids, *Mech. Res. Commun.*, 30 (2003) 651.

[22] W. Huang, H. Li, Y. Xu, G. Lian, Hydrodynamic force between two hard spheres tangentially translating in a power law fluid, *Chem. Eng. Sci.*, 61 (2006) 1480.

[23] B. T. Liu, S. J. Muller, M. M. Denn, Interactions of two rigid spheres translating collinearly in creeping flow in a Bingham material, *J. Non-Newt. Fluid Mech.*, 113 (2003) 49.

[24] O. Merkak, L. Jossic, A. Magnin, Spheres and interactions between spheres moving at very low velocities in a yield stress fluid, *J. Non-Newtonian Fluid Mech.*, 133 (2006) 99.

[25] J. Peng, K. Q. Zhu, Drag force of interacting coaxial spheres in viscoplastic fluids, *J. Non-Newtonian Fluid Mech.*, 135 (2006) 83.

[26] Z. Yu, A. Wachs, A fictitious domain method for dynamic simulation of particle sedimentation in Bingham fluids, *J. Non-Newtonian Fluid Mech.*, 145 (2007) 78.

[27] T. Ferroir, H. T. Huynh, X. Chateau, P. Coussot, Motion of a solid object through a pasty (thixotropic) fluid, *Physics of Fluids* 16 (2004) 3.

[28] B. Gueslin, L. Talini, B. Herzhaft, Y. Peysson, C. Allain, Flow induced by a sphere settling in an aging yield-stress fluid, *Physics of Fluid* 18 (2006) 103101-1.

[29] B. Gueslin, L. Talini, B. Herzhaft, Y. Peysson, C. Allain, Aggregation behavior of two spheres falling through an aging fluid, *Physical Review E*, 74 (2006) 042501-1.

[30] Z. Yu, A. Wachs, Y. Peysson, Numerical simulations of particle sedimentation in shear-thinning fluids with a fictitious domain method, *J. Non-Newtonian Fluid Mech.*, 136 (2006) 126.

[31] H. Tabuteau, P. Coussot, J. R. de Bruyn, Drag force on a sphere in steady motion through a yield-stress fluid, *J. Rheol.* 51 (2007) 125.

Chapter 2

Methods and techniques

2.1 Lattice-Boltzmann method

2.1.1 Introduction

Lattice-Boltzmann method (LBM) is a well established and frequently used method for simulating liquid flows. It has a second order accuracy and particularly regarded an efficient flow solver for flows involving interfacial dynamics and complex geometries [1]. The development of LBM is based on molecular dynamics approach where focus is on microscopic level properties. In other numerical methods, like finite element and finite difference, liquid flows are solved by directly discretizing the Navier-Stokes equations while in molecular dynamics each particle is followed. The basic idea of the LBM is to construct a simplified kinetic model which incorporates some essential features of microscopic processes so that the macroscopic averaged properties obey the desired macroscopic equations [1].

LBM is originated from lattice gas automata theory in which particles are distributed on a lattice of nodes. Each particle has certain directions of velocities at each node. At each time step a particle is involved in two sequential processes: streaming and collision. In the streaming process, the particle moves from one node to the nearest node in the direction of its velocity and in collision it interacts with other particles reaching at the node and changes its velocity as per collision rule (see Figure 2.1). For computation many possible lattices can be used, which are discretized over time and space. Hardy et al. [2] proposed a square lattice for studying the flow properties of liquids. Frisch et al.[3] employed a symmetrical hexagonal lattice after finding the importance of symmetry of the lattice for the recovery of Navier-Stokes equations. LBM differs with lattice gas automata by neglecting individual particle motion and particle-particle correlations and focusing on average macroscopic behavior in which dimensionless mass densities are distributed along the velocity directions [4]. This modification also eliminates the problem of statistical noise suffered by lattice gas automata method.

2.1.2 Lattice-Boltzmann equations

We consider a 4D face-centered-hyper-cubic (FCHC) lattice and a 3D projection of that lattice is shown in Figure 2.2. This lattice has 18 possible velocity directions (D3Q18 model). Since it is a 3D projection of a 4D lattice, a weight factor is associated with some of the directions. Dimensionless mass densities can be described by a real function $N_i(\mathbf{x}, t)$ and they are associated with velocities $\mathbf{c_i}$ where the subscript i indicates the velocity direction the mass density is traveling in, $\mathbf{x}$ is the position on the lattice and t is the time. The evolution equation of the mass densities is given by

$$N_i(\mathbf{x} + \mathbf{c_i}, t + 1) = N_i(\mathbf{x}, t) + \Omega_i(\mathbf{N}) \tag{2.1}$$

The mass density at position $\mathbf{x}$ moves to the position $\mathbf{x} + \mathbf{c_i}$ with each time step where collision can modify its mass density. Here $\Omega_i(\mathbf{N})$ is the collision operator which repre-

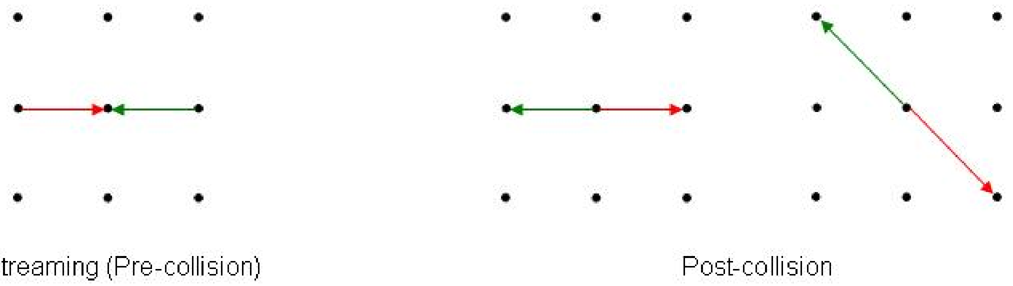

Figure 2.1: Demonstration of some possible streaming (pre-collision) and post-collision states.

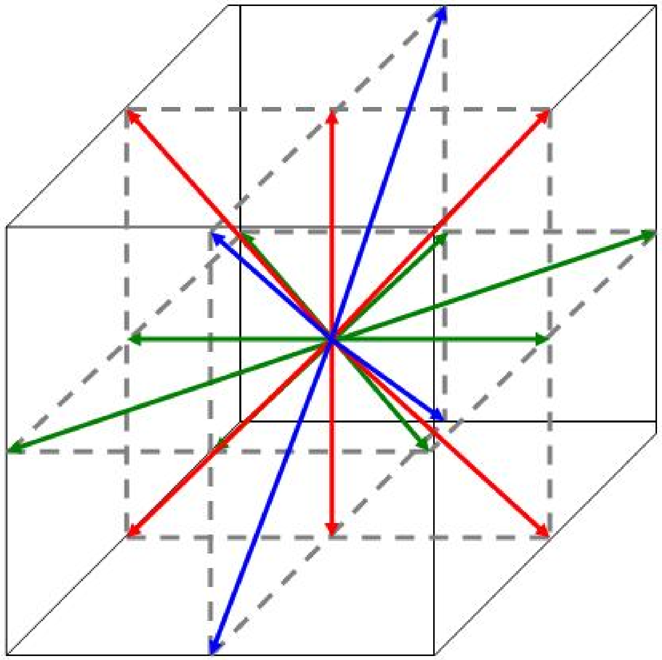

Figure 2.2: 3D projection of a 4D FCHC lattice

sents the rate of change of mass densities from collision. This collision operator depends upon the all components of mass densities and is required to satisfy conservation of mass and momentum at each lattice:

$$\sum_i \Omega_i(\mathbf{N}) = 0 \tag{2.2}$$

$$\sum_i \mathbf{c_i}\Omega_i(\mathbf{N}) = \mathbf{f} \tag{2.3}$$

where **f** is optional external force (e.g. gravity) that drives the flow.

Frisch et al. [5] has reported that Equation 2.1 is equivalent to Navier-Stokes equations when Ω assures convergence of lattice-Boltzmann scheme to the following equilibrium solution:

$$N_i = \frac{m_i\rho}{24}\,[\,1+2\mathbf{c_i}\cdot\mathbf{u}+3\{\mathbf{c_i}\mathbf{c_i}:\mathbf{u}\mathbf{u}-\tfrac{1}{2}(\mathbf{u}\mathbf{u})\}-6\nu\{(\mathbf{c_i}\cdot\nabla)(\mathbf{c_i}\cdot\mathbf{u})-\tfrac{1}{2}\nabla\cdot\mathbf{u}\}+\mathcal{O}(u^3,u\nabla u)\,] \tag{2.4}$$

where m_i is weight factor for $\mathbf{c_i}$, $\mathbf{u}$ is the velocity vector while ρ and ν are the density and kinematic viscosity, respectively. Before going further, it is worth mentioning here that in lattice-Boltzmann scheme, the units of distance and time are unit lattice space and unit time step, respectively. All the liquid properties and flow variables are scaled to dimensionless quantities with in certain ranges (e.g. $\rho \sim 8$, $0.25 > \nu > 10^{-5}$) [6]. All the parameters defined by LB units in this work are considered as dimensionless and scaled in this way. Now momentum and density can be calculated by notions

$$\rho = \rho(\mathbf{x}, t) = \sum_i N_i(\mathbf{x}, t) \tag{2.5}$$

$$\rho\mathbf{u} = \rho\mathbf{u}(\mathbf{x}, t) = \sum_i \mathbf{c_i} N_i(\mathbf{x}, t) \tag{2.6}$$

Substituting Equation 2.4 into,2.1 carrying out the summation over all i, finally using the constraint given by Equation 2.2 and symmetry properties of the FCHC lattice, we obtain the following equation for mass conservation:

$$\frac{\partial \rho}{\partial t} + \nabla \cdot \rho\mathbf{u} = 0 \tag{2.7}$$

To recover momentum balance equation, we substitute Equation 2.4 into Equation 2.1 multiplied by $\mathbf{c_i}$, summate over i and use the constraint given by Equation 2.3 and symmetry properties of the FCHC lattice. Carrying out all this leads to the following equation:

$$\frac{\partial}{\partial t}(\rho\mathbf{u}) + \nabla \cdot \rho\mathbf{u}\mathbf{u} = -\nabla P + \nabla \cdot \rho\nu(\nabla\mathbf{u} + (\nabla\mathbf{u})^T) - \nabla(\tfrac{1}{2}\rho\nu\nabla \cdot \mathbf{u}) + \mathbf{f} \tag{2.8}$$

The Equation 2.8 is Navier-Stokes equation only in incompressible limit. Since the velocity range considered in lattice-Boltzmann scheme is $|u| < 0.2$ [6] for incompressibility limit (the speed of sound in the lattice-Boltzmann scheme is of the order of one), the higher order terms represented by $\mathcal{O}(u^3, u\nabla u)$ in Equation 2.4 have been neglected.

Consideration of these terms would have caused some additional terms in Equations 2.7 and 2.8 giving obvious deviation from the Navier-Stokes equations.

2.1.3 Implementation of lattice-Boltzmann method

There are various possible implementations of LBM. In present work, we make use of the formulation by Eggels and Somers [6], which is described in this section.

Time evolution of mass densities is described in Equation 2.1, however a proper definition of $\Omega(\mathbf{N})$ is still required so that lattice-Boltzmann scheme converges to an equilibrium solution. To achieve this, Eggels and Somers redefine Equation 2.1 as (staggered formulation of the LB equation):

$$N_i(\mathbf{x}+\tfrac{1}{2}\mathbf{c_i}, t+\tfrac{1}{2}) = N_i(\mathbf{x}-\tfrac{1}{2}\mathbf{c_i}, t-\tfrac{1}{2}) + \Omega_i(\mathbf{N}) \tag{2.9}$$

By doing a first order Taylor expansion around $\mathbf{x}$ and t and neglecting higher order terms

$$N_i(\mathbf{x}\pm\tfrac{1}{2}\mathbf{c_i}, t\pm\tfrac{1}{2}) = N_i(\mathbf{x}, t) \pm \tfrac{1}{2}\mathbf{c_i}\cdot\nabla N_i(\mathbf{x}, t) \pm \tfrac{1}{2}\partial_t N_i(\mathbf{x}, t) \tag{2.10}$$

we find

$$\Omega_i(\mathbf{N}) = N_i(\mathbf{x}+\tfrac{1}{2}\mathbf{c_i}, t+\tfrac{1}{2}) - N_i(\mathbf{x}-\tfrac{1}{2}\mathbf{c_i}, t-\tfrac{1}{2}) \tag{2.11}$$

$$= \mathbf{c_i}\cdot\nabla N_i(\mathbf{x}, t) + \partial_t N_i(\mathbf{x}, t)$$

and now substituting $N_i(\mathbf{x}, t)$ from Equation 2.4, we get

$$\Omega_i(\mathbf{N}) = \frac{m_i\rho}{12}((\mathbf{c_i}\cdot\nabla)(\mathbf{c_i}\cdot\mathbf{u}) - \tfrac{1}{2}\nabla\cdot\mathbf{u}) + \frac{m_i}{12}\mathbf{c_i}\cdot\mathbf{f} \tag{2.12}$$

Combining the Equations 2.10 and 2.11, we obtain

$$N_i(\mathbf{x}\pm\tfrac{1}{2}\mathbf{c_i}, t\pm\tfrac{1}{2}) = N_i(\mathbf{x}, t) \pm \tfrac{1}{2}\Omega_i(\mathbf{N}) \tag{2.13}$$

Substituting the value of $N_i(\mathbf{x}, t)$ and $\Omega_i(\mathbf{N})$ from Equations 2.4 and 2.12, respectively into the Equation 2.13 we obtain

$$\begin{aligned} N_i(\mathbf{x} \pm \tfrac{1}{2}\mathbf{c_i}, t \pm \tfrac{1}{2}) &= \frac{m_i}{24}\left[\rho(1 + 2\mathbf{c_i} \cdot \mathbf{u} + 3\mathbf{c_i}\mathbf{c_i} : \mathbf{uu} - \tfrac{1}{2}(\mathbf{uu}) - 6\nu(\mathbf{c_i} \cdot \nabla)(\mathbf{c_i}\cdot\mathbf{u})\right. \\ &\quad \left. -\tfrac{1}{2}\nabla.\mathbf{u}) \pm \rho((\mathbf{c_i} \cdot \nabla)(\mathbf{c_i}\cdot\mathbf{u}) - \tfrac{1}{2}\nabla \cdot \mathbf{u}) + \mathbf{c_i}\cdot\mathbf{f}\ \right] \end{aligned} \tag{2.14}$$

which can be rewritten in terms of a $n \times n$ matrix E_{ik} and a solution vector $\beta_k^{\pm}$ as

$$N_i(\mathbf{x} \pm \tfrac{1}{2}\mathbf{c_i}, t \pm \tfrac{1}{2}) = \frac{m_i}{24}\sum_{k=1}^{n} E_{ik}\beta_k^{\pm}(\mathbf{x}, t) \tag{2.15}$$

where n is the number of velocity directions. $\beta_k^{\pm}$, the solution vector contains liquid properties such as the density and velocity. For $D3Q18$ scheme ($n = 18$) which is used in this work , the matrix E_{ik} and solution vector $\beta_k^{\pm}$ are given by

$$E_{ik} = \begin{bmatrix} 1,\ 2c_{ix},\ 2c_{iy},\ 2c_{iz},\ 3(c_{ix}^2 - \frac{1}{2}),\ 6c_{ix}c_{iy},\ 3(c_{iy}^2 - \frac{1}{2}), \\ 6c_{ix}c_{iz},\ 6c_{iy}c_{iz},\ 3(c_{iz}^2 - \frac{1}{2}),\ c_{ix}(3c_{iy}^2 - 1),\ c_{iy}(3c_{ix}^2 - 1), \\ c_{ix}(2c_{iz}^2 + c_{iy}^2 - 1),\ c_{iy}(2c_{iz}^2 + c_{ix}^2 - 1),\ c_{iz}(3c_{ix}^2 + 3c_{iy}^2 - 2), \\ c_{iz}(c_{iy}^2 - c_{ix}^2),\ 3(c_{ix}^2 - c_{iy}^2)^2 - 2,\ (c_{ix}^2 - c_{iy}^2)(1 - 2c_{iz}^2) \end{bmatrix} \tag{2.16}$$

and

$$\beta_k^{\pm}(\mathbf{x}, t) = \begin{bmatrix} \rho,\ \rho u_x \pm \frac{1}{2}f_x,\ \rho u_y \pm \frac{1}{2}f_y,\ \rho u_z \pm \frac{1}{2}f_z, \\ \rho(u_x u_x) + \rho(\dfrac{\pm 1 - 6\nu}{6})(2\partial_x u_x), \\ \rho(u_x u_y) + \rho(\dfrac{\pm 1 - 6\nu}{6})(\partial_x u_y + \partial_y u_x), \\ \rho(u_y u_y) + \rho(\dfrac{\pm 1 - 6\nu}{6})(2\partial_y u_y), \\ \rho(u_x u_z) + \rho(\dfrac{\pm 1 - 6\nu}{6})(\partial_x u_z + \partial_z u_x), \\ \rho(u_z u_y) + \rho(\dfrac{\pm 1 - 6\nu}{6})(\partial_z u_y + \partial_y u_z), \\ \rho(u_z u_z) + \rho(\dfrac{\pm 1 - 6\nu}{6})(2\partial_z u_z), \\ T_1^{\pm}, T_2^{\pm}, T_3^{\pm}, T_4^{\pm}, T_5^{\pm}, T_6^{\pm}, F_1^{\pm}, F_2^{\pm} \end{bmatrix} \tag{2.17}$$

with $T_1^{\pm}, T_2^{\pm}, T_3^{\pm}, T_4^{\pm}, T_5^{\pm}, T_6^{\pm}$ are six third-order terms while $F_1^{\pm}, F_2^{\pm}$ are two fourth-order terms. See appendix A for the sequential time step procedure of Equation 2.15.

2.1.4 Boundary conditions in the LBM

Boundary conditions are the constraints specified to model interactions between liquid and objects as well as between the always finite lattice and its surrounding. In the following two types of commonly used boundary conditions are presented; bounce-back boundary condition and periodic boundary condition.

Every time the interaction between an object and liquid flow is of interest, no-slip boundary condition comes into the picture. Wolfram [7] and Lavallee et al. [8] used a particle distribution function bounce back scheme to mimic no-slip boundary conditions at plane walls. In this scheme, the particle distribution is reflected back to the node it comes from. Applying the bounce back scheme at a curved boundary is not that straightforward since the points of the curve may not coincide with lattice nodes. Therefore some sort of interpolation and extrapolation is required. The detailed explanation of this technique can be seen in appendix B.

Periodic boundary condition is important for dealing with the finiteness of the modeled system. This condition is implemented by connecting the edges of the simulated lattice with their opposites. This results in a system shaped like a hyper-torus. The implementation of this type of boundary condition is very easy, it is only necessary to copy particle distributions leaving the lattice at one side to the other side of the lattice cube resulting in an incoming particle distribution.

2.2 Non-Newtonian liquid models

Under the conditions of steady flow, if the shear stress (τ) needed to maintain the flow of the liquid is proportional to the shear rate ($\dot{\gamma}$) , the liquid is termed as Newtonian liquid. The proportionality constant is known as dynamic viscosity or simply viscosity (μ) of the liquid which is independent of shear rate. Many liquids do not appear to follow the linear

Newtonian stress-strain relationship under normal conditions ($\tau \neq \mu\dot{\gamma}$). Their viscosities vary with different parameters such as shear rate and time. These types of liquids are termed as non-Newtonian liquids. Non-Newtonian liquids can be broadly classified into two categories:1) Viscoelastic liquids 2) Purely viscous liquids. Viscoelastic liquids whose flow properties are the combination of elastic and viscous behavior, are not considered in present work. A liquid model is a mathematical expression which represents the essential flow properties of liquid. A brief insight into the general theoretical models of some purely viscous non-Newtonian liquids is provided through Table 2.1. The time-independent models mentioned in Table 2.1 are graphically depicted on shear rate-shear stress axes in Figure 2.3.

It is obvious from this discussion that mimicking non-Newtonian liquids poses a tougher challenge due to the variable_apparent viscosity. In this work, solid particle motion behavior is studied in Bingham liquid and thixotropic liquid. Some of the theoretical models given in Table 2.1 are modified to accommodate them feasibly with computer algorithm.

2.2.1 Bingham model

Bingham liquids, a special subclass of viscoplastic liquids ($n = 1$, refer Table 2.1),_possess a yield stress (τ_0) which must be exceeded before the fluid shows any significant deformation. Bingham model is one of the simplest mathematical models which is used to describe the flow properties of liquid with yield stress. Qualitatively Bingham model can be characterized by a flow curve which has an intercept τ_0 at shear stress axis and slope μ_p (Figure 2.4). The shear rate remains zero and the material behaves like a solid until shear stress exceeds yield limit of the liquid. Once the liquid is yielded, it flows with a net shear stress of $\tau - \tau_0$. In a generalized manner, constitutive equations for Bingham model can be written as

$$\tau_{ij} = 2(\frac{\tau_0}{\dot{\gamma}} + \mu_p)d_{ij} \quad |\tau| > \tau_0 \tag{2.18}$$

Purely viscous (non-elastic) non-Newtonian liquids	
Time-independent	Time-dependent
Viscoplastic liquid $\mu_a(\dot{\gamma}) = \frac{\tau_0}{\dot{\gamma}} + K(\dot{\gamma})^{n-1} \quad, n > 0$	Thixotropic liquid $\mu_a = f(\dot{\gamma}, t)$
Shear-thinning liquid $\mu_a(\dot{\gamma}) = m(\dot{\gamma})^{n-1} \quad, 0 < n < 1$	
Shear-thickening liquid $\mu_a(\dot{\gamma}) = m(\dot{\gamma})^{n-1} \quad, n > 1$	

μ_a: apparent viscosity

Table 2.1: Rheological models of purely viscous non-Newtonian liquids.

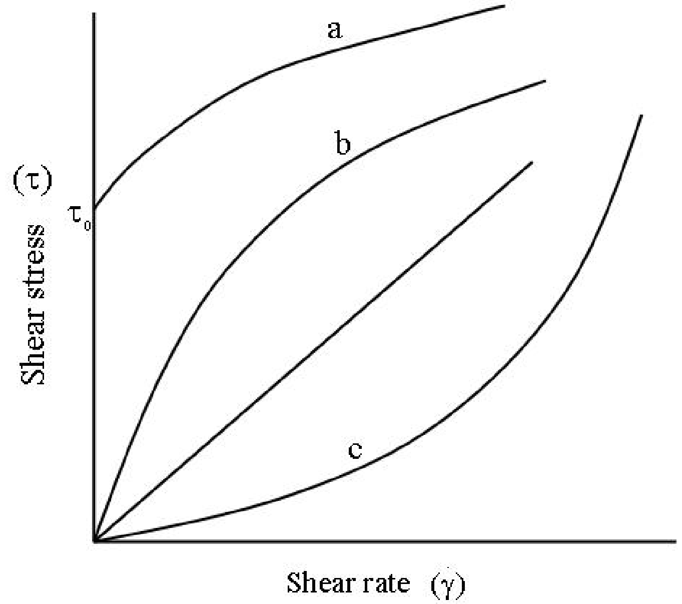

Figure 2.3: Graphical demonstration of time-independent theoretical models in Table 2.1 with a: viscoplastic liquid, b:shear-thinning liquid, c: shear-thickening liquid. The straight line represents a Newtonian liquid.

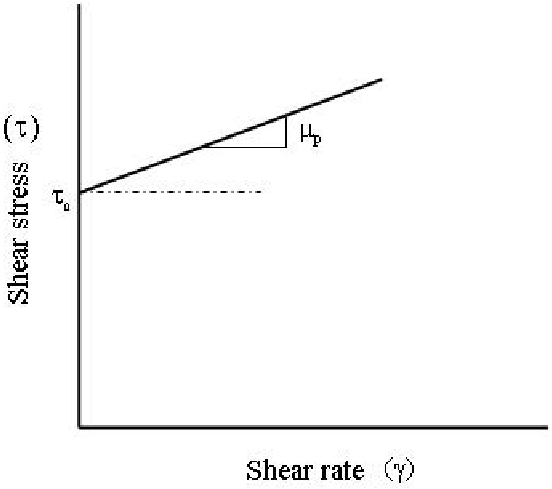

Figure 2.4: One dimensional representation of Bingham model

$$d_{ij} = 0 \quad |\tau| < \tau_0 \tag{2.19}$$

In the above expressions, τ_{ij} is deviatoric part of whole stress tensor σ_{ij}, $\dot{\gamma}$ is the deformation rate ($\sqrt{d_{ij}d_{ij}}$), d_{ij} is the rate of deformation tensor $[1/2((\partial u_i/\partial x_j)+(\partial u_j/\partial x_i))]$, μ_p is the plastic viscosity and $|\tau|$ is magnitude of shear stress ($\sqrt{\tau_{ij}\tau_{ij}}$).

One of the difficulties encountered in implementing the Bingham model with computer code is its non-differentiable form. Moreover, in perspective of computational fluid dynamics it is an unusual situation to compute the shear stress to determine the yielding where one typically solves the velocity component first and then shear rate. Approaching this problem another way, one can think of estimating the state of no-deformation by computing the zero shear rate. However this approach is ruled out due to the numerical noise which always produces some shear rate whatsoever small it may be. Therefore it becomes highly difficult to locate the state of absolute rigidity. There are mainly three approaches; dual viscosity model [9, 10], regularization methods [11, 12] and variational inequality based methods [13, 14] which have been used in literature to counter these problems. First two methods approximate the Bingham model by considering the solid region as a highly viscous material. Therefore the flow curve transits from solid (high viscosity) state to yielded liquid (low viscosity) state without having discontinuity.

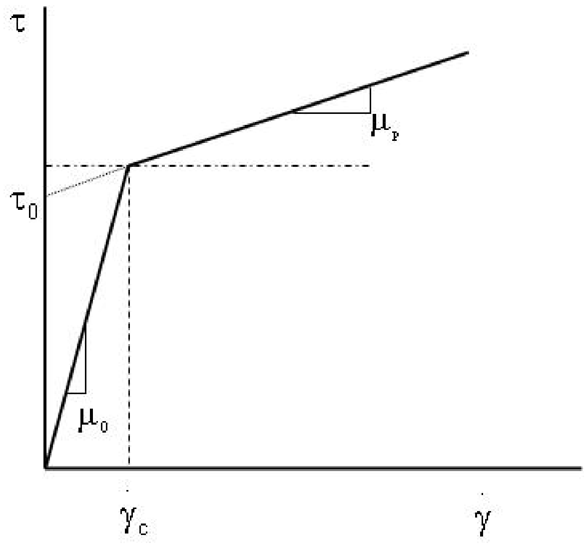

Figure 2.5: One dimensional representation of dual viscosity Bingham model

The variational inequality method, rigorously equivalent to original Bingham model, is implemented by introducing Lagrange multiplier.

In this study, dual viscosity model is used to mimic Bingham liquids because of its less complex structure and easy implementation with lattice-Boltzmann scheme. In this model the region around zero shear rate is characterized by a highly viscous material with viscosity μ_0. Actual Bingham rheology is represented by a low viscosity μ_p. One dimensional dual viscosity Bingham rheology is shown in Figure 2.5. The transition (from high to low viscosity) point gives the critical shear rate ($\dot{\gamma_c}$) at shear rate axis. Mathematically, critical shear rate can be expressed by the notion

$$\dot{\gamma}_c = \frac{\tau_0}{\mu_0 - \mu_p} \tag{2.20}$$

When shear rate ($\dot{\gamma}$) becomes greater than critical shear rate, material is considered to be yielded. Thus the criterion of yielded and unyielded regions is defined as

$$\dot{\gamma} > \dot{\gamma}_c \rightarrow yielded \tag{2.21}$$

$$\dot{\gamma} \leq \dot{\gamma}_c \rightarrow unyielded \tag{2.22}$$

In this modified Bingham model, apparent viscosity (μ_a) and shear stress (τ_{ij}) of the material can be read as

$$\mu_a = \mu_0 \quad \dot{\gamma} \leq \dot{\gamma}_c \tag{2.23}$$

$$\mu_a = \mu_p + \frac{\tau_0}{\dot{\gamma}} \quad \dot{\gamma} > \dot{\gamma}_c \tag{2.24}$$

$$\tau_{ij} = 2\mu_a d_{ij} \tag{2.25}$$

2.2.2 Thixotropy model

Prior to discuss the modeling approach for thixotropy, a brief introduction to thixotropy is required. The flow behavior of many liquids can not be explained with a simple stress-strain curve. Apparent viscosities of these liquids not only depend on the shear rate, but also on the time for which liquid has been subjected to shearing. If a thixotropic liquid is subjected to a constant shear rate, its apparent viscosity decreases with time and it increases in absence of shear. Change in apparent viscosity with time at a constant shear rate can be linked with structural changes with in the liquid. Constant shear breaks down the liquid network. Conversely, as the structure breaks down, Brownian motion of the broken units tend to re-form the network. Both, the structure breakdown and structure build-up processes keep going together , so that eventually a state of dynamic equilibrium is reached when the network breaking and building rates are equal.

The modeling aspects of thixotropy have been reviewed earlier by Mewis [15], Barnes [16] and more recently by Mujumdar et al. [17]. Over the period of decades, researchers have used basically three approaches: phenomenological, direct micro structural and indirect micro structural. In the phenomenological models, researchers simulated the thixotropic liquid by modifying macroscopic parameters in constitutive equations of liquid models [18, 19, 20, 21]. The shortcoming of phenomenological models is the absence of direct connection with structure breakdown-build up processes which are responsible for thixotropic behavior. Direct micro structural approach overcomes this problem by introducing kinetic equation which defines the break up and build up of bonds. This approach was first formulated by Goodeve [22] and then used in several other studies [23, 24]. Moore [25] was the first to explain the thixotropic flow behavior by introducing a scalar structure parameter (indirect micro structural approach). As pointed out by both, Mewis [15]and Mujumdar et al. [17], the ultimate objective of both the direct or indirect approach is to couple the structural kinetics with the rheology of liquid.

In present work, the thixotropy model adopted is based on the early work by Storrey and Merrill [23], Moore [25], recently by Mujumdar et al. [17] and Ferroir et al. [26]. In this model, the structure (or network) of thixotropic liquid is defined by a scalar parameter λ whose value varies from 0 to 1. $\lambda = 0$ indicates complete network breakdown while $\lambda = 1$ signifies fully build up network. The transport equation of λ reads as:

$$\frac{\partial \lambda}{\partial t} + u_i \frac{\partial \lambda}{\partial x_i} = -k_1 \dot{\gamma} \lambda + k_2 (1 - \lambda) \tag{2.26}$$

where u_i is the ith component of the liquid velocity vector and $\dot{\gamma} = \sqrt{2 d_{ij} d_{ij}}$ is the shear rate. The first term on the right hand side of Equation 2.26 is responsible for break up of the network due to shear while the second term is responsible for build-up. The constants k_1 and k_2, an inverse of liquid time scale, are considered as breakdown and build-up parameters, respectively. To couple the structural kinetics with rheology, scalar parameter λ should be related to a macroscopic flow property. This is achieved by relating λ with apparent viscosity μ_a according to the purely viscous model used by Ferroir et al. [26] which reads

$$\mu_a = \mu_\infty (1 + \alpha \lambda) \tag{2.27}$$

The steady state ($\frac{\partial \lambda}{\partial t} = 0$) solution of Equation 2.26 with a homogeneous shear field ($\frac{\partial \lambda}{\partial x_i} = 0$) reads:

$$\lambda_{ss} = \frac{k_2}{k_1\dot{\gamma} + k_2} \tag{2.28}$$

If $\dot{\gamma} \rightarrow \infty$, $\lambda_{ss} = 0$ which means no network in presence of high shear. Conversely, $\lambda_{ss} = 1$ (fully developed network) when $\dot{\gamma} \rightarrow 0$ which is consistent with the definition of λ. The steady state viscosity can be derived by combining Equations 2.27 and 2.28.

$$\mu_{ss}(\dot{\gamma}) = \mu_{\infty}(1 + \alpha\frac{k_2}{k_1\dot{\gamma} + k_2}) \tag{2.29}$$

Again calculating the steady state viscosity at limiting values of shear rate, we find that

$$\mu_{ss}(\dot{\gamma}) = \begin{cases} \mu_{\infty} & \dot{\gamma} \rightarrow \infty \\ \mu_{\infty}(1+\alpha) & \dot{\gamma} \rightarrow 0 \end{cases} \tag{2.30}$$

Therefore μ_{∞} is the infinite shear viscosity and thixotropic parameter α can be derived from Equation 2.30 as:

$$\alpha = \frac{\mu_{ss}(0)}{\mu_{ss}(\infty)} - 1 \tag{2.31}$$

A typical representation of steady state thixotropic rheology is shown in Figure 2.6. It is interesting to observe that steady state thixotropic rheology shows some similarity with dual-viscosity Bingham model explained in subsection 2.2.1. Comparing the Equations 2.24_and 2.29, a_relation between yield stress of Bingham liquid and thixotropic parameters can be formed (assuming $k_1\dot{\gamma} >> k_2$) as:

$$\tau_0 = \mu_{\infty}\alpha\frac{k_2}{k_1} \tag{2.32}$$

Once the network build-up time scale ${}^{1}/_{k_2}$ is chosen, rest of the parameters of the thixotropic liquid can be fixed to simulate the liquid which, in steady state, exhibits Bingham behavior in the $\dot{\gamma} \rightarrow 0$ and $\dot{\gamma} \rightarrow \infty$ asymptotes. So the relations between thixotropic and Bingham parameters read

$$\mu_{\infty} = \mu_p \tag{2.33}$$

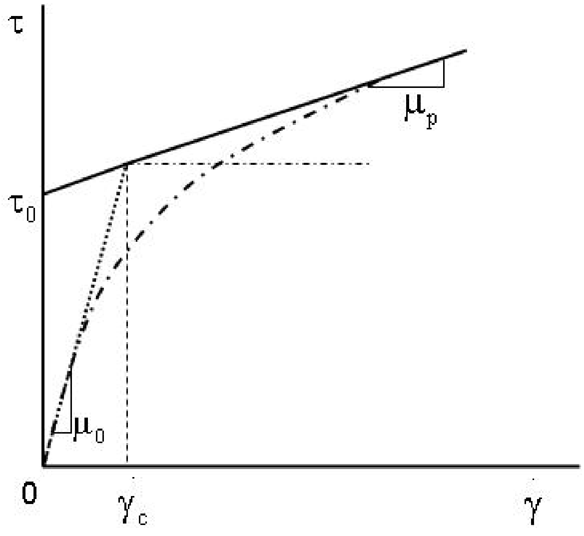

Figure 2.6: Steady-state rheology. Solid straight line: Bingham liquid with yield stress τ_0 and slope μ_p. Dashed line: very high viscosity (μ_0) in dual-viscosity model. Dash-dotted curve: steady-state behavior of thixotropic liquid.

$$\alpha = \frac{\mu_0}{\mu_p} - 1 \tag{2.34}$$

$$k_1 = \mu_p \alpha \frac{k_2}{\tau_0} \tag{2.35}$$

It is worthwhile to check the validity of the assumption ($k_1\dot{\gamma} >> k_2$) made for this analysis. Rewriting the assumption

$$k_1\dot{\gamma} >> k_2 \tag{2.36}$$

and substituting the value of k_1 from Equation 2.32 into the Equation 2.36, we obtain

$$\mu_\infty \alpha k_2 \frac{\dot{\gamma}}{\tau_0} >> k_2 \tag{2.37}$$

$$\dot{\gamma} >> \frac{\tau_0}{\mu_\infty \alpha} \approx \frac{\tau_0}{\mu_{ss}(0)} \tag{2.38}$$

Equation 2.38 shows that assumption made is valid in the region where shear rate is higher than $\tau_0/\mu_{ss}(0)$. In case of high viscosity ratio ($\frac{\mu_0}{\mu_p}$) in dual viscosity implementation, which is usually the case, Equations 2.38 and 2.20 can be compared with each other which confirms the similarity shown by two models in Figure 2.6.

$$\dot{\gamma}_c = \frac{\tau_0}{\mu_0 - \mu_p} \approx \frac{\tau_0}{\mu_{ss}(0)} \tag{2.39}$$

2.3 Contribution of present work

Lattice-Boltzmann scheme described in section 2.1 has been coded with Fortran programming language and the computer code used in this work is inherited from existing code. In addition, computer codes (based on LB scheme) exist for 1) two spheres motion in a shear flow (Newtonian liquid) 2) Bingham liquid flow in a channel and in a lid driven cavity and 3) thixotropic liquid flow in a lid driven cavity. In present work, the major contribution (in terms of programming) is to couple the single phase non-Newtonian rheology code with single sphere and two spheres code.

Bibliography

[1] S. Chen, G. D. Doolen, Lattice Boltzmann method for fluid flows, *Annu. Rev. Fluid Mech.* 30 (1998) 329.

[2] J. Hardy, O de Pazzis, Y. Pomeau, Molecular dynamics of a classical lattice gas: transport properties and time correlation functions, *Phys. Rev. A*.13 (1976) 1949.

[3] U. Frisch, B. Hasslacher, Y. Pomeau, Lattice-gas automata for the Navier-Stokes equations, *Phys. Rev. Lett.* 56 (1986) 1505.

[4] G. R. McNamara, G. Zanetti, Use of the Boltzmann equation to simulate lattice-gas automata, *Phys. Rev. Lett.* 61 (1988) 2332.

[5] U. Frisch, D. d'Humieres, B. Hasslacher, P. Lallemand, Y. Pomeau, J. P. Rivet, Lattice-gas hydrodynamics in two and three dimensions, *Complex Syst.* 1 (1987) 649.

[6] J. G. M. Eggels, J. A. Somers, Numerical simulation of free convective flow using the lattice-Boltzmann scheme, 1995, *Int. J. Heat fluid flow* 16 (1995) 357.

[7] S. Wolfram, Cellular automaton fluids, 1: Basic theory, *J. Stat. Physics*.45 (1986) 471.

[8] P. Lavallee, J. P. Boon, A. Noullez, Boundaries in lattice gas flows, *Physics D*.47 (1991) 233.

[9] E. J. O'Donovan, R. I. Tanner, Numerical study of the Bingham squeeze film problem, *J. Non-Newtonian Fluid Mech.*, 15 (1984) 75.

[10] C. R. Beverly, R. I. Tanner, Numerical analysis of extrudate swell in viscoelastic materials with yield stress, *J. Rheol.* 33 (1989) 989.

[11] E. Mitsoulis, Th. Zisis, Flow of Bingham plastics in a lid-driven square cavity, *J. Non-Newtonian Fluid Mech.* 101 (2001) 173.

[12] T. C. Papanastasiou, Flow of materials with yield, *J. Rheol.* 31 (1987) 385.

[13] D. Vola, L. Boscardin, J. C. Latche, Laminar unsteady flows of Bingham fluids: a numerical strategy and some benchmark results, *J. Comp. Phys.* 187 (2003) 441.

[14] Z. Yu, A. Wachs, A fictitious domain method for dynamic simulation of particle sedimentation in Bingham liquids, *J. Non-Newtonian Fluid Mech.* 145 (2007) 78.

[15] J. Mewis, Thixotropy-a general review,*J. Non-Newtonian Fluid Mech.* 6 (1979) 1.

[16] H. A. Barnes, Thixotropy-a review, *J. Non-Newtonian Fluid Mech.* 70 (1997) 1.

[17] A. Mujumdar, A. N. Beris, A. B. Metzner, Transient phenomena in thixotropic systems, *J. Non-Newtonian Fluid Mech.* 102 (2002) 157.

[18] A. Silbar, P. R. Paslay, Retarded flow of Bingham materials, *J. Appl. Mech.* 26 (1959) 107.

[19] J. Elliot. A. J. Ganz, Modification of food characteristics with cellulose hydrocolloids. I. Rheological characterization of an organoleptic property, *J. Texture Stud.* 2 (1971) 220.

[20] J. Elliot. A. J. Ganz, Salad dressings-preliminary rheological characterization, *J. Texture Stud.* 8 (1977) 359.

[21] Y. Suetsugu, J. White, A theory of thixotropic plastic viscoelastic fluids with a time-dependent yield surface and its comparison to transient and steady state experiments on small particle filled polymer melts, *J. Non-Newtonian Fluid Mech.* 14 (1984) 121.

[22] C. F. Goodeve, A general theory of thixotropy and viscosity, *Trans. Faraday Soc.* 35 (1939) 342.

[23] B. T. Storrey, E. W. Merrill, The rheology of aqueous solution of amylose and amylopectine with reference to molecular configuration and intermolecular association, *J. Polym. Sci.* 33 (1958) 361.

[24] M. M. Cross, Rheology of non-Newtonian fluids: a new flow equation for pseudoplastic systems, *J. Colloid Inter. Sci.* 20 (1965) 417.

[25] F. Moore, The rheology of ceramic slips and bodies, *Trans. Br. Ceramic Soc.* 58 (1959) 470.

[26] T. Ferroir, H. T. Huynh, X. Chateau, P. Coussot, Motion of a solid object through a pasty (thixotropic) fluid, *Phys. Fluids* 16 (2004) 594.

Chapter 3

Benchmark cases for non-Newtonian liquids

Prior to present and analyze the results of solid-liquid suspension (the main focus of this work), it is necessary and desirable to validate the numerical solution procedure discussed in the preceding chapter. Validation of this procedure is accomplished by benchmarking the numerical results against the available reliable numerical, experimental and/or analytical predictions for the analogous problem. We illustrate this by appealing to two important benchmark problems in non-Newtonian fluid mechanics, namely channel flow and lid driven cavity flow.

3.1 Channel flow

The steady laminar channel flow between two fixed parallel plates is also known as plane Poiseuille flow. It is a standard benchmark used by researchers over several years to validate a procedure.

3.1.1 Description of the problem

A 2-D projection of the geometry for this benchmark test is seen in Figure 3.1 (a). An external body force f_0 drives the flow between two plates at a mutual distance of H. Body force produces a shear stress with linear profile

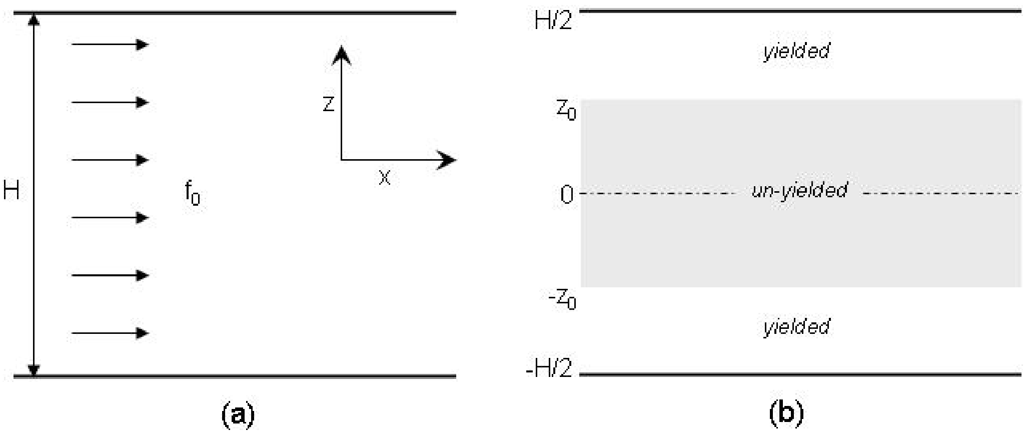

Figure 3.1: (a) 2D projection of the geometry of the channel flow (b) sketch showing yielded/unyielded boundaries at steady state.

$$\tau_{zx} = -f_0 z \tag{3.1}$$

We define yield stress and plastic viscosity of Bingham liquid as τ_0 and μ_p, respectively. Since the external force is one dimensional, the flow velocity lies in the x direction and is a function of z alone. This velocity U_x can be derived from the notion

$$\frac{\partial U_x}{\partial z} = -\frac{f_0 z}{\mu_p} \tag{3.2}$$

No-slip boundary conditions are imposed on fixed walls, while periodic boundary conditions are applied for inlet and outlet of the channel.

3.1.2 Analytical solution

Before presenting the simulation results, we analytically derive the velocity expression for the problem depicted in subsection 3.1.1. In the system defined by Figure 3.1 (b), the shear stress has maximum value close to the walls ($z = H/2$ and $-H/2$) while it decreases towards the center ($z = 0$). Let us define a distance $|z_0|$ for which $|\tau_{zx}| = \tau_0$ (i.e. $\tau_0 = f_0|z_0|$). Therefore we get three regions which are mathematically defined as

$$z_0 < z < H/2 \rightarrow \frac{\partial U_x}{\partial z} \neq 0 \rightarrow yielded\, region$$

$$-z_0 < z < z_0 \rightarrow \frac{\partial U_x}{\partial z} = 0 \rightarrow unyielded\, region$$

$$-H/2 < z < -z_0 \rightarrow \frac{\partial U_x}{\partial z} \neq 0 \rightarrow yielded\, region$$

First we derive the velocity expression for region $-H/2 < z < -z_0$ by integrating the Equation 3.2

$$U_x = -\frac{1}{2}\frac{f_0}{\mu_p}z^2 - \frac{\tau_0}{\mu_p}z + c \tag{3.3}$$

where c is an integration constant. Applying the no-slip boundary condition $U_x = 0$ at $z = -H/2$ with Equation 3.3 we obtain the integration constant c as

$$c = \frac{1}{8}\frac{f_0}{\mu_p}H^2 - \frac{\tau_0 H}{2\mu_p} \tag{3.4}$$

Replacing the value of constant c from Equation 3.4 to Equation 3.3, we obtain

$$U_x = \frac{f_0}{2\mu_p}(\frac{H^2}{4} - z^2) - \frac{\tau_0}{\mu_p}(\frac{H}{2} + z) \tag{3.5}$$

The Equation 3.5 is valid for region $-H/2 < z < -z_0$. The velocity of unyielded region at $z = -z_0$ is obtained by replacing z with $-\tau_0/f_0$ in Equation 3.5 which results in expression

$$U_x|_{-z_0} = \frac{1}{\mu_p}(\frac{f_0 H^2}{8} + \frac{\tau_0^2}{2f_0} - \frac{\tau_0 H}{2}) \tag{3.6}$$

The unyielded liquid in the region $-z_0 < z < z_0$ moves with a constant velocity given by Equation 3.6. Since the flow is symmetric about center line, velocity expression for region $z_0 < z < H/2$ can be derived using similar procedure.

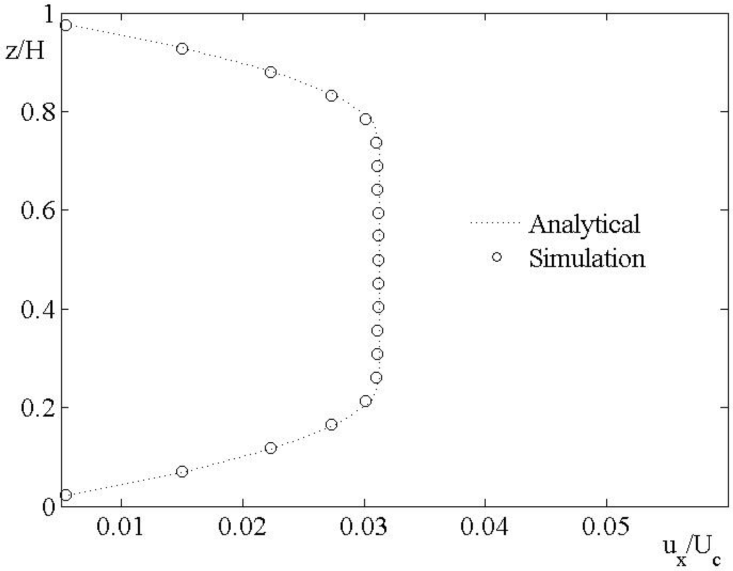

Figure 3.2: Steady state velocity profile of a Bingham liquid in a channel flow.

3.1.3 Simulation

For this problem we used a lattice grid of size 41 × 1 × 21 (x, y, z) filled with Bingham liquid of density $\rho = 8.0$ and plastic kinematic viscosities being $\nu_0 = 0.5$, $\nu_p = 0.004$, all in lattice-Boltzmann (LB) units. One can refer subsection 2.1.2 to get the idea of LB units. The simulation is performed with $f_0 = 0.0001$ and a comparison of the steady state velocity in x direction with the analytical solution can be seen in Figure 3.2. The velocity is made dimensionless using a characteristic velocity U_c which is steady state velocity of Newtonian liquid in channel flow with same conditions and physical properties (Newtonian liquid $\nu = \nu_p$). The velocity profile of channel flows features a velocity gradient (see Equation 3.2) which decreases towards the center of the channel. Hence the shear stress transmitted by a liquid layer also decreases towards the channel center. For the reason that Bingham liquids become solid when the applied shear stress falls below the yield stress it is obvious that the Bingham liquid will become solid in the center layers of the channel. There a solid plug moves within the flow, illustrated by the flat profile of Figure 3.2. Looking at Figure 3.2 we observe an excellent agreement of simulation result with analytical solution.

3.2 Lid driven cavity flow (Bingham liquid)

3.2.1 Introduction

In computational fluid dynamics field lid driven cavity flow is a widely used test case for benchmarking incompressible iso-thermal liquid flows. This is a model for flow in a cavity where the upper boundary moves tangentially, and thus causes a rotation in the cavity. Due to the simplicity of cavity geometry, applying a numerical method on this flow problem is fairly easy and straight forward. Despite its simple geometry, the driven cavity flow retains a rich fluid flow physics manifested by recirculating region(s). For Newtonian liquids, this problem has been extensively studied by researhcers [1, 2, 3] over several decades. However research activities on lid driven cavity flows with non-Newtonian liquids caught the pace with the improvements in computational algorithms and power. These include studies on viscoelastic liquid [4, 5, 6], power law liquid [8] and Bingham liquid [9, 10, 11, 12].

Considering moderate inertial influence ($Re = 1$), Bercovier and Engleman [9] provided a finite element analysis of lid driven cavity flow with Bingham liquid using a mesh of square (10×10) elements. They illustrated the effect of different liquid yield stresses on the yielded/unyielded zone inside the cavity. Using finite element method (40×40 grid size) coupled with regularized constitutive law, Mitsoulis and Zisis [10] qualitatively confirmed the results obtained by Bercovier and Engleman [9] at creeping flow conditions. Also they observed that center of the primary vortex travels towards moving lid with increasing yield stress of liquid. Vola et al. [11] used the combination of characteristic/Galerkin method with Fortin-Glowinsky decomposition/coordination method (80×80 mesh size) to solve the lid driven cavity flow with Bingham liquid at low as well as high Re. Yu and Wachs [12] examined the problem at low Re using fictitious domain method (256×256 mesh size). In present work, lid driven cavity flow with purely viscous Bingham liquid is solved through dual-viscosity method using lattice-Boltzmann as numerical tool.

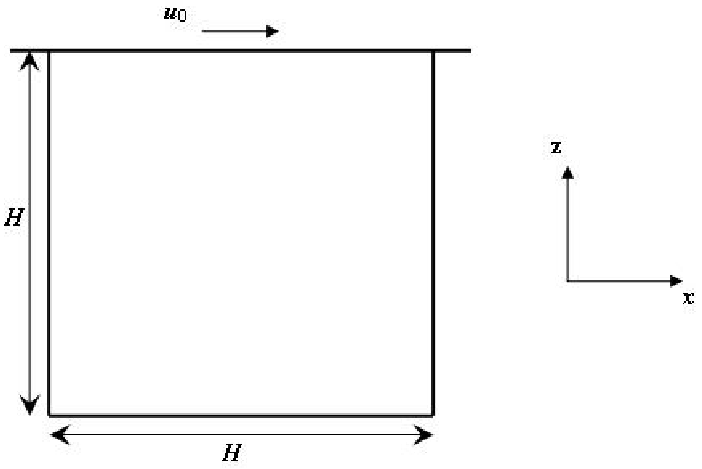

Figure 3.3: Lid driven cavity flow geometry and coordinate system

3.2.2 Flow definition and dimensionless numbers

Flow definition and coordinate system for lid driven cavity flow is defined in Figure 3.3. A Bingham liquid, contained inside a square cavity is set into motion by the upper wall which slides at constant speed. The velocity of the upper wall u_0 and the cavity depth H are taken as characteristic velocity and length, respectively. Originally a three-dimensional grid is used for simulating the flow, applying no-slip boundary conditions (using bounce-back scheme) at east-west, north-south. Periodic boundary conditions are imposed at front and back walls effectively making it a two-dimensional problem. Based on characteristic velocity and length, we introduce two non-dimensional numbers namely Reynolds number (Re) and Bingham number (Bn) which are defined by notions:

$$Re = \frac{\rho u_0 H}{\mu_p} \tag{3.7}$$

$$Bn = \frac{\tau_0 H}{\mu_p u_0} \tag{3.8}$$

3.2.3 Verification of numerical method

To establish the qualitative credibility of results obtained by a numerical method, it is desirable to verify the method with different numerical parameters. This is achieved by varying a certain numerical parameter and keeping all other unchanged. In this study, two parameters are investigated for the purpose of verification. One is the grid size of flow domain and other being the ratio of zero shear viscosity to plastic viscosity (μ_r). Previous researches have shown [10, 11, 12] that the location of primary vortex formed in lid driven cavity flow is appreciably influenced by the yield stress of Bingham liquid at low inertial effects (it moves closer to the moving lid as Bn increases). This appreciable change in location makes it an easily observable quantity. Therefore we monitor the vertical position (z coordinate) of primary vortex center to observe the qualitative credibility of our results. The center of primary vortex is the point having the minimum value of stream function (ψ) which is calculated through integration of velocity field ($u_x = \dfrac{\partial \psi}{\partial z}$, $u_z = -\dfrac{\partial \psi}{\partial x}$)

In a number of previous finite element studies of dual-viscosity Bingham model, researchers [13, 14] have found their results insensitive to very large values of viscosity ratio ($\mu_r > 1000$). Beverly and Tanner [15] reported the highest accuracy for an axis-symmetric problem when $\mu_r = 1000$. For present work, different values of viscosity ratio ($\mu_r = 250, 1250, 5000, 10000, 15000$) are chosen to measure the sensitivity of vertical position of primary vortex center. For each value of μ_r, simulations are performed over a range of liquid's yield stress ($Bn = 2, 5, 10, 20, 50, 100, 200, 500$) and the position of primary vortex (z coordinate) is monitored. Sensitivity of primary vortex position with yield stress (i.e. Bn) of liquid for each viscosity ratio is shown in Figure 3.4.

For the range of investigation ($2 \leq Bn \leq 500$), primary vortex moves closer to the moving lid on increasing the Bn only when $\mu_r > 1250$. However simulations with lower μ_r (≤ 1250) fail to deliver the expected results. This discrepancy can be attributed to the misleading velocity fields which can be generated from dual-viscosity model, if shear stresses or shear rates developed are very low compared to yield stress (τ_0) or critical shear rate ($\dot{\gamma}_c$), respectively. By decreasing the viscosity ratio, we increase the magnitude of critical shear rate. When yield stress of liquid is high ($Bn > 50$), developed shear rates are very low and may fall below the critical shear rate for lower viscosity ratios which in turn lead to the failure of dual-viscosity model. Figure 3.4 shows that

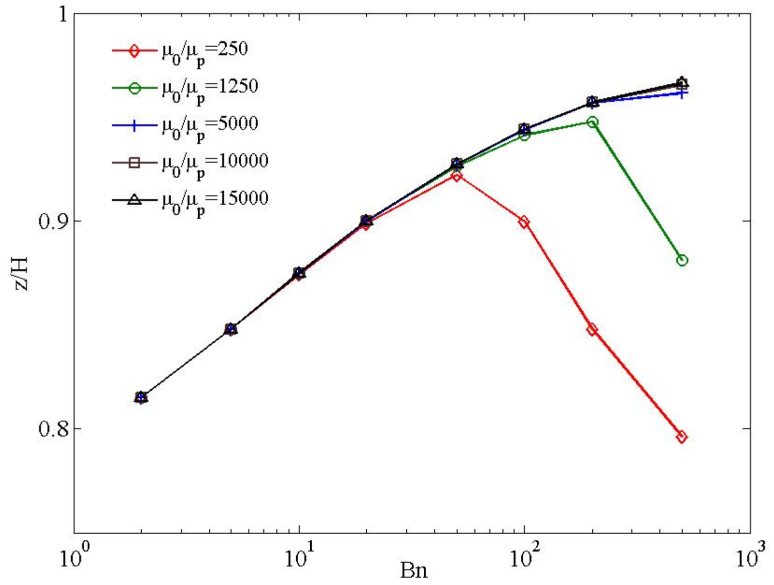

Figure 3.4: Sensitivity of z-coordinate of the primary vortex center with viscosity ratio (μ_r); grid size: $81 \times 2 \times 81$

after reaching a certain value, increase in viscosity ratio does not alter the position of primary vortex. We obtain approximately same results with $\mu_r = 10000, 15000$ (refer Table 3.1). Therefore we choose the value of viscosity ratio as 10000 which will be used in all Bingham liquid simulations of this chapter.

Bn	10	20	50	100	200	500
z/H ($\mu_r = 10000$)	0.8746	0.9000	0.9271	0.9441	0.9570	0.9655
z/H ($\mu_r = 15000$)	0.8747	0.9000	0.9272	0.9442	0.9570	0.9664
% difference	0.01	0	0.01	0.0001	0	0.09

Table 3.1: Sensitivity of z-coordinate of primary vortex with $\mu_r = 10000, 15000$

Choosing a appropriate grid to mimic the lid driven cavity problem is important in terms of accuracy and computational effort. Researchers have used different grid sizes for different methods to achieve satisfactory results (refer subsection 3.2.1). In this study, a comparison of results obtained through simulations based on various grid sizes is provided. Detailed quantitative comparison with literature is given in subsection 3.2.4. Keeping all other numerical parameters unchanged, simulations are performed with five different grids and the results are shown in Figure 3.5. Approximately same results

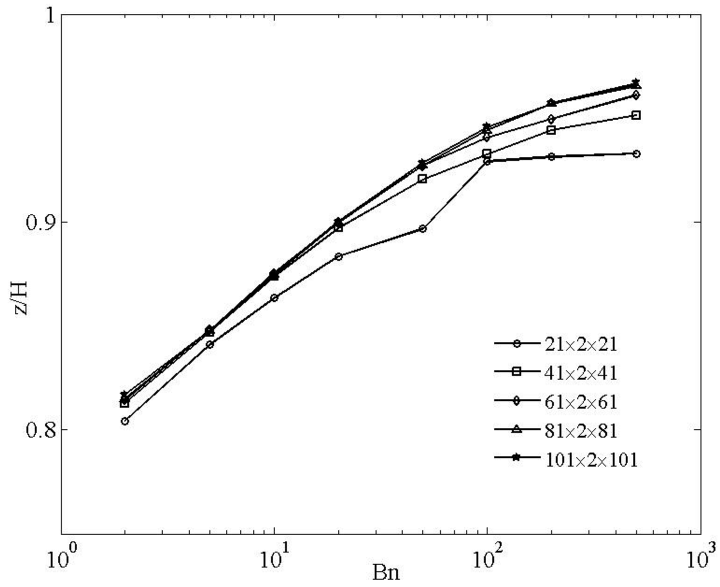

Figure 3.5: Sensitivity of z-coordinate of the primary vortex center with grid size ($x \times y \times z$);$\mu_r = 10^4$

are observed for all grids with low Bingham numbers ($Bn \leq 50$) except $21 \times 2 \times 21$ grid, however they start to differ with higher Bingham numbers. For whole range of investigation ($2 \leq Bn \leq 500$), the results obtained from grid size $81 \times 2 \times 81$ differ little from those obtained from grid size $101 \times 2 \times 101$ (see Table 3.2). Since a finer grid ($101 \times 2 \times 101$) does not offer any significant contribution, we adhere to the grid size of $81 \times 2 \times 81$.

Bn	10	20	50	100	200	500
z/H ($81 \times 2 \times 81$ grid)	0.8746	0.9000	0.9271	0.9441	0.9570	0.9655
z/H ($101 \times 2 \times 101$ grid)	0.8744	0.8999	0.9283	0.9456	0.9570	0.9667
% difference	0.02	0.01	0.13	0.16	0	0.12

Table 3.2: Sensitivity of z-coordinate of primary vortex center with grids $81 \times 2 \times 81$ and $101 \times 2 \times 101$

3.2.4 Validation of numerical method

Based on verification of numerical method, viscosity ratio and grid size are chosen 10^4 and $81 \times 2 \times 81$, respectively for mimicking the lid driven cavity flow with Bingham liquid. Simulations are performed with various values of Bingham number ($2 \leq Bn \leq 500$)

keeping Reynolds number constant ($Re = 0.5$). Streamlines coupled with yielded (white) and unyielded (shaded) regions (defined by Equations 2.21 and 2.22) inside cavity at $Bn = 2, 5, 20, 50, 200$ and 500 are displayed in Figure 3.6. The unyielded regions in the cavity can be divided in two categories: a) lower unyielded region (close to the bottom wall) b) upper unyielded region (close to moving lid). Since the lid (top wall) is the only source to generate shear stress, effect imparted to lower region is not sufficient to yield the liquid. The formation of upper unyielded region takes place due to the existence of primary vortex where deformation rate is very small. It is easily observed that both the unyielded regions grow with the increase of Bingham number. In this study ($2 \leq Bn \leq 500$) the liquid is always yielded between upper unyielded region and lower unyielded region and moving lid and upper unyielded region.

At this juncture, it is interesting to observe the streamlines inside a cavity which are shown in Figure 3.6. Ideally, unyielded regions are solid regions and they should be quiescent . In present study we observe the streamlines passing through unyielded regions which indicates that these regions are not solid. In fact, the shear rate in these regions is so small that it makes them fall in the category of unyielded liquid defined by the criteria mentioned in Chapter 3.

Other quantities of interest are position of primary vortex and vortex intensity at its center. Vortex intensity is defined as $-\psi^*_{min}$ at the center of the vortex where ψ^* denotes dimensionless stream function. In the present work dimensionless stream function is evaluated from the notion:

$$\psi^* = \frac{\psi}{u_0 H} \tag{3.9}$$

Position of primary vortex can be determined as explained in subsection 3.2.3. A comparison of these quantities from this study with the literature can be seen in Figure 3.7. It is obvious that the position of primary vortex is a distinct function of the Bingham number. As yield stress (τ_0) of the liquid increases, it restricts the flow zone close to the moving lid, making regions away from the lid less active. This is confirmed by the Figure 3.6 too. The physical concept of stream function (ψ) is associated with the volumetric flow rate of liquid. With the increase of Bingham number, the liquid's resistance to lid

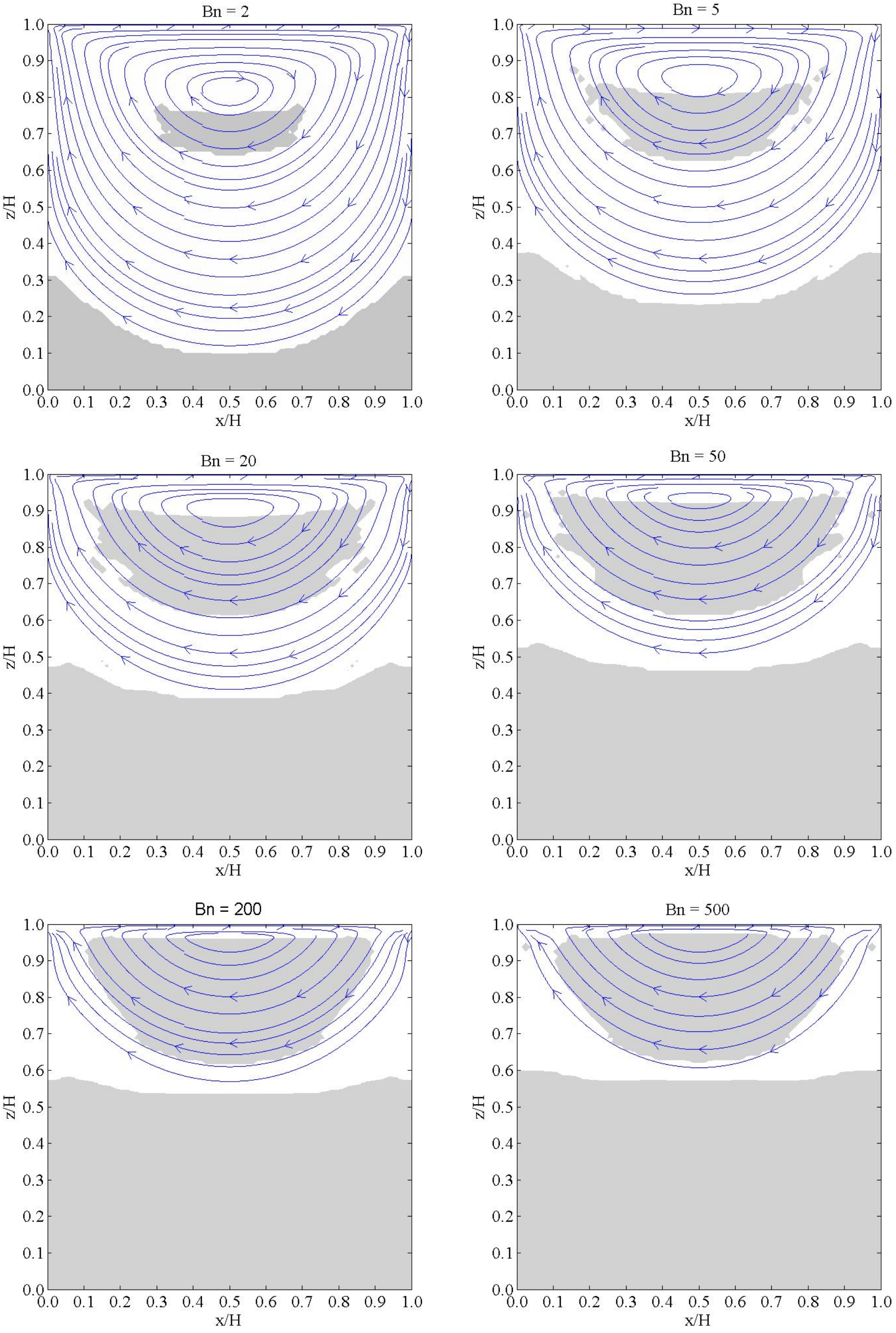

Figure 3.6: Yielded (white)/unyielded(shaded) regions together with streamlines for lid driven cavity flow of a Bingham liquid with different Bingham numbers at $Re = 0.5$

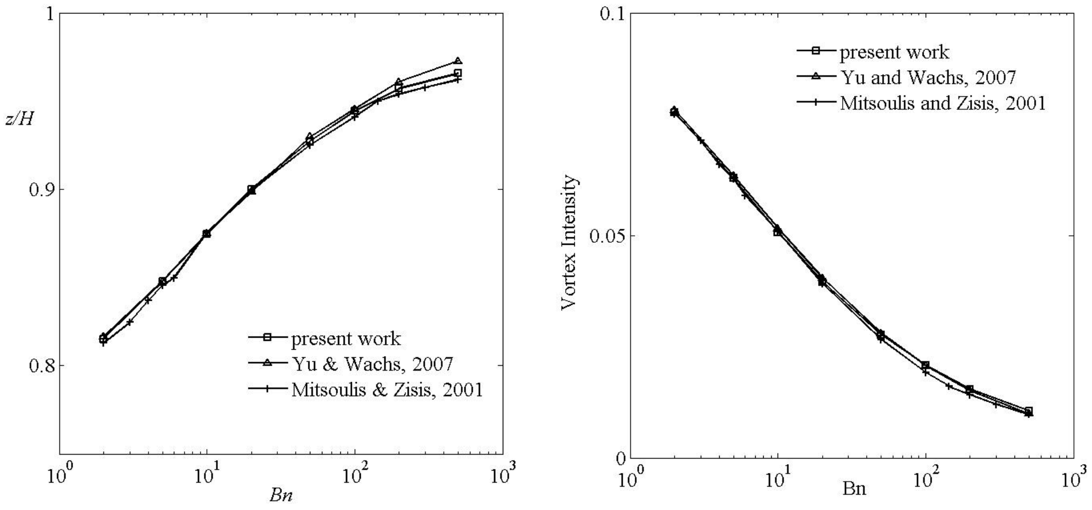

Figure 3.7: left: z-location of the vortex center as a function of Bn at Re=0.5, right: Vortex intensity at vortex center as a function of Bn at Re=0.5; comparison with literature results (Mitsoulis and Zisis [10]; Yu and Wachs [12])

motion increases which decreases the volumetric flow rate at vortex center.

3.2.5 High Reynolds number study

This work is started with the aim of achieving the steady state solution of lid-driven cavity flow at high Reynolds number. First we validate our numerical method with the results available in literature for Bingham liquid flows. The grid size is same as with low Reynolds number study i.e. $81 \times 2 \times 81$. We start the simulations with different Bingham numbers as done in previous subsection, at $Re = 1000$ and the comparison of results with literature are presented in Figure 3.8. Then in Figure 3.9 the plots of the streamlines and the rigid zones with various Bingham numbers are shown. It can be observed that vortex intensities obtained from our simulations agree well with those reported by Vola et al.[11]. While comparing the results of vertical position of primary vortex center, we see a deviation of around 3% and 1% with Vola et al. [11] at $Bn = 20$ and $Bn = 500$, respectively. Comparison of horizontal position data is also in close agreement with in the range of $2 \leq Bn \leq 100$. Near the range of $Bn = 20$, there seems to be a large deviation, however by looking the figure carefully, we can attribute this deviation to the less data points obtained by Vola et al. [11].

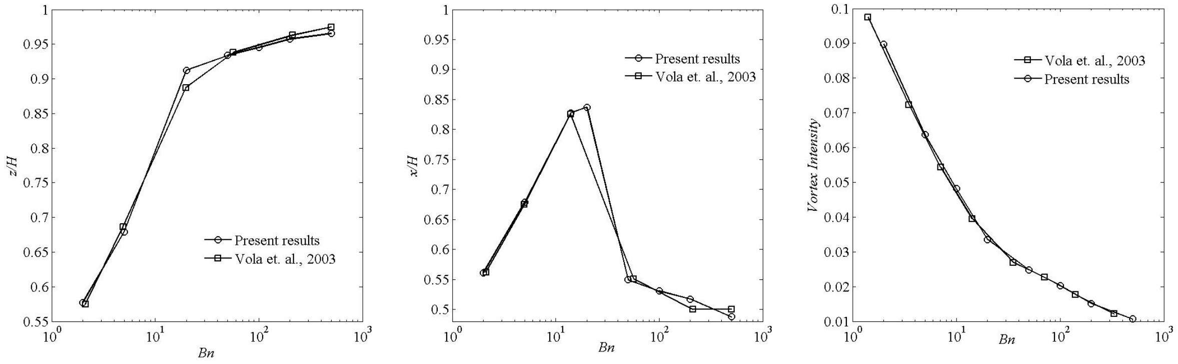

Figure 3.8: z-location (left) and x-location (center) of the vortex center as a function of Bn at $Re = 1000$; right: Vortex intensity at vortex center as a function of Bn at Re=1000; comparison with literature result (Vola et al. [11])

Figure 3.10 shows the positions (horizontal, vertical) of primary vortex center with different Bingham numbers, at $Re = 0.5, 10, 50$ and 1000. Vertical position of the vortex does not change significantly till $Re = 50$ (0.1% change from $Re = 0.5$ with $Bn = 2$). However an appreciable change in vertical position is observed with low Bingham numbers at $Re = 1000$. When inertial effects are highly dominating, Bingham liquid behaves like a Newtonian liquid. The value of vertical position of primary vortex center with $Bn = 2$ ($z/H = 0.5772$) obtained by this study is significantly close to the value of same quantity ($z/H = 0.5652$) observed by Botella and Peyret [16] with Newtonian liquid. As the yield stress of liquid increases, the inertial effects are softened and region away from the moving lid is less active, drawing vortex closer to the lid and we obtain similar results to that of low Reynolds number.

Horizontal position of primary vortex is significantly effected with low yield stress liquids as Reynolds number goes beyond 10. Till $Re \leq 50$, a definite trend is observed in the variation of horizontal position with Bingham number. At $Re = 1000$, again we observe a huge deviation from the trend. With in the range of $Bn \leq 20$ the vortex center travels into the direction of moving lid irrespective of the increase of yield stress. As yield stress further increases, inertial effects are softened and horizontal position follow the trend observed at low Re. It is interesting to note here that horizontal position of primary vortex center is more sensitive (as compared to vertical position) to Reynolds

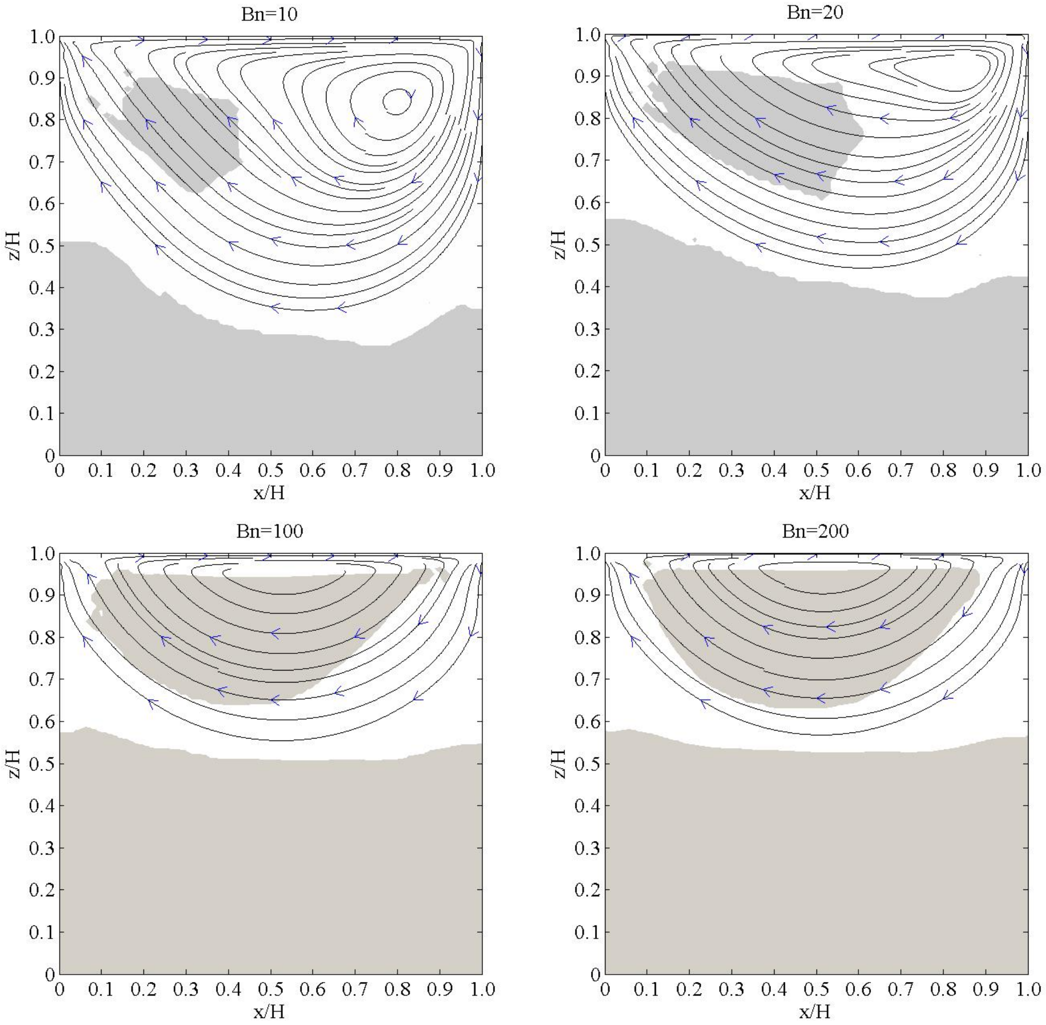

Figure 3.9: Yielded(white)/unyielded(shaded) regions together with streamlines for lid driven cavity flow of a Bingham liquid with different Bingham numbers at $Re = 1000$

number. Moreover, there seems to be a critical Bingham number (i.e. yield stress) related to liquid at a particular Reynolds number where it abruptly changes its flow behavior. In present study, this critical Bingham number is found to lie in the range of $20 \leq Bn \leq 50$ at $Re = 1000$.

3.3 Lid driven cavity flow (Thixotropic liquid)

Having tested the numerical procedure with Bingham liquid, it is applied to a more complex (rheological) medium i.e. thixotropic liquid. This work is build up on a recently

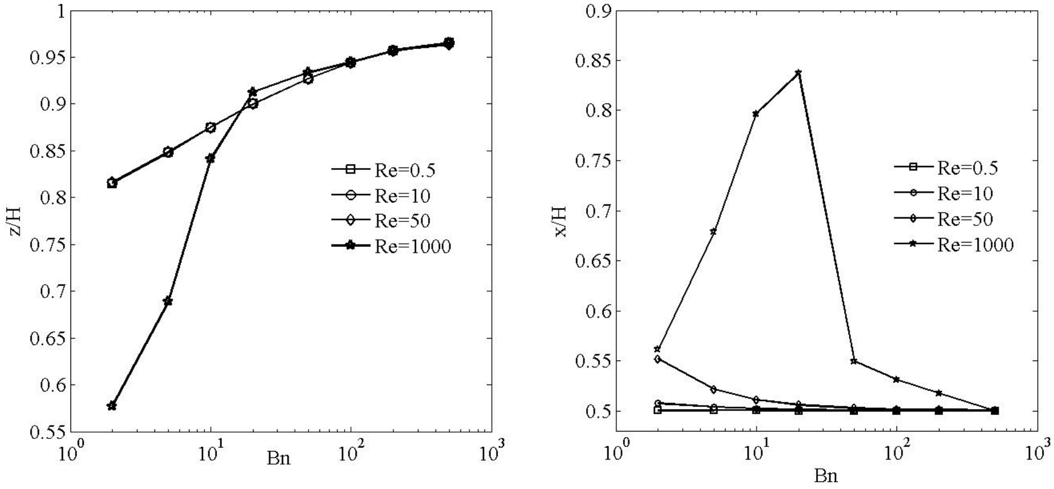

Figure 3.10: z-location (left) and x-location (right) of the vortex center as a function of Bn at $Re = 0.5, 10, 50$ and 1000.

published paper by Derksen and Prashant [17] which investigates the thixotropic effects on liquid's behavior by varying various thixotropic parameters.

3.3.1 Flow definition and dimensionless numbers

The flow definition of lid driven cavity flow with thixotropic liquid is same as with Bingham liquid (see Figure 3.3). Lid velocity u_0 and cavity depth H are taken as characteristic velocity and length, respectively. We define four dimensionless numbers (Reynolds number, Bingham number, Deborah number and viscosity ratio) which govern the flow in consideration. Reynolds number (Re) is based on characteristic quantities defined above.

$$Re = \frac{\rho u_0 H}{\mu_\infty} \tag{3.10}$$

The other dimensionless numbers involved in the LDC flow with thixotropic liquid are based on the liquid's asymptotic, steady state analogy with Bingham liquids. As mentioned in subsection 2.2.2, yield stress is related to thixotropic parameters according to $\tau_0 = \frac{\mu_\infty \alpha k_2}{k_1}$. Using this notion of yield stress the (pseudo) Bingham number (Bn) can be defined as

$$(pseudo)Bn = \frac{\alpha k_2 H}{k_1 u_0} \tag{3.11}$$

Deborah number (Db) is the ratio of liquid time scale ($^1/_{k_2}$) to flow time scale ($^H/_{u_0}$) while viscosity ratio ($\alpha + 1$) is the ratio between the zero-shear and infinite-shear viscosity.

$$Db = \frac{u_0}{H k_2} \tag{3.12}$$

$$\alpha = \frac{\mu_0}{\mu_\infty} - 1 \tag{3.13}$$

3.3.2 Verification of numerical method

In the recent study [17] it has been shown that vertical position of the primary vortex center is affected by dimensionless numbers such as Db, Bn and α. In present work, an attempt is made to describe the variation of vertical position of the primary vortex center with different Bingham numbers ($Bn = 2, 5, 10, 20, 50, 100, 200, 500$). The dimensionless numbers Re, Db and α are kept constant for all numerical experiments. We choose $Re = 0.5$, $Db = 1$ and $\alpha = \mu_r - 1$ where μ_r is the viscosity ratio chosen (after verification) with Bingham liquid simulations. Therefore the value of α turns out to be 9999.

The grid consists of $81 \times 2 \times 81$ ($x \times y \times z$) cells, no-slip boundary conditions at the four planar walls, and periodic conditions in the third (y) direction. The lid is set to move with velocity u_0 starting from a zero flow field. Results of these numerical experiments at steady state are shown in Figure 3.11. At steady state, the results of thixotropic rheology can be compared with Bingham rheology. In the case of the Bingham liquid, vertical position of primary vortex center increases with increase of Bingham number. The results shown in Figure 3.11 behave in the same manner until $Bn \leq 200$. The vortex center moves away from the lid at $Bn = 500$. This type of deviation has been observed while verifying the numerical technique with Bingham liquid (see Figure 3.4). As done in the subsection 3.2.3, the value of μ_r (i.e. α) is increased ($\alpha = 24999$). The difference in the result (vertical position of vortex center) at $Bn = 500$ with two different values

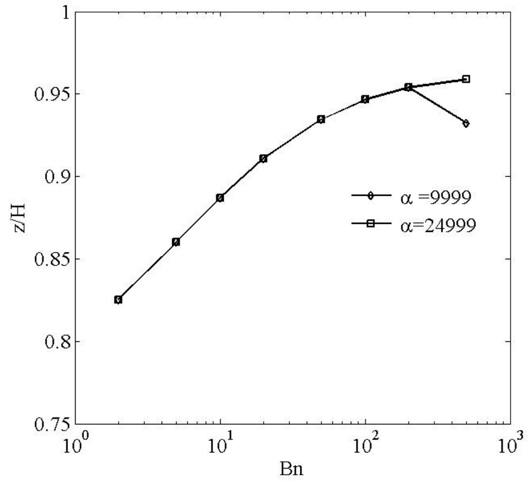

Figure 3.11: Vertical position of the primary vortex center z as a function of Bingham number

of α is obvious from Figure 3.11. Vortex center moves towards the moving lid with the increase of α. By keeping all other dimensionless numbers (Re, Bn, Db) constant, increment in α implies a high viscosity ratio. By keeping a high viscosity ratio, it is made sure that shear rates developed in the flow field are higher than the critical shear rate (refer Equations 2.35 and 2.36). This avoids the generation of wrong velocity fields which leads to the calculation of incorrect stream functions.

3.3.3 Comparison of results (Thixotropy vs. pseudo Bingham rheology)

Numerical experiments are performed for a detailed study of lid driven cavity flow problem with thixotropic liquids. To concentrate on the thixotropic effects rather than the inertial influence, Reynolds number is set to a low value ($Re = 0.5$). Deborah number and viscosity ratio are set to fixed values: $Db = 1$, $\alpha = 24999$. We start the simulations keeping network parameter $\lambda = 0$. Due to the network build up with time, liquid offers more resistance to moving lid which drives the vortex center closer to moving lid. A quantitative aspect of this phenomenon can be viewed in Figure 3.11 with $\alpha = 24999$. By keeping all other dimensionless numbers constant, Bn can be increased by decreasing k_1 (breakdown parameter) only. Reducing k_1 implies reducing the $-k_1\dot{\gamma}\lambda$ term in the

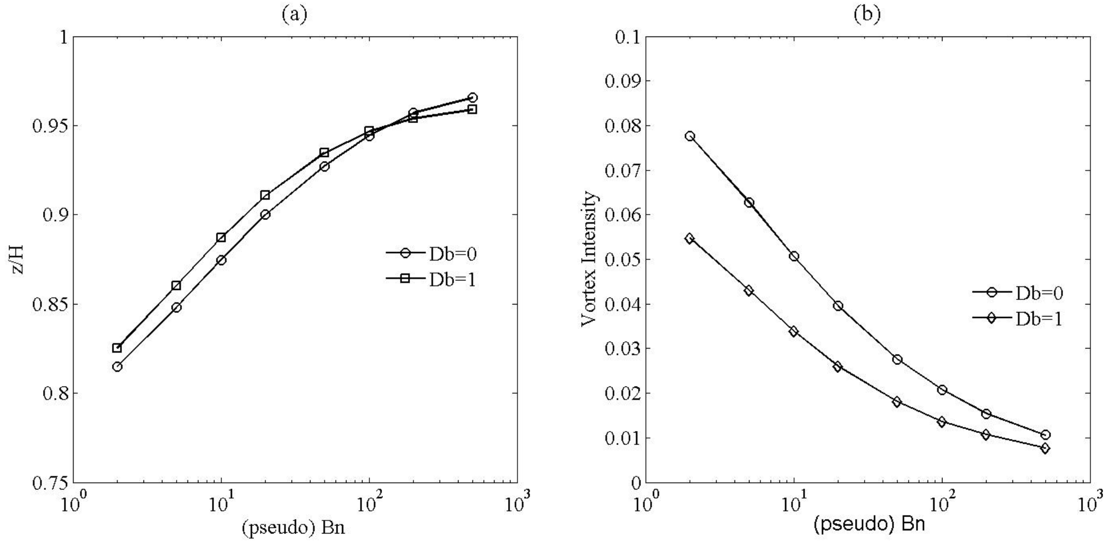

Figure 3.12: left: z-location of the vortex center as a function of Bn at $Re = 0.5$ and $Db = 0$ and 1, right: Vortex intensity at vortex center as a function of Bn at $Re = 0.5$ and $Db = 0$ and 1.

network parameter transport equation (Equation 2.26) which impacts the rate of change of λ making the flow evolution slower.

In the Figure 3.12(a) results are shown for $Db = 0$ and $Db = 1$. A Deborah number with zero value implies that the liquid time scale is very small in comparison to flow time scale i.e. the liquid properties are time independent (e.g. Bingham liquid). As Deborah number increases, liquid's flow response to external force decreases. This can be verified by comparing the vertical position of vortex center at two different Deborah numbers (Figure 3.12). For $Bn \leq 50$, liquid with higher Deborah number responds slowly to moving lid which draws the vortex center closer. As the Bingham number approaches higher values ($Bn > 50$), thixotropic rheology ($Db = 1$) results approach pseudo Bingham rheology ($Db = 0$) results. High reduction of k_1 results in quick build up of network, reaching to steady state very fast which is comparable to Bingham flow system. Other measurable quantity, vortex intensity, is also compared and shown in Figure 3.12(b).

Bibliography

[1] O. R. Beggary, Analytical and numerical studies of structure of steady separated flows, *J. Fluid. Mech.* 24 (1966) 113.

[2] M. Balsam, K. Krishna Prasad, On cavity flow at high Reynolds numbers, *J. Fluid Mech.* 79 (1977) 391.

[3] U. Ghia, K. N. Ghia, C. T. Shin, High-Re solutions for incompressible-flow using the Navier-Stokes equations and a multigrid method, *J. Comp. Phys.* 48 (1982) 387.

[4] M. A. Mendelson, P. -W. Yeh, R. A. Brown, R. C. Armstrong, Approximation error in finite element calculations of viscoelastic fluid flows, *J. Non-Newtonian Fluid Mech.* 10 (1982) 31.

[5] P. Pakdel, S. H. Spiegelberg, G. H. McKinley, Cavity flows of elastic liquids: two-dimensional flows, *Phys. Fluids* 9 (1997) 3123.

[6] A. M. Grillet, B. Yang, B. Khomani, E. S. G. Shaqfeh, Modeling of viscoelastic lid driven cavity flow using finite element simulations, *J. Non-Newtonian Fluid Mech.* 88 (1999) 99.

[7] K. -H. Sun, D. L. Pyle, M. J. Baines, N. Hall-Taylor, A. D. Fitt, Velocity profiles and frictional pressure drop for shear thinning materials in lid-driven cavities with fully developed axial flow, *Chem. Eng. Sc.* 61 (2006) 4697.

[8] M. Bercovier, M. Engleman, A finite-element method for incompressible non-Newtonian flows, *J. Comp. Phys.* 36 (1980) 313.

[9] E. Mitsoulis, Th. Zisis, Flow of Bingham plastics in a lid-driven square cavity, *J. Non-Newtonian Fluid Mech.* 101 (2001) 173.

[10] D. Vola, L. Boscardin, J. C. Latche, Laminar unsteady flows of Bingham fluids: a numerical strategy and some benchmark results, *J. Comp. Phys.* 187 (2003) 441.

[11] Z. Yu, A. Wachs, A fictitious domain method for dynamic simulation of particle sedimentation in Bingham liquids, *J. Non-Newtonian Fluid Mech.* 145 (2007) 78.

[12] D. K. Gartling, N. Phan-Thien, Numerical simulation of a plastic fluid in a parallel-plate plastometer, *J. Non-Newtonian Fluid Mech.* 14 (1984) 347.

[13] E. J. O'Donovan, R. I. Tanner, Numerical study of the Bingham squeeze film problem, *J. Non-Newtonian Fluid Mech.*, 15 (1984) 75.

[14] C. R. Beverly, R. I. Tanner, Numerical analysis of three-dimensional Bingham plastic flow, *J. Non-Newtonian Fluid Mech.* 42 (1992) 85.

[15] O. Botella, R. Peyret, Benchmark spectral results on the lid-driven cavity flow, *J. Comp. Fluids* 27 (4) (1998) 421.

[16] J. J. Derksen, Prashant, Simulations of complex flow of thixotropic liquids, *J. Non-Newtonian Fluid Mech.* 160 (2009) 65.

Chapter 4

Single sphere sedimentation

Sedimentation is a process in which a particle settles to the bottom of a container (filled with liquid) in which it is entrained. It is important to understand the behavior of particles settling in the viscous liquids to solve the problems involving fluidization, sedimentation and flow through packed beds. Moreover several engineering applications directly involve the settling of particles. A few examples include mineral ore processing, industrial crystallization, biological science, particle size analysis and fuel research. Sedimentation behavior of particles vary with many parameters such as size and shape of the particles, nature of liquid, size of container. To understand the mechanics of particle sedimentation, it is useful to start with hydrodynamics systems consisting single particle and consider the multi-particle systems later. In this chapter, we study the motion of a spherical particle in purely viscous Newtonian and non-Newtonian liquids. After having an insight into the motion of single sphere, a study of motion of two spheres is presented in chapter 5.

4.1 Sedimentation in Newtonian liquid

The theory of low Reynolds number Newtonian flow, also known as creeping flow has applications to various industries and natural phenomena involving small length and velocity scales and/or extremely viscous liquids. Stokes was the first to give a solution for the creeping flow problem around a sphere in Newtonian liquid of unbounded region.

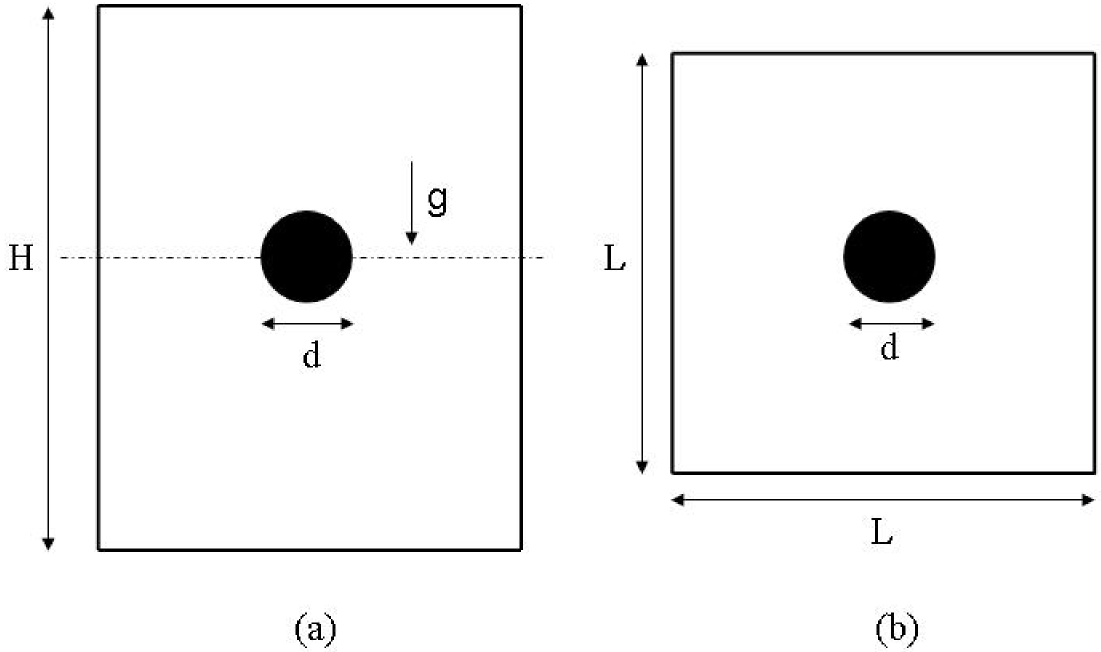

Figure 4.1: Flow definition of a sphere motion in a cylinder of square cross-section ($L \times L$); (a) Front view of cylinder (b) Top view of cylinder taken at cross-section marked by dashed line in (a).

A sphere falling under the effect of gravity is resisted by the drag (D) and buoyancy force and in equilibrium drag force is obtained by

$$D = \frac{4}{3}\pi(\frac{d}{2})^3(\rho_s - \rho_l)g \tag{4.1}$$

with ρ_s, ρ_l, d and g being the density of sphere, density of liquid, sphere diameter and the acceleration due to gravity, respectively. In case of small inertial effect Stokes derived the drag force expression which is read as

$$D = 3\pi d\mu U_\infty \tag{4.2}$$

where μ is the liquid viscosity while U_∞ is the terminal velocity of sphere settling in a medium of infinite size. We obtain the expression for terminal velocity U_∞ by combining the Equations 4.1 and 4.2.

$$U_\infty = \frac{d^2(\rho_s - \rho_l)g}{18\mu} \tag{4.3}$$

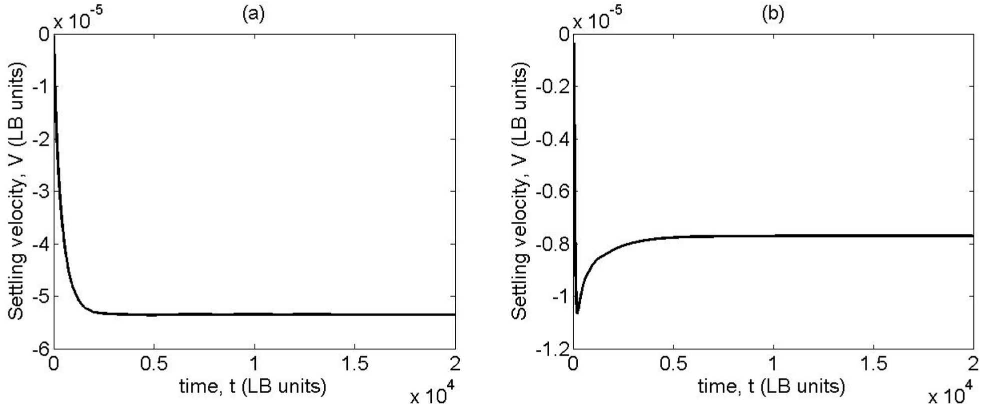

Figure 4.2: Time series of falling velocity of a single sphere settling in Newtonian liquid with L/d ratios (a) 5.0 and (b) 1.43 at $Re = 0.001$.

However in practical circumstances, motion of a sphere falling under gravity is retarded by the finite boundaries. In literature this effect has been often quantified as the wall factor which is defined as the ratio of the terminal velocity of a sphere in a bounded medium to that in an unbounded medium ($^{U_w}/_{U_\infty}$).

In this section, we aim to achieve the wall factors for a single sphere settling in a square cylinder of different cross-section sizes filled with Newtonian liquid and then compare them with experimental/numerical studies available in literature. The flow definition is shown in Figure 4.1. The numerical experiments are carried out with different values of d/L ratios and the steady state settling velocities (U_w) are measured for each of them. We use a sphere of diameter $d = 12$ and density $\rho_s = 32.0$. The grid size ($nx \times ny \times 213$) varies with L/d ratio as sphere diameter is fixed for all the simulations and $nx - 1 = ny - 1 = L$. The physical properties of Newtonian liquid are; density $\rho_l = 8.0$, viscosity $\mu = 0.8$. All the properties and parameters are defined in lattice-Boltzmann (LB) units. The sphere is released at the center of the cross-section of the cylinder with zero velocity. Throughout the numerical experiments, the Reynolds number is kept very low ($Re = 0.001$) and it is defined by the notion

$$Re = \frac{\rho_s U_\infty d}{\mu} \tag{4.4}$$

The velocity time series of a falling sphere for $L/d = 5.0, 1.43$ is plotted in Figure 4.2.

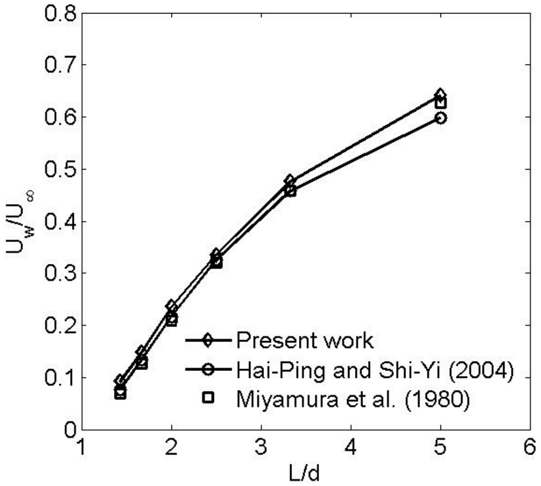

Figure 4.3: Wall factor as a function of sphere diameter to square cross-section side ratio at $Re = 0.001$; comparison with literature results (Miyamura et al. [1], Hai-Ping and Shi-Yi [2])

The velocity of sphere falling in a grid with $L/d = 1.43$ starts settling with a sharply increased velocity which gradually decreases and reaches steady state. This behavior is different from the one observed with $L/d = 5.0$. When sphere starts settling in the grid with $L/d = 1.43$, it initially falls with a greater velocity because the flow field is not fully developed and the interaction with walls is partial. Once the flow develops with time, strong friction due to very close walls decelerate the sphere. The sphere moves with steady state velocity once friction force due to walls and drag force are counterbalanced by the net gravitational force. Figure 4.3 displays the wall factor (U_w/U_∞) as a function of L/d ratio. The terminal velocity of a sphere in bounded region is always less than the terminal velocity of an unconfined sphere. The retardation effect of walls increases as they come closer to the moving sphere. Our simulation results are compared with the experimental data obtained by Miyamura et al. [1]. They used a square cylinder to investigate the wall factors with creeping flow of a sphere in Newtonian liquid. A close agreement is seen between our simulation results and literature data.

4.2 Sedimentation in Bingham liquid

4.2.1 Introduction

Many industrial processes deal with the sedimentation of particles in liquids which possess yield stress. Therefore it is of practical importance to have an understanding of physics involved in this solid-liquid suspension. Research studies focused on the falling of a sphere in Bingham liquids date back several decades. Volarovich and Gutkin [3] were the first to report that a sphere falling in a Bingham liquid is surrounded by a liquid envelope which separates the sphere from outer unyielded region of liquid. One of the theoretical problems experienced in early studies was to specify the shear stresses in the region surrounding the sphere. To handle this, Andres [4] put forth the concept of concentric sphere of influence which surrounds the falling sphere, however no idea was given to explain the effect of velocity of the material flow on such a region. Valentik and Whitmore [5] experimentally determined the terminal velocity of a sphere with an objective of gaining better insight into the stress and velocity distribution in the region surrounding the falling sphere. Ansley and Smith [6] postulated the shape and extents of yielded/unyielded regions surrounding the sphere using slip line theory. Yoshika et al. [7] confirmed the existence of stagnation points at the front and back of the sphere for any finite value of the liquid's yield stress.

Using the variational formulations, Duvaut and Lions [8] proved that a unique solution existed for the creeping flow of Bingham liquids in both interior and exterior regions. Assuming the results of Newtonian flow problem square-integrable, they also claimed that the solution of Bingham liquid problem approaches the Newtonian result as the yield stress approaches zero. Beris et al. [9] pointed out the invalidity of this assumption for a sphere in unbounded liquid due to the different results suggested by variational studies. Some of the earlier studies [6, 10, 11] concentrated on measuring the drag coefficient for a falling sphere as a function of yield stress and plastic viscosity of liquid. In a classical work, Beris et al. [9] numerically determined the velocity field, pressure field, shape of the yield surfaces and drag coefficient for the creeping flow around a sphere in an unbounded Bingham liquid. More recently Atapattu et al. [12, 13] extensively investigated the wall effects and their effects on drag coefficient. Blackery and Mitsoulis [14] reported the drag coefficients for different tube/sphere diameter ratios. Liu et al. [15] and Yu and Wachs [16] obtained the shape and extents of yielded/unyielded regions and compared their results with literature.

In subsequent subsections, a numerical solution of a sphere settling in Bingham liquid is presented using lattice-Boltzmann scheme as numerical tool.

4.2.2 Flow definition and dimensionless numbers

The interaction of a single sphere with Bingham liquid inside a cylinder has been dealt with two ways. In the first manner the sphere is assumed stationary while the liquid and the cylinder walls move with a constant velocity (flow past fixed sphere). This scheme is easier to implement since it eliminates the time dependence associated with the problem of a moving sphere. In other scheme, the liquid and cylinder walls are stationary while sphere falls in the cylinder under the influence of an external force. We study both of the cases here and their flow definitions are shown in Figure 4.4.

The flow is governed by two dimensionless numbers namely Reynolds number and Bingham number which are displayed by the notions

$$Re = \frac{\rho_l U_c d}{\mu_p} \tag{4.5}$$

$$Bn = \frac{\tau_0 d}{\mu_p U_c} \tag{4.6}$$

where τ_0, μ_p are yield stress and plastic viscosity of Bingham liquid, respectively. The symbol U_c is the characteristic velocity which is defined differently for both cases. In case of fixed sphere problem, the terminal velocity of the sphere V is taken as characteristic velocity and dimensionless numbers are suffixed with letter T.

$$Re_T = \frac{\rho_l V d}{\mu_p} \tag{4.7}$$

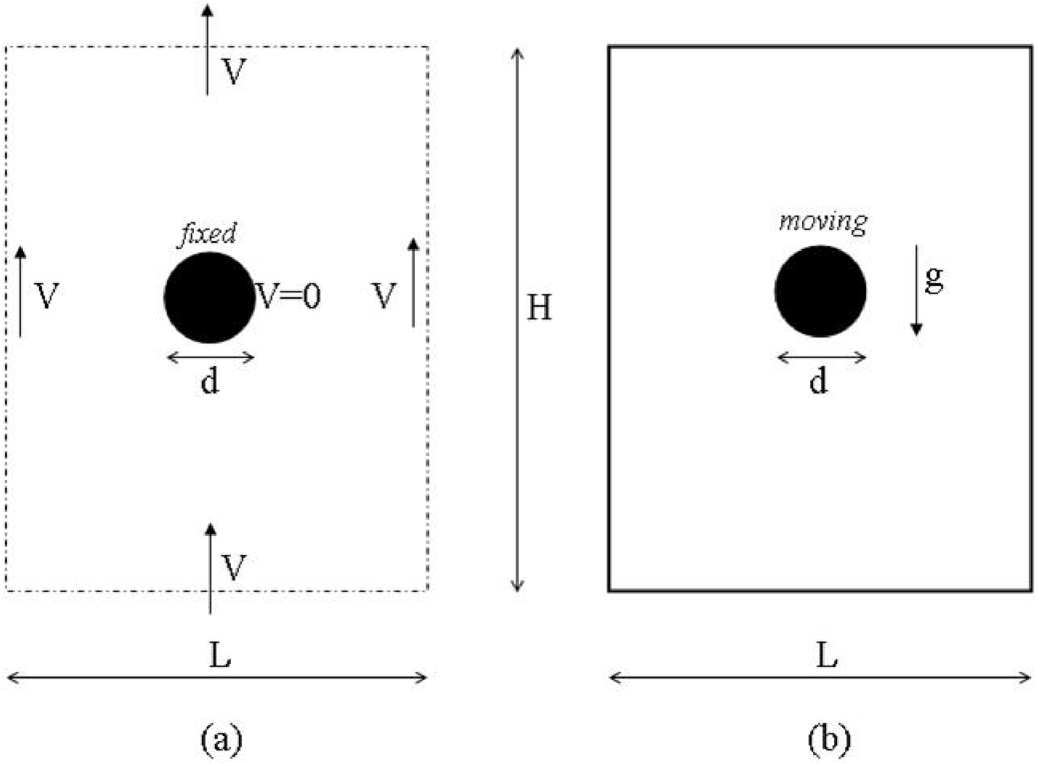

Figure 4.4: Flow definition of a sphere motion in a cylinder of square cross-section ($L \times L$) filled with Bingham liquid; (a) The liquid and cylinder walls move with velocity V, sphere is fixed (b) The sphere falls under the influence of gravity; the liquid and cylinder walls remain stationary.

$$Bn_T = \frac{\tau_0 d}{\mu_p V} \tag{4.8}$$

While handling the problem with a moving sphere, the characteristic velocity is calculated using Equation 4.3 (with viscosity $\mu = \mu_p$) and dimensionless numbers are suffixed with letter S.

$$Re_s = \frac{\rho_l U_\infty d}{\mu_p} \tag{4.9}$$

$$Bn_s = \frac{\tau_0 d}{\mu_p U_\infty} \tag{4.10}$$

4.2.3 Results - Fixed sphere case

Prior to demonstrate the results, we revisit the flow definition depicted by Figure 4.4 (a). A sphere, considered as frame of reference, remains fixed inside a three dimensional square cylinder which moves along with Bingham liquid with a uniform velocity V. This velocity V is taken as terminal velocity of sphere in Bingham liquid. The boundary conditions are, uniform velocity V along the cylinder walls and at inlet-outlet while no-slip at the surface of sphere.

Once V and other liquid parameters (ρ_l, μ_p and τ_0) are fixed, one can set the flow governing dimensionless numbers Re_T and Bn_T (Equation 4.7 and 4.8). In a number of previous studies [9, 14, 16] researchers have measured the ratio of Stokes velocity to terminal velocity (termed as Stokes drag coefficient by Beris et al. [9]) with yield stress of Bingham liquid at very low inertial effects. In this case too, for the sake of comparison, we solve for the drag force (D) exerted on sphere by the liquid and further calculate the Stokes velocity (U_∞) using the Equation 4.2 (with viscosity $\mu = \mu_p$). To avoid the conflict with the classical drag coefficient definition, we refrain from using the term Stokes drag coefficient and call it a velocity ratio which is defined as

$$v_r = \frac{U_\infty}{V} \tag{4.11}$$

To mimic creeping flow, the Reynolds number chosen is very small ($Re = 0.001$) and we use a square cylinder ($L/d = 4$, $d = 12$) filled with Bingham liquid of density $\rho_l = 8$ ($\rho_s/\rho_l = 4$), plastic viscosity $\mu_p = 0.032$ and viscosity ratio $\mu_r = 10^5$. The three dimensional grid size is $49 \times 49 \times 73$. The simulations are performed over a range of liquid's yield stress ($Bn_T = 0.1, 1, 5, 10, 20, 50, 100, 200$) and the velocity ratio (Equation 4.11) is calculated for each case. A pictorial depiction of the effect of yield stress of liquid is presented in Figure 4.5. The unyielded regions progressively grow with the increase of yield stress and the interaction of yielded Bingham liquid with cylinder walls decreases. These results qualitatively agree well with the results reported by Blackery and Mitsoulis [14]. The occurrence of black polar caps with $Bn_T = 50$ (two unyielded regions at stagnation points), observed by both Beris et al. [9] and Blackery and Mitsoulis [14], and solid regions on each side of sphere with $Bn_T = 5, 50$ proposed by Ansley and Smith [6] confirms the validity of our results.

A quantitative comparison of our results with literature is shown in Figure 4.6. When we increase the yield stress (i.e. Bn_T) of the liquid, the viscous forces dominate and they assist the resistance offered by the fixed sphere to the motion of the liquid. Since the liquid travels with a constant velocity V in all the simulations, the drag force exerted on sphere increases with increase of yield stress of liquid. This increased drag force leads to the increased Stokes velocity (Equation 4.2), therefore increased velocity ratio, which is confirmed in the Figure 4.6. There is a slight difference between the flow definitions used by us and Blackery and Mitsoulis [14]. They used a cylinder with circular cross-section whose diameter is four times the diameter of sphere while we have used a cylinder with square cross-section whose one side is four times the diameter of sphere. Obviously in square cylinder the retardation effect of walls should be less pronounced than the circular cylinder and we should expect smaller velocity ratios (U_∞/V) than those obtained by Blackery and Mitsoulis [14]. One can question the apparent excellent agreement of results obtained by both the studies which are shown in Figure 4.6, however it is important to note that both the axes are logarithmic which hide the minor deviation in the results. The actual deviations between the results shown in Figure 4.6 can be seen in Table 4.1.

Miyamura et al. [1] performed experiments to calculate the wall factors of single solid sphere settling in a square cylinder filled with a Newtonian liquid and then compared them with the wall factors obtained with circular cylinder [17] keeping other parameters unchanged. They reported that the retardation effect on the terminal velocity due to wall proximity is less severe with square cylinder and the sphere settles with a greater terminal velocity which is around 5% higher than that measured with circular cylinder. Close to the Newtonian limit ($Bn_T = 0.1$), we too observe a 6.6% lesser velocity ratio (i.e. 6.6% higher terminal velocity) which is in close agreement with the results reported by Miyamura et al. [1]. Once the yield stress of liquid is appreciably high ($Bn_T > 0.1$), unyielded region around sphere grows progressively (refer Figure 4.5) which restricts the

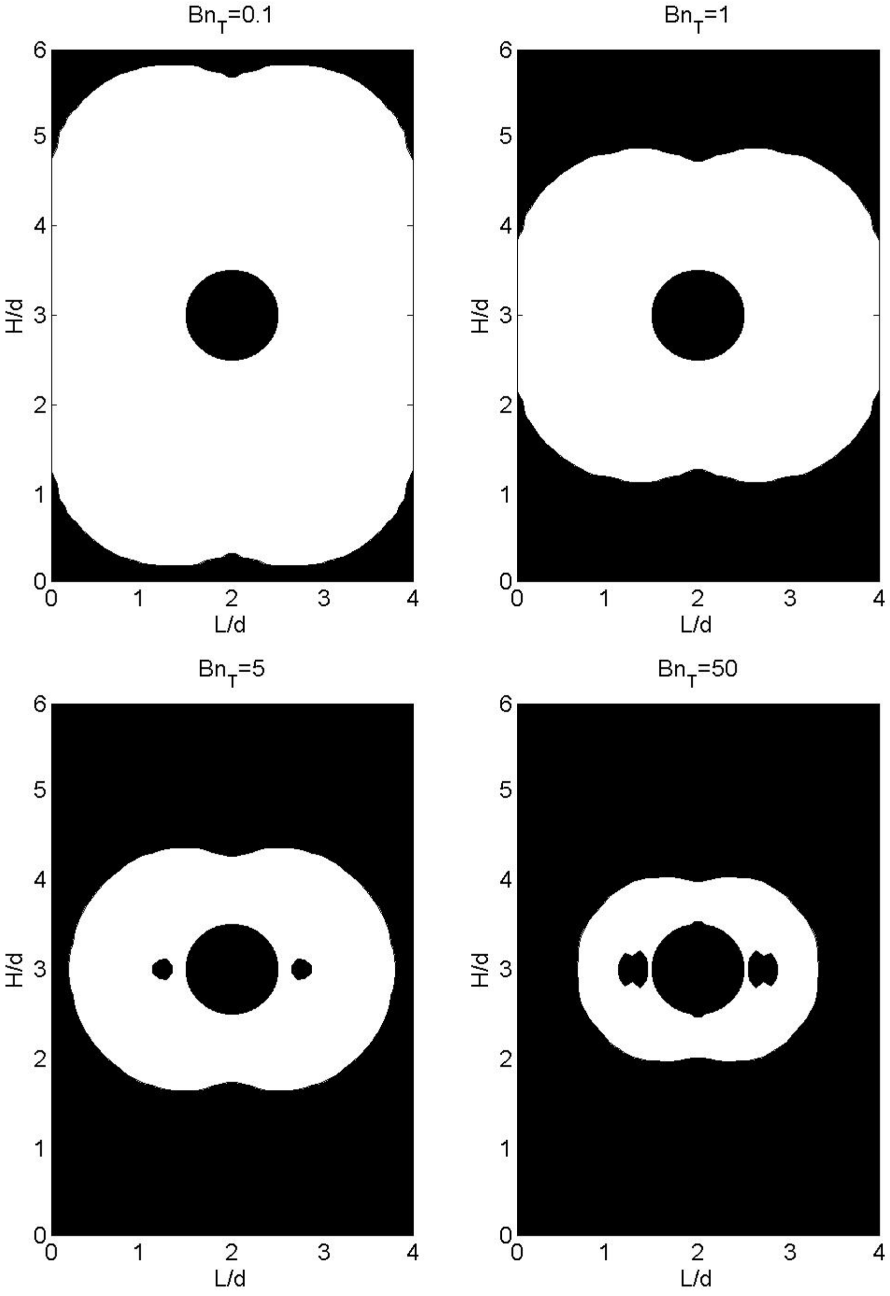

Figure 4.5: The yielded (white) and unyielded (black) regions for flow of a Bingham liquid around a fixed sphere contained in a square cylinder with $4:1$ ratio of L/d

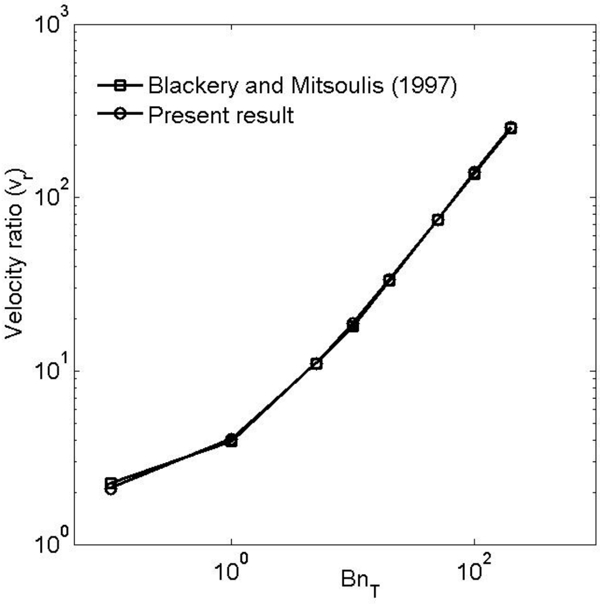

Figure 4.6: Velocity ratio (v_r) as a function of Bingham number (Bn_T) at $Re = 0.001$; comparison with literature results (Blackery and Mitsoulis [14])

interaction of flow field with walls. Therefore in this scenario (higher yield stress), it can be expected that difference in cylinder geometry does not influence our results from literature considerably. This is well supported by the minor deviations (shown in Table 4.1) observed with higher yield stress flow simulations.

4.2.4 Results - Moving sphere case

Having solved the creeping flow problem of a sphere in Bingham liquid using a comparatively easy approach, we turn our attention to mimic the same problem with a different flow definition where sphere falls in a stationary square cylinder filled with Bingham liquid under the influence of gravitational force (refer Figure 4.4 (b)). A zero velocity boundary condition (for details refer appendix C) is imposed along the walls of cylinder and no-slip boundary condition is considered for surface of the sphere. For this case, we use the set of dimensionless numbers defined by Equations 4.9 and 4.10. The numerical parameters and grid size used in this case remain same as with fixed sphere approach. It is important to mention here that in this case our objective is to obtain the terminal velocity V of the sphere settling in Bingham liquid. The gravitational force (i.e. g) is

Bn_T	0.1	1	10	20	50	200	
v_r (Blackery and Mitsoulis)	2.24	3.92	18.04	33.13	74.11	250.25	$R1$
v_r (Present work)	2.10	4.06	18.84	33.47	74.77	252.96	$R2$
% difference ($\frac{R2 - R1}{R2} \times 100$)	-6.66	3.45	4.25	1.02	0.88	1.07	

Table 4.1: Velocity ratio (v_r) as a function of Bingham number (Bn_T)

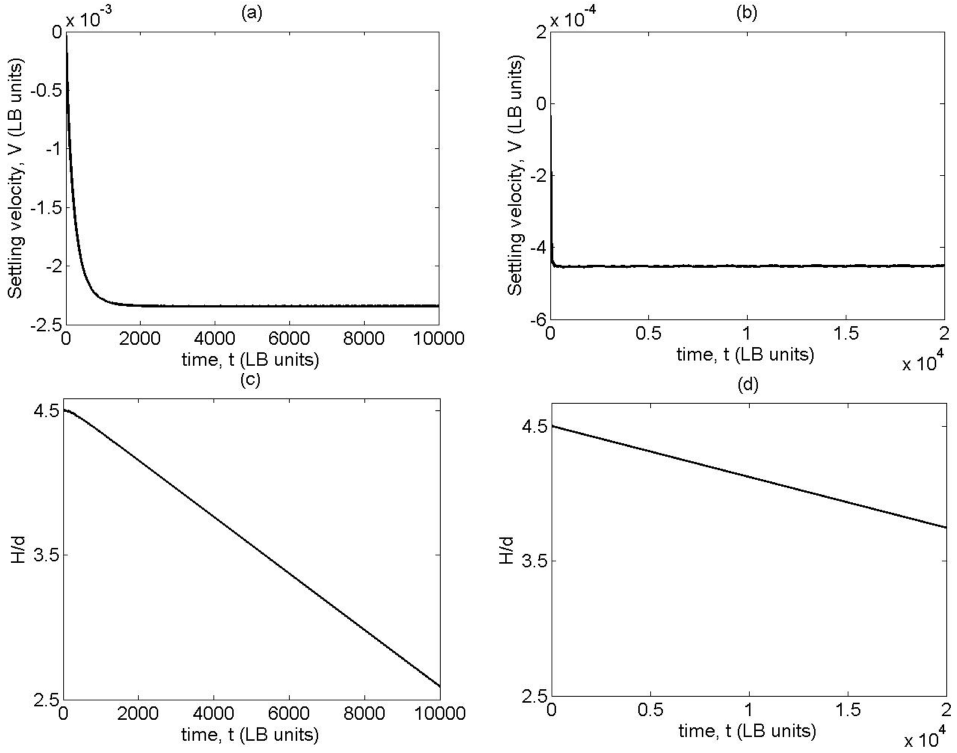

Figure 4.7: Time series of settling velocity and distance traveled in Bingham liquid with $Bn_s = 0.21$ (left) and 0.53 (right) at $Re_s = 1$.

set in such a way that Reynolds number $Re_s = 1$. The primary reason of choosing this comparatively higher Reynolds number is literature work with which our simulations are validated for moving sphere case. Also, by choosing $Re_s = 1$, the effective Reynolds numbers (based on the terminal velocity of sphere) are in the order of 10^{-1} to 10^{-2} which are fairly low Reynolds numbers.

The simulations are performed with various values of yield stress of the liquid ($Bn_s = 0.05, 0.21, 0.36, 0.53, 0.60, 0.66, 0.72$). The settling velocity and distance traveled by a sphere, falling in Bingham liquid with $Bn_s = 0.21, 0.53$, are plotted in Figure 4.7 as a function of time. Clearly, the terminal velocity decreases with increase in the yield stress of the Bingham liquid. The unyielded and yielded regions coupled with steady state velocity vectors are shown in Figure 4.8. As observed previously (Figure 4.5), confinement of sphere by unyielded region increases progressively with the increase of liquid's yield stress. The shape and extent of these regions are in qualitative agreement with Beris et al. [9], Blackery and Mitsoulis [14], Liu et al. [15] and Yu and Wachs [16]. The recirculating regions observed on both sides of the sphere are consequences of the finite size of square cylinder. It is clear that the centers of recirculating regions shift closer to the sphere with the increase of Bingham number (i.e. yield stress) which is qualitatively similar to the results reported in literature [9, 13, 14]. We observe polar cap (black) with $Bn_s = 0.36, 0.53$ only at trailing point of sphere. Since the stagnation point does not exist at leading side of the moving sphere, no polar cap is observed at leading side of the sphere.

A quantitative comparison of our results with literature is shown through the variation of velocity ratio ($^{U_\infty}/_{V}$) with Bingham number (Bn_s) in Figure 4.9. The results obtained by us deviate from available literature results at moderate to high Bingham numbers ($Bn_s > 0.36$). The possibility of considerable influence due to square cylinder is quite unlikely at high Bingham numbers ($Bn_s = Bn_T/v_r$; $Bn_s = 0.36$ corresponds to $Bn_T = 2.4$) as discussed previously in subsection 4.2.3. The discrepancy in the results with moderate to high Bingham numbers can be caused by different numerical methods, however the exact reason remains indeterminate so far. An attempt is made to demonstrate these results in Figure 4.10 which plots velocity ratio as a function of Bingham number Bn_T. In this figure, all the studies are found to be in good agreement with each other due to the presence of terminal velocity V in both abscissa and ordinate which supposedly cancels out the differences while plotting.

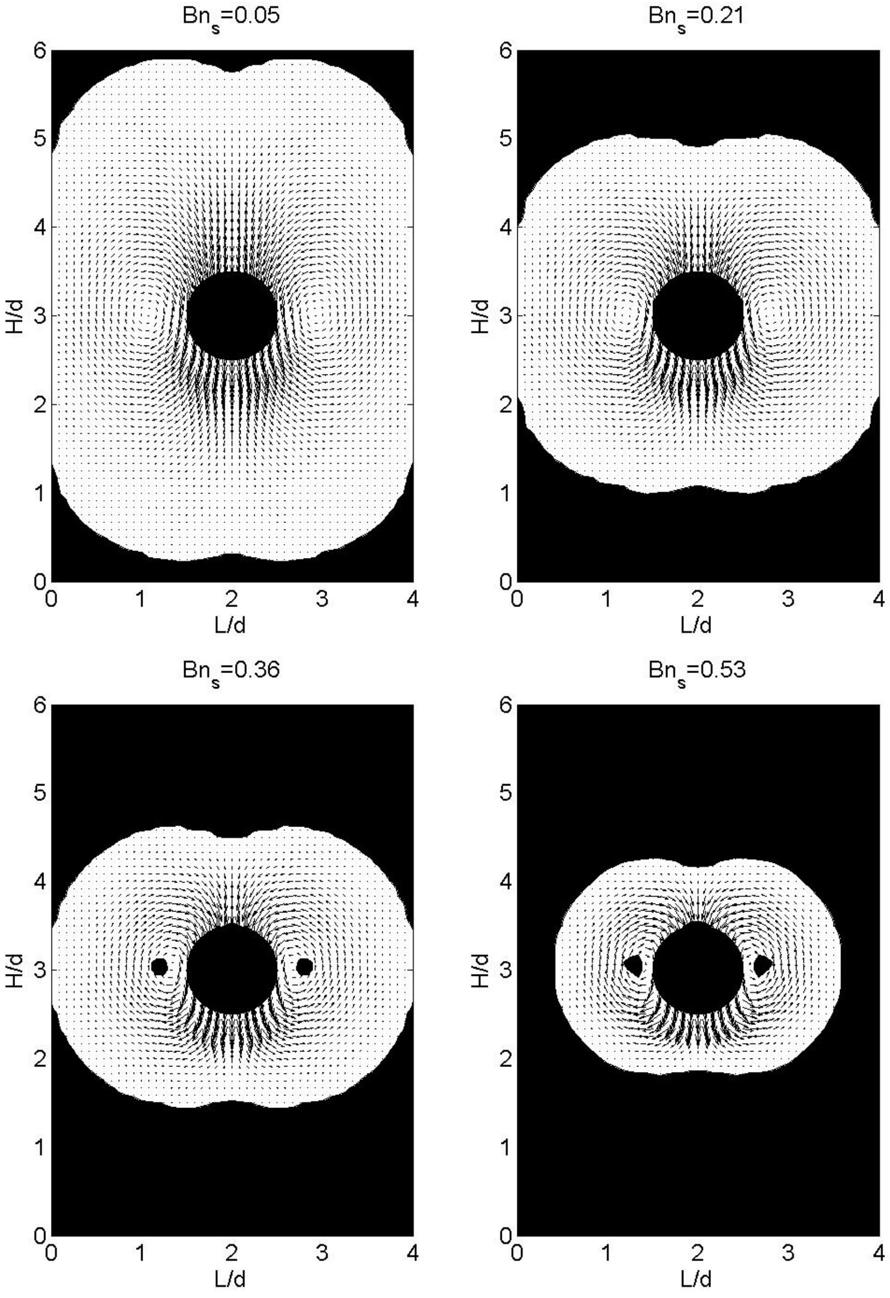

Figure 4.8: Yielded (white)/unyielded (black) regions together with velocity vectors for a sphere settling in a square cylinder filled with Bingham liquid.

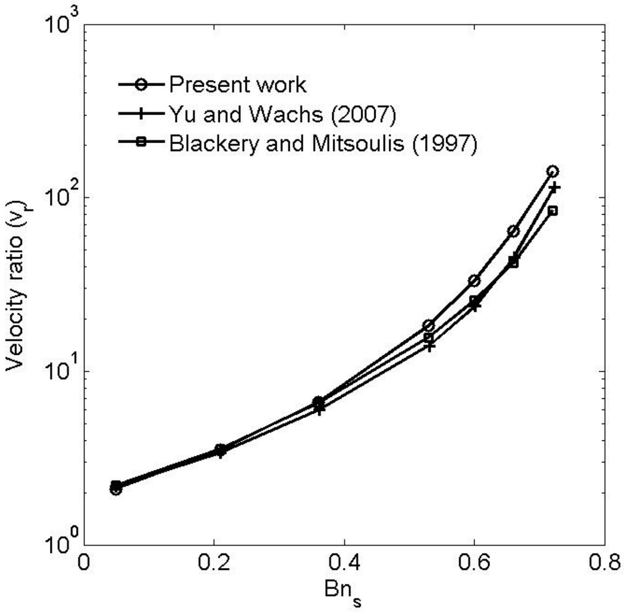

Figure 4.9: Velocity ratio (v_r) as a function of Bingham number (Bn_s) at $Re_s = 1$; comparison with literature results (Blackery and Mitsoulis [14], Yu and Wachs [16])

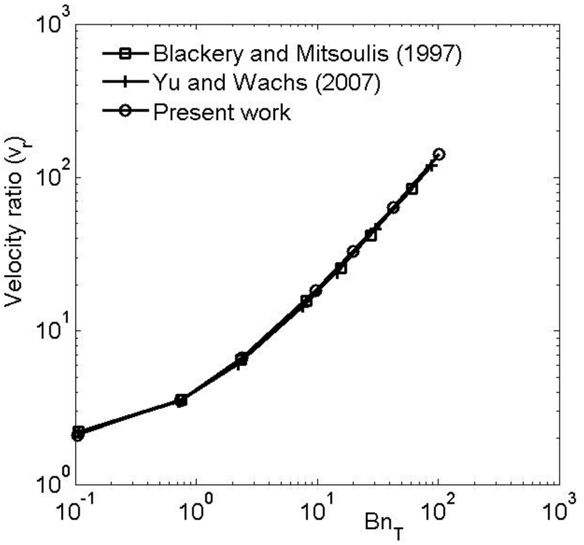

Figure 4.10: Velocity ratio (v_r) as a function of Bingham number (Bn_T); comparison with literature results (Blackery and Mitsoulis [14], Yu and Wachs [16])

4.3 Sedimentation in thixotropic liquid

4.3.1 Introduction

Thixotropic liquids are usually known by change in their viscosity with time due to the change of internal structure caused by shear. Apart from this, they often exhibit yield stress and shear-thinning behavior. Clays or muds are very good examples of thixotropic liquids. In the mining industry, a viscous mud is used to remove the rock cutting from the bottom during drilling process. The other major functionality of this viscous mud is to hold the solid particles in suspension when injection of mud is stopped. The mud develops a network with time of rest which hinders the settling of solid particles. This behavior is usually termed as aging of the liquid.

A number of early experimental studies [5, 6] of liquids showing yield stress raised a major concern regarding the poor reproducibility of settling data. Atapattu et al. [13] performed a rigorous experimental study on creeping sphere motion in the liquids, which exhibit yield stress and shear-thinning behavior, and reported a poor reproducibility of settling data without releasing 4 to 10 spheres with very small time difference. Same problem was noticed by Hariharaputhiran et al. [18] in their study of settling of spheres in viscoplastic liquids. Recently Ferroir et al. [23] pointed out that consideration of time-dependent properties of liquids could be the main reason of the problems reported above. They examined the effect of thixotropy on the settling of solid objects in pasty materials possessing yield stress and concluded that settling behavior of the object depends upon the initial state of the material and Reynolds number of the flow system. Chafe and de Bruyn [25] conducted the sphere settling experiment with bentonite clay suspension and measured the steady state drag force on the sphere. They reported the increment in drag force with the aging time of the suspension. Gueslin et al. [26] used particle image velocimetry technique (PIV) in the experiments to measure the flow field of a spherical particle in Laponite clay suspension. They showed that apparent yield stress and shear thinning properties of a Laponite clay suspension are direct function of aging time. Tabuteau et al. [27] used a clay suspension, showing yield stress and rheological aging, to qualitatively confirm the results obtained by Chafe and de Bruyn [25].

4.3.2 Flow definition and dimensionless numbers

The flow definition of sphere sedimentation with thixotropic liquid is same with moving sphere sedimentation in Bingham liquid (see Figure 4.4 (b)). The sphere falls through the thixotropic liquid under the effect of gravity in a closed square cylinder. The sphere diameter d and the Stokes terminal velocity in an unbounded medium (defined by Equation 4.2) are considered as characteristic length and velocity, respectively with viscosity μ being equal to μ_∞, the infinite shear viscosity of thixotropic liquid. Based on characteristic parameters, four dimensionless numbers Reynolds number (Re), (pseudo) Bingham number, purely viscous Deborah number (Db) and viscosity ratio ($\alpha + 1$) are defined as

$$Re = \frac{\rho_l U_\infty d}{\mu_\infty} \tag{4.12}$$

$$(pseudo)\ Bn = \alpha \frac{k_2 d}{k_1 U_\infty} \tag{4.13}$$

$$Db = \frac{U_\infty}{d k_2} \tag{4.14}$$

$$\alpha = \frac{\mu_0}{\mu_\infty} - 1 \tag{4.15}$$

with μ_0 being zero shear viscosity while k_1 and k_2 are thixotropic parameters defined in chapter 2 (Euqation 2.35). Zero velocity boundary conditions imposed on cylinder walls can be seen in appendix C.

4.3.3 Effect of aging

It has been widely observed that some liquids (e.g. drilling mud) exhibit highly viscous behavior when not sheared. This highly viscous behavior is attributed to the development of a network with time of rest. As long as the liquid ages, as much as the network integrity increases. In present study, we are using a dimensionless parameter λ to define the integrity of liquid's network. A detailed description of evolution of network parameter λ can be seen in chapter 2. If shear is removed ($\dot{\gamma} = 0$ and $u_i = 0$) from the steady state flow of a thixotropic liquid, the network breakdown process stops and only the build-up process remains in the system. Equation 2.26 can now be written as

$$\frac{\partial \lambda}{\partial t} = k_2(1 - \lambda) \tag{4.16}$$

Equation 4.16 can be solved for λ with boundary condition $\lambda = 0$ at $t = 0$ which leads to the expression

$$\lambda = 1 - e^{-k_2 t} \tag{4.17}$$

Thus the integrity of network increases with aging time and its numerical value varies from $\lambda = 0$ at $t = 0$ to $\lambda = 1$ at $t \to \infty$. From the basic knowledge of physics of creeping flow of a sphere, we know that the terminal velocity (V) of sphere is inversely proportional to the liquid viscosity μ (apparent viscosity μ_a in case of non-Newtonian liquids).

$$V \propto \frac{1}{\mu_a} \tag{4.18}$$

Using the apparent viscosity expression defined by Equation 2.27 and assuming the proportionality constant as κ, Equation 4.18 can be written as

$$V = \frac{\kappa}{\mu_\infty(1 + \alpha\lambda)} \tag{4.19}$$

In case of steady state flow with no shear, λ can be substituted by the expression given in Equation 4.17 resulting in following expression

$$V = \frac{\kappa}{\mu_\infty[1 + \alpha(1 - e^{-k_2 t})]} \tag{4.20}$$

Rearranging the Equation 4.20, we obtain

$$(1+\alpha) - \frac{\kappa}{V\mu_\infty} = \alpha e^{-k_2 t} \tag{4.21}$$

The terminal velocity can be calculated analytically at limiting values of time using Equation 4.21 and read as

$$V(t) = \begin{cases} \dfrac{\kappa}{\mu_\infty} & t \rightarrow 0 \\ \\ \dfrac{\kappa}{\mu_\infty(1+\alpha)} & t \rightarrow \infty \end{cases} \tag{4.22}$$

The ratio of no network terminal velocity to complete network terminal velocity can be derived from Equation 4.22 as

$$\frac{V(0)}{V(\infty)} = \alpha + 1 \tag{4.23}$$

In order to systematically investigate the effect of aging on sedimentation of a sphere, a number of numerical experiments are carried out with the thixotropic liquid of different ages. The aging time of the liquid is calculated using Equation 4.17 with the different values of network parameter ($\lambda = 0.05, 0.20, 0.35, 0.55, 0.65, 0.72, 0.85$). For the numerical experiments, the Reynolds number and Deborah number are set as; $Re = 1$, $Db = 1$ while the grid size is chosen as $97 \times 97 \times 97$. It is important to point out here that the Reynolds number ($Re = 1$) used in our simulations is based on the Stokes terminal velocity (with $\mu = \mu_\infty$). The maximum value of effective Reynolds number (based on terminal velocity V and μ_∞) for each simulation is of the order of 10^{-2} or less. The value of viscosity ratio is chosen in such a way that $\alpha = 99999$.

A sphere of diameter $d = 12$ and density $\rho_s = 4\rho_l$ ($\rho_l = 8$) is allowed to fall due to gravity and time series of falling velocity and distance travelled are displayed in Figure 4.11. Terminal velocity of the sphere is plotted against the aging time of liquid in Figure 4.12. The terminal velocity of sphere decreases with aging time and its variation is loosely matched by an exponential fit (straight line) which is defined by the expression

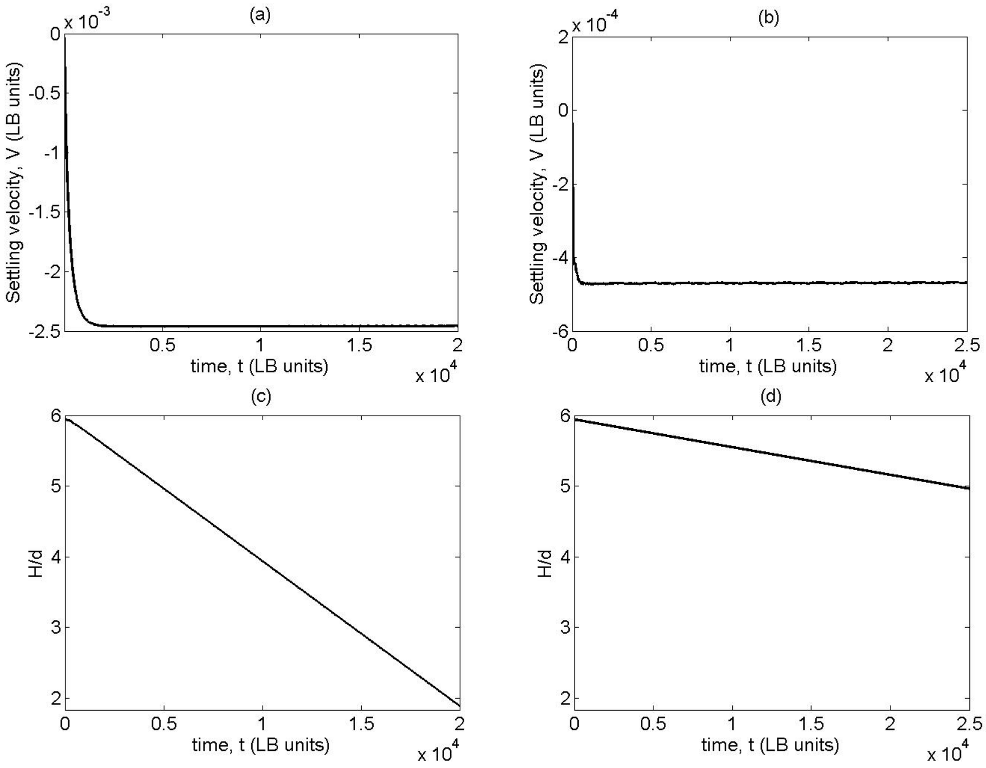

Figure 4.11: Time series of settling velocity and distance traveled in thixotropic liquid with age (left) $t_a = 340$ and (right) $t_a = 1087$ $Re = 1$.

$$V = V_0 e^{-k_2' t} \tag{4.24}$$

with V_0 and $1/k_2'$ being the sphere terminal velocity at $t = 0$ and the characteristic build-up time for solid-liquid suspension, respectively. The idea of getting an exponential fit is inspired by the work due to Gueslin et al.[26]. We observe some deviation between exponential fit and our simulation data with large aging time ($t > 1000$). This deviation is caused by the particular viscosity model (Equation 2.27) used in our simulations according to which terminal velocity varies with aging time as given by Equation 4.21. One can observe that for a finite value of α, this viscosity model gives a non zero terminal velocity when $t \to \infty$ (Equation 4.22) while as per Equation 4.24 $V \to 0$ when $t \to \infty$. We can expect a close match with exponential fit using a very large value of α. Increasing the value of α (i.e. viscosity ratio; see Equation 2.31) means the increment in zero shear viscosity which pushes the steady state thixotropic rheology closer to dual-

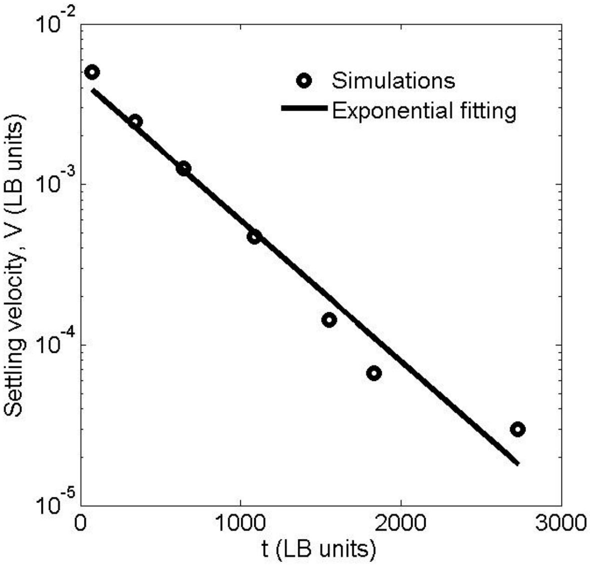

Figure 4.12: Terminal velocity of a sphere in thixotropic liquid as a function of aging time at $Re = 1$; Straight line is exponential fit to simulation data.

viscosity Bingham model (refer Figure 2.6). The idea of this whole exercise is that indeed thixotropic liquid behaves as true yield stress liquid and by using a large viscosity ratio in simulations, a close match can be expected between simulation data and the exponential fit given by Equation 4.24. Also these results qualitatively agree with the experimental observations made by Gueslin et al. [26].

It is important to note here that there is a substantial difference between the time constants $1/k_2$ used in simulations and $1/k_2'$ extracted from exponential fitting. The constant $1/k_2$ is liquid parameter alone while the constant $1/k_2'$ depends upon the entire solid-liquid system and would change with the properties of settling sphere. Through these simulations we find that

$$\frac{k_2'}{k_2} \approx 3 \tag{4.25}$$

which indicates that network of thixotropic liquid builds up approximately 3 times faster with sphere settling than that with liquid alone.

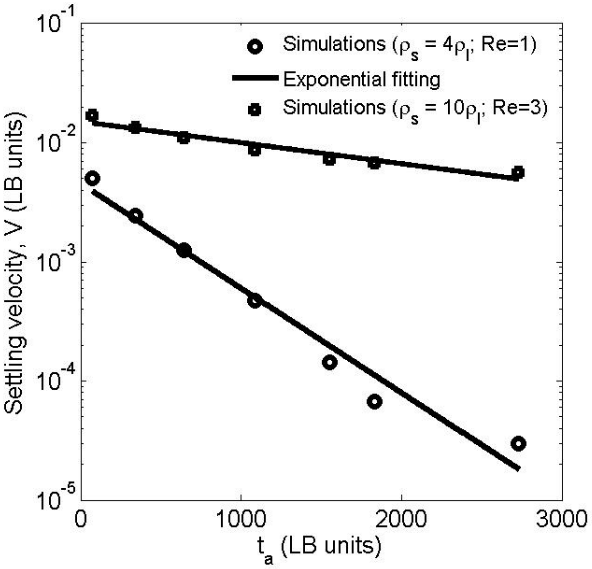

Figure 4.13: Terminal velocity of spheres in thixotropic liquid as a function of aging time at $Re = 1$ and $Re = 3$; Straight line is exponential fit to simulation data

4.3.4 Effect of Reynolds number

In this subsection, we study the settling behavior of a solid particle ($\rho_s = 10\rho_l$) which exert higher inertial forces than those due to the solid sphere studied in previous subsection. All the dimensionless numbers are unchanged (except Reynolds number; $Re = 3$) and same procedure is employed to obtain the settling velocities of sphere in thixotropic liquid with different aging times as done in previous subsection. Figure 4.13 displays the terminal velocity of spheres ($\rho_s = 4\rho_l, 10\rho_l$) as a function of aging time, measured separately. In this case too, terminal velocity decreases with aging time and the variation is well described by the Equation 4.24. The settling velocities of heavier sphere are greater than those of lighter sphere at same aging time. However the ratio of heavier sphere terminal velocity to lighter sphere terminal velocity is smaller at small aging times whereas the ratio is larger at large aging times. This is in qualitative agreement with the results reported by Gueslin et al. [26]. The characteristic build-up time ($1/k_2'$) for solid-liquid suspension of heavier particle is related with liquid time constant ($1/k_2$) as

$$\frac{k_2'}{k_2} \approx 0.6 \tag{4.26}$$

which shows that network recovery process slows down with heavier particle. In contrast to the case with lighter sphere, on this occasion the motion of (heavier) sphere catalyzes the breakdown process and retards the association process.

4.3.5 Fore-aft asymmetry

The fore-aft symmetry (symmetry of flow field before and after the sphere) has been a distinguished feature of the creeping flow of a sphere moving in a Newtonian or Bingham liquid [9, 14]. In contrast to this, we observe a fore-aft asymmetry in the case of thixotropic liquid at low Reynolds number flows. A qualitative comparison of fore-aft flow fields in a Newtonian, Bingham and thixotropic liquid is displayed in Figure 4.14. The fore-aft asymmetry displayed with thixotropic liquid (Figure 4.14 (c)) is due to its time-dependent behavior. As the sphere moves, the sheared liquid has lesser viscosity than the liquid approached by the sphere. In case of Newtonian and Bingham liquids, the viscosity remains unchanged before and after the moving sphere which makes the flow symmetric. To illustrate the time dependent behavior of thixotropic liquid, a contour plot of ratio of apparent viscosity to infinite shear viscosity ($^{\mu_a}/_{\mu_\infty}$) coupled with streamlines is provided in Figure 4.15.It is clear that the liquid is lesser viscous in downstream region compared to the same area of upstream region. This contour plot is in qualitative agreement with the viscosity contours shown by Yu et al. [31] in their numerical study of particle sedimentation in shear-thinning liquids with memory. The lack of fore-aft symmetry is consistent with the findings of some experimental studies [26, 32] conducted with a yield stress shear thinning liquid.

Another feature related to yield stress shear thinning liquids reported by these studies is the upward flow in the sphere's wake which is also termed as negative wake. In present study we do not observe the existence of negative wake. Exploring the literature further, we find out that the existence of negative wake has been often reported by numerical studies [33, 29, 30, 31] using viscoelastic constitutive models. Gueslin et al. [26] and Putz

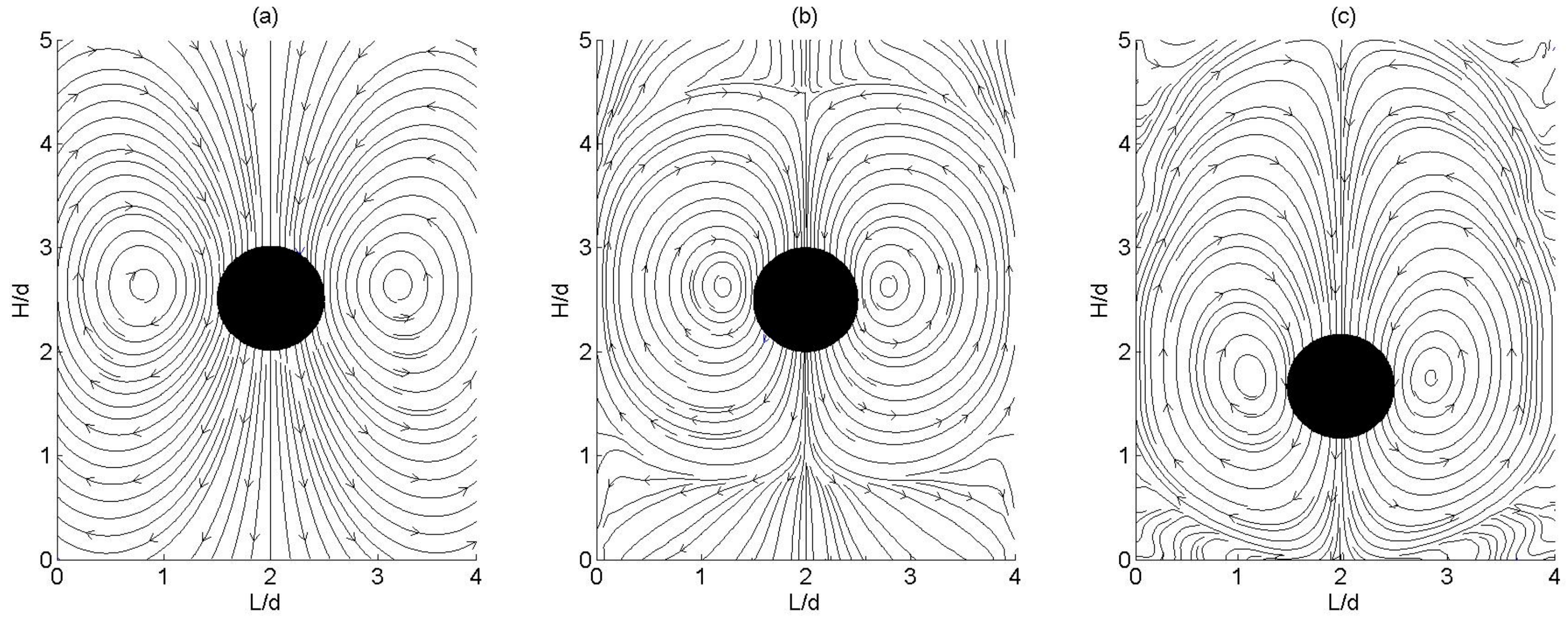

Figure 4.14: Streamlines for a sphere sedimentation in (a) Newtonian liquid ($Re = 0.001$); (b) Bingham liquid ($Re_s = 1, Bn_s = 0.21$) and (c) thixotropic liquid ($Re = 1, Db = 1, t_a = 643, \alpha = 99999$).

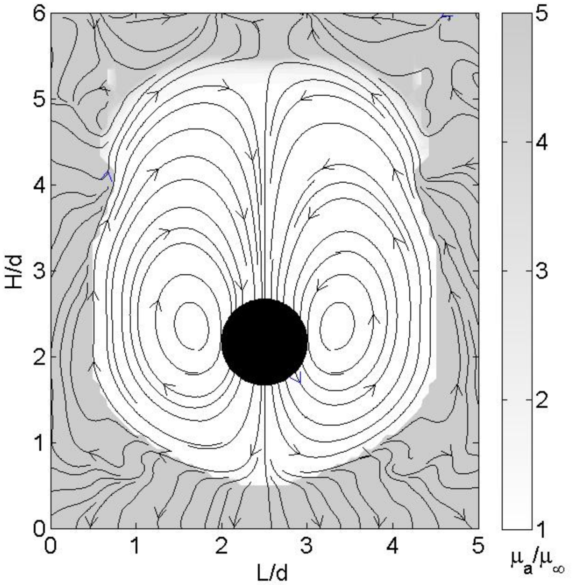

Figure 4.15: Viscosity contour plot coupled with streamlines for creeping flow of a sphere in thixotropic liquid

et al. [32] have also speculated that the negative wake observed in their experimental studies resulted from the elastic effects of their experimental liquids; aqueous suspension of Laponite clay and Carbopol, respectively. Since the viscosity model used in present study is purely viscous, it can be stated that the non-existence of negative wake in our simulations is expected and not in disagreement of experimental works.

Bibliography

[1] A. Miyamura, S. Iwasaki, T Ishii, Experimental wall correction factors of single solid spheres in triangular and square cylinders, and parallel plates, *Int. J. Multiphase Flow* 7 (1981) 41.

[2] Fang Hai-Ping, Chen Shi-Yi, Lattice Boltzmann method for three-dimensional moving particles in a Newtonian fluid, *Chin. Phys. Soc.* 13 (2004) 47.

[3] M. P. Volarovich, A. M. Gutkin, Theory of flow in a viscoplastic medium, *Colloid J.* 15 (1953) 153.

[4] V. T. Andres, Equilibrium and motion of a sphere in a viscoplastic fluid, *Dokl. Akad. Nauk USSR* 133 (1960) 777.

[5] L. Valentik, R. L. Whitmore, The terminal velocity of spheres in Bingham plastics, *Brit. J. Appl. Phys.* 16 (1965) 1197.

[6] R. W. Ansley, T. N. Smith, Motion of spherical particles in a Bingham plastic, *AICHE J.* 13 (1967) 1193.

[7] N. Yoshika, K. Adachi, H Ishimura, On creeping flow of a viscoplastic fluid past a sphere, *Kagaku Kogaku* 10 (1971) 1144.

[8] G. Duvaut, J. L. Lions, Inequalities in mechanics and physics, Springer (1976).

[9] A. N. Beris, J. A. Tsamopoulos, R. C. Armstrong, R. A. Brown, Creeping motion of a sphere through a Bingham plastic, *J. Fluid Mech.* 158 (1985) 219.

[10] M. P. Dy Plessis, R. W. Ansley, Setting the parameters in solids pipelining, *J. Pipeline Div.* ASCE 93 (1967) 1.

[11] S. Ito, T. Kajiachi, Drag force on a sphere moving in a plastic solid, *J. Chem. Engng Japan* 2 (1969) 19.

[12] D. D. Atapattu, R. P. Chhabra, P. H. T. Uhlherr, Wall effect for spheres falling at small Reynolds number in a viscoplastic medium, *J. Non-Newtonian Fluid Mech.* 38 (1990) 31.

[13] D. D. Atapattu, R. P. Chhabra, P. H. T. Uhlherr, Creeping sphere motion in Herschel-Bulkley fluids: flow field and drag, *J. Non-Newtonian Fluid Mech.* 59 (1995) 245.

[14] J. Blackery, E. Mitsoulis, Creeping motion of a sphere in tubes filled with a Bingham plastic material, *J. Non-Newtonian Fluid Mech.* 70 (1997) 59.

[15] B. T. Liu, S. J. Muller, M. M. Denn, Convergence of a regularization method for creeping flow of a Bingham material about a rigid sphere, *J. Non-Newtonian Fluid Mech.* 102 (2002) 179.

[16] Z. Yu, A. Wachs, A fictitious domain method for dynamic simulation of particle sedimentation in Bingham fluids, *J. Non-Newtonian Fluid Mech.* 145 (2007) 78.

[17] M. Iwaoka, T. Ishii, Experimental wall correction factors of single solid spheres in circular cylinders, *J. Chem. Engg. Japan* 12 (1979) 3.

[18] M. Hariharaputhiran, R. S. Subramanian, G. A. Campbell, R. P. Chhabra, The settling of spheres in a viscoplastic fluid, *J. Non-Newtonian Fluid Mech.* 79 (1998) 87.

[19] T. Ferroir, H. T. Huynh, X. Chateau, P. Coussot, Motion of a solid object through a pasty (thixotropic) fluid, *Physics of Fluids* 16 (2004) 3.

[20] N. P. Chafe, J. R. de Bruyn, Drag and relaxation in a bentonite clay suspension, *J. Non-Newtonian Fluid Mech.* 131 (2005) 44.

[21] B. Guselin, L. Talini, B. Herzhaft, Y. Peysson, C. Allain, Flow induced by a sphere settling in an aging yield-stress fluid, *Physics of Fluid* 18 (2006) 103101-1.

[22] H. Tabuteau, P. Coussot, J. R. de Bruyn, Drag force on a sphere in steady motion through a yield-stress fluid, *J. Rheol.* 51 (2007) 125.

[23] E. W. Billington, Some measurements of the time dependence of the viscosity of thixotropic fluids, *Proc. Phys. Soc.* 75 (1960) 40.

[24] D. C. H. Cheng, Yield stress: a time dependent property and how to measure it, *Rheol. Acta.* 25 (1985) 542.

[25] E. A. Toorman, Modelling the thixotropic behaviour of dense cohesive sediment suspensions, *Rheol. Acta.* 36 (1997) 56.

[26] Z. Yu, A. Wachs, Y. Peysson, Numerical simulation of particle sedimentation in shear-thinning fluids with a fictitious domain method, *J. Non-Newtonian Fluid Mech.* 136 (2006) 126.

[27] A. M. V. Putz, T. I. Burghelea, I. A. Frigaard, D. M. Martinez, Settling of an isolated spherical particle in a yield stress shear thinning fluid, *Physics of Fluids* 20 (2008) 033102-1.

[28] J. M. Kim, C. Kim, C. Chung, K. H. Ahn, S. J. Lee, Negative wake generation of FENE-CR fluids in uniform and Poiseuille flows past a cylinder, *Rheol. Acta.* 44 (2005) 600.

[29] X. Frank, H. Z. Li, Negative wake behind a sphere rising in viscoelastic fluids: A lattice Boltzmann investigation, *Phys. Rev. E.* 74 (2006) 056307-1.

[30] X. Frank, M. Kemiha, S. Poncin, H. Li, Origin of the negative wake behind a bubble rising in non-Newtonian fluids, *Chem. Engg. Sci.* 61 (2006) 4041.

[31] O. G. Harlen, The negative wake behind a sphere sedimenting through a viscoelastic fluid, *J. Non-Newtonian Fluid Mech.* 108 (2002) 411.

Chapter 5

Two sphere sedimentation

The applications involving suspensions of solid particles are abundant in industrial and natural processes. The rheology of such suspensions depends on the hydrodynamic interactions of solid particles which are subjected to a variety of forces. Moreover the analytical and experimental analysis of these suspensions is difficult due to the multiple interaction effects and boundary conditions. A reasonable approach generally adopted by researchers is to conduct a study of single particle motion and then taking the two particle hydrodynamic interactions into consideration. In the present chapter, we build up on the results of preceding chapter by considering the sedimentation of two particles in Newtonian and non-Newtonian liquids at low Reynolds number. As a standard of various particle shapes conceivable, identical spheres are chosen for numerical experiments discussed in this chapter. Going one step further, the influence of inertial effects at moderate Reynolds number on the motion of two spheres is also discussed.

5.1 Two sphere sedimentation in Newtonian liquid

5.1.1 Introduction

When two spheres fall one above the other, each sphere tends to move liquid down with itself which influences the motion of other sphere. This mutual interaction between the spheres depends upon the Reynolds number and the distance between the center of two spheres. In the earliest theoretical work related to low Reynolds number regime, Smoluchowski [1] used method of reflections to approximately determine the terminal velocity of two spheres falling in an unbounded liquid and calculated the drag force D on each sphere employing correction factor δ[1] due to the mutual interaction of spheres. The drag force defined by Smoluchowski [1] is given by

$$D = 3\pi\mu dU\delta \tag{5.1}$$

with μ, d, U being the liquid viscosity, sphere diameter and terminal velocity, respectively. The correction factor δ is given by notion

$$\delta = 1 - \frac{3}{4}\frac{d}{l} + (\frac{3}{4}\frac{d}{l})^2 \tag{5.2}$$

where l is the separation distance between the centers of spheres. The drawback with this solution is its validity only for two identical spheres falling with a center to center distance greater than three diameters.

The first exact solution of creeping flow of two spheres sedimenting with constant and equal velocities was provided by Stimson and Jeffrey [2]. They determined the Stokes' stream functions from the motion of the liquid and deduced the forces (using Equation 5.1) required to maintain the motion of spheres. They defined the correction factor δ as the ratio of the force required to maintain the motion of either sphere in the vicinity of other to the force required to maintain its motion with the same velocity if the other sphere were at a infinite distance. Recalling the Stokes' law (Equation 4.2), the force required to maintain the motion of a single sphere is directly proportional to its terminal velocity. Therefore δ can also be defined as the ratio of the terminal velocity of single sphere ($U_{1\infty}$) to terminal velocity of sphere doublet ($U_{2\infty}$). The value of δ is given by expression

---

[1] In literature, the correction factor is usually denoted by symbol λ. However in present work the use of λ is reserved for thixotropic network parameter, therefore symbol δ is used instead of that.

$$\delta = \frac{U_{1\infty}}{U_{2\infty}} = \frac{4}{3} sinh\alpha \sum_{n=1}^{\infty} \frac{n(n+1)}{(2n-1)(2n+3)}\{1 - \frac{4sinh^2(n+1/2)\alpha - (2n+1)^2 sinh^2\alpha}{2sinh(2n+1)\alpha + (2n+1)sinh2\alpha}\} \tag{5.3}$$

where the ratio of center to center distance to the diameter of either sphere is equal to $cosh\alpha$. Faxen [3] and later Happel and Brenner [4] investigated the case of two touching spheres and found out the value of $\delta = 0.645$ which compares well with the solution obtained using Equation 5.3. Kynch [5] extended the method of reflections to analytically solve the motion of two or more spheres. Mazur and Saarloos [6] developed a method based on Fourier-space multiple expansion to calculate the sphere mobility functions for four and more spheres. Their findings were in close agreement with those obtained by Kynch [5].

In addition to theoretical studies, there are numerical solutions available in literature for two or more body interactions. Ganatos et al. [7] extended the collocation technique, earlier used by researchers for bounded and unbounded multi-particle axisymmetric Stokes flow, to solve the non-axisymmetric creeping-motion flows. They handled a variety of problems and calculated the velocity and drag coefficient of two or more closely spaced spheres in a plane. Batchelor [8] performed a rigorous study of hydrodynamic interactions between small rigid spheres settling under gravity through Newtonian liquid and put forth the analytical expressions of pair distribution function and sedimentation coefficient for interacting spheres. Later Batchelor and Wen [9] provided the numerical solutions of these expressions for various conditions including different sizes and weights of spheres. Other notable numerical studies for hydrodynamic interaction of two or more spheres include Cichoki et al. [10], Ingber [11], Tran-Cong and Phan-Thien [12] and Durlofsky and Brady [13].

Turning the focus towards experimental studies, Happel and Pfeffer [14] measured the velocities of two identical spheres falling one above the other in a circular cylinder as a function of the center to center distance between them at low Reynolds number. They found a good agreement with the theoretical studies. They experimentally confirmed the theoretical result that two spheres attract each other at Reynolds number greater than 0.25. Kasper et al. [15] studied the settling of chains of spheres in circular cylinders and determined the drag, shape factors and wall correction factors. Muraoka and Kumagai [16] conducted the experiments of two sphere sedimentation and confirmed the results obtained by Steinberger and Pruppach [17] that each sphere falls at different velocity, which increases with time and the velocity of leading sphere depends upon the Reynolds number (even in low Reynolds number regime). They empirically found a close fit expression for drag incorporating correction for Reynolds number. Zheng et al. [18] measured the velocity of two identical falling spheres with the various ratios of diameter of sphere to diameter of cylinder. Their results compared well with Leichtberg et al. [19] and Stimson and Jeffery [2].

In the following study, we display the results of present work which deals with the sedimentation of two spheres in Newtonian liquid. The spheres fall along the axis of a cylinder of square cross-section in a direction parallel to their line of centers. Initially the Reynolds number is kept very low ($Re < 0.25$) and the terminal velocity of sphere doublet is measured. Further the dynamic behavior of two spheres is investigated at moderate Reynolds number.

5.1.2 Flow definition and dimensionless numbers

The flow definition for two identical spheres settling along the axis of a cylinder of square cross-section in a direction parallel to their line of centers is displayed in Figure 5.1. The spheres are placed at a vertical distance of W, measuring center to center and allowed to fall under the influence of gravity (g). The sphere diameter d and the terminal velocity in an unbounded medium U_∞ are taken as characteristic length and velocity, respectively. The flow is governed by the Reynolds number which is expressed by the notion

$$Re = \frac{\rho_l U_\infty d}{\mu} \tag{5.4}$$

where ρ_l and μ being the density and viscosity of the Newtonian liquid, respectively. The terminal velocity of sphere falling in an unbounded medium is defined differently

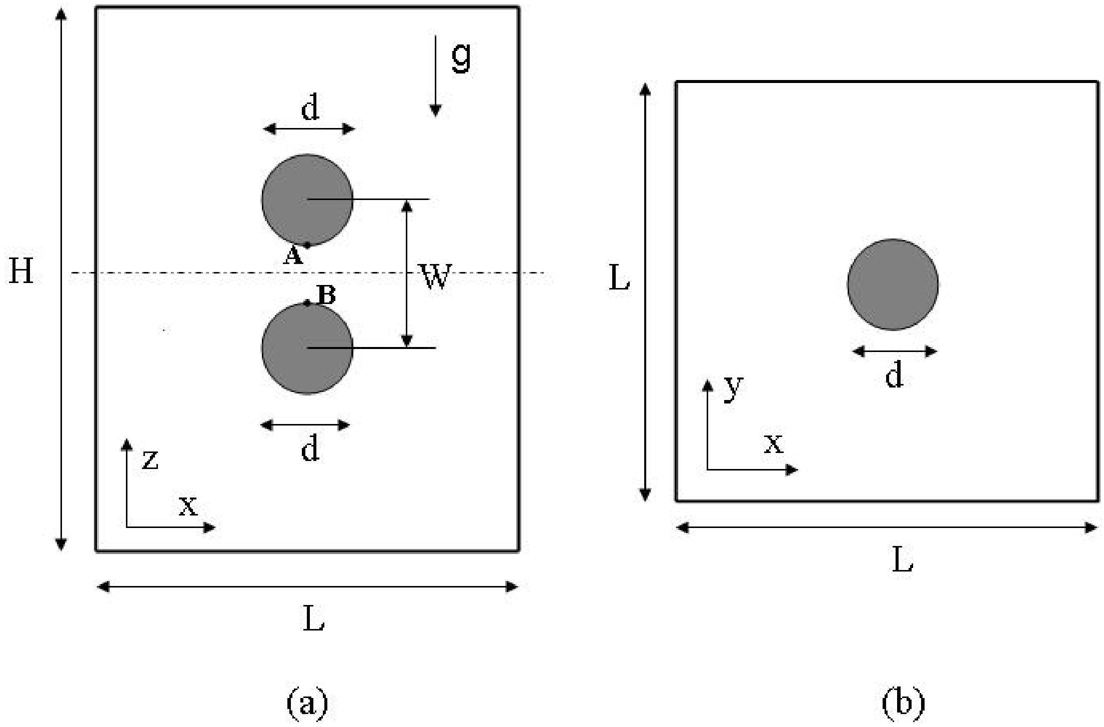

Figure 5.1: Flow definition of two sphere motion in a cylinder of square cross-section ($L \times L$); (a) Front view of cylinder (b) Top view of cylinder taken at cross-section marked by dashed line in (a).

for low and moderate Reynolds number cases. In case of low Reynolds number flow, the Stokes velocity (U_s) is considered as characteristic velocity which is read as

$$U_\infty = U_s = \frac{d^2(\rho_s - \rho_l)g}{18\mu} \tag{5.5}$$

with ρ_s being the density of sphere. To calculate U_∞ in case of moderate inertial influences, we consider the drag coefficient expression proposed by Abraham [20] and later used by Ten Cate et al. [21]:

$$C_d = \frac{24}{Re}(1 + \frac{\sqrt{Re}}{9.06})^2 \tag{5.6}$$

Based on drag coefficient defined by Equation 5.6, U_∞ is given by

$$U_\infty = \frac{d^2(\rho_s - \rho_l)g}{18\mu(1 + {}^{\sqrt{Re}}/_{9.06})^2} \tag{5.7}$$

Implementation of zero velocity boundary condition can be seen in appendix C.

5.1.3 Hydrodynamic interaction at low *Re*

Investigation of hydrodynamic interaction of two spheres falling one above the other is started with low Reynolds number flow. The density and viscosity of liquid are chosen as $\rho_l = 8.0$ and $\mu = 0.8$, respectively. The diameter and density of each falling sphere are defined as $d = 12$, $\rho_s = 4\rho_l$. The value of g is chosen in such a way that Reynolds number is very low ($Re = 0.001$) and grid size chosen for these simulations is $73 \times 73 \times 281$ ($x \times y \times z$). The numerical experiments are carried out by placing the two spheres at different center to center distances so that the hydrodynamic interaction could be examined at various W/d ratios ($W/d = 1.11, 1.43, 2.0, 2.5, 3.33$). Initially, the sphere doublet is placed along the axis of symmetry with trailing sphere's location reading $0.5x \times 0.5y \times 0.6z$.

Hydrodynamic interaction between two spheres is interpreted through several quantitative (e.g. drag force, terminal velocity) and qualitative parameters (e.g. flow field, attraction of spheres). In present work, the focus is set on the terminal velocity, flow field and attraction of spheres. The terminal velocity of single sphere falling under same conditions (as two spheres) is also calculated for a quantitative comparison with terminal velocity of sphere doublet. The velocity of falling sphere(s) with time is plotted in Figure 5.2 to demonstrate the steady state terminal velocity in case of single and double sphere sedimentation. It is obvious from the figure that as the sphere starts settling, its velocity first increases and then attains a constant value under the equilibrium of acting forces (gravity force=hydrodynamic force+buoyancy force). Related to two sphere sedimentation, a quick observation can be made that for any d/W ratio, both the spheres (leading and trailing) fall with the same velocity and their steady state velocities are also equal. This concludes that irrespective of center to center distance, two spheres do not attract each other at low Reynolds number. This is in agreement with the literary analysis of two sphere sedimentation problem.

Figure 5.3 displays the streamlines of single and double sphere sedimentation with

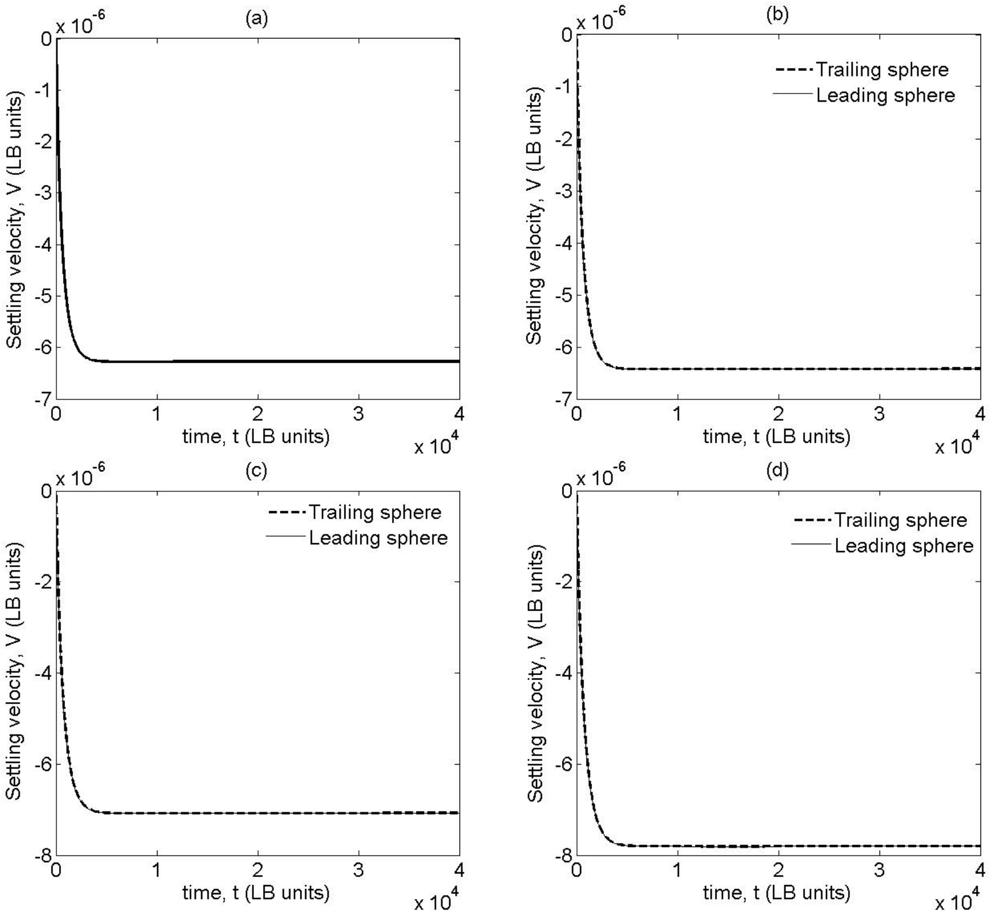

Figure 5.2: Time series of settling velocity of (a) single sphere and two spheres with different W/d ratios; (b) $W/d = 3.33$ (c) $W/d = 2.0$ (d) $W/d = 1.43$

different values of center to center distance. When the separation distance between two spheres is moderately high ($W/d = 3.33$), the hydrodynamic interaction between the two spheres is very minor. One can observe in Figure 5.3 (b) that both the spheres move with their own recirculating regions on either side. As the separation distance is decreased, the flow fields of two spheres start interacting with each other (Figure 5.3 (c)). Decreasing the distance further, the flow fields of two spheres merge with each other and now the sphere doublet move with only two recirculating regions on either side. Therefore it is clear that the hydrodynamic interaction between the spheres increases with decrease of center to center distance. The direct effect of this hydrodynamic interaction between the two spheres is obvious when we plot the terminal velocity of two spheres with W/d ratio (Figure 5.4).

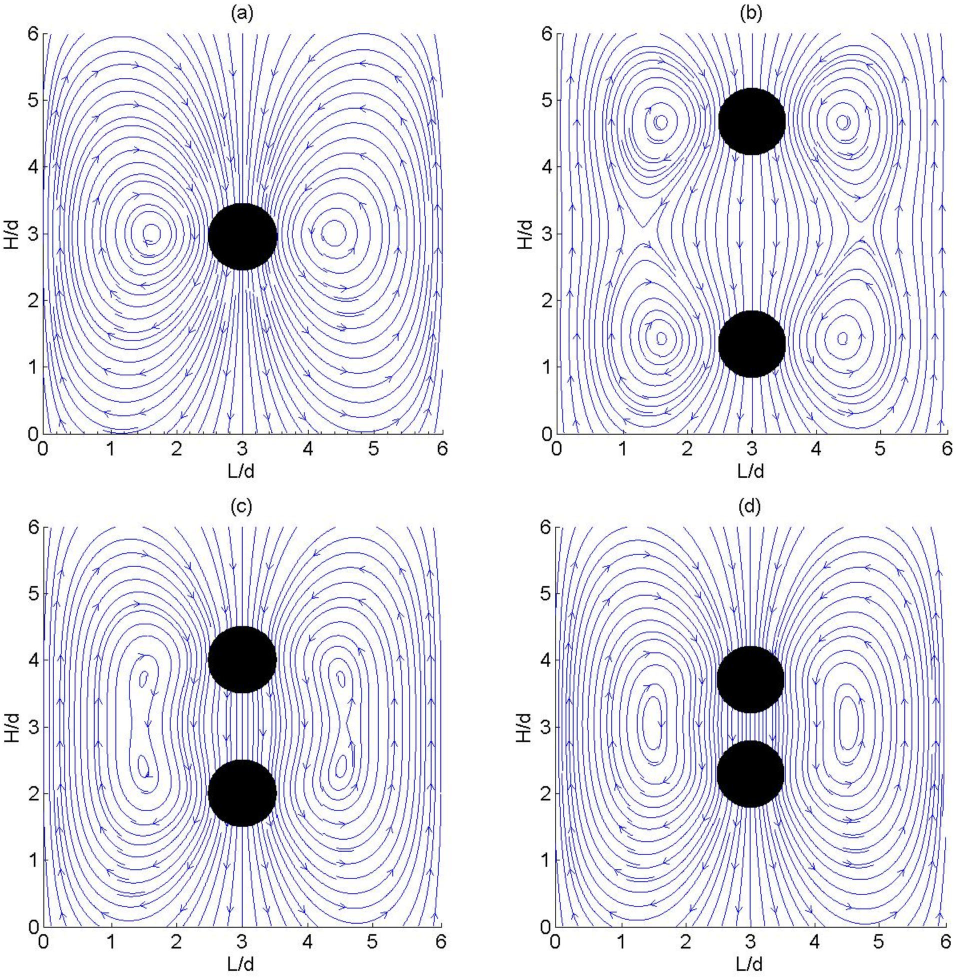

Figure 5.3: Streamline flow region for settling of (a) single sphere and two spheres with W/d ratios (b) 3.33 (c) 2.0 (d) 1.43 .

The terminal velocity of two spheres is always equal or higher than the terminal velocity of single sphere settling under same conditions. This phenomena is explained by adopting a point of view when two spheres move while touching each other. With this configuration, the leading sphere behave as a shield to trailing sphere which experiences a very smaller drag force as compared to leading sphere. Treating the two spheres like a single body, the mass of whole body is doubled however the drag force on the whole body is much less than twice the drag force experienced by single sphere. Therefore using the Equations 4.1 and 4.2, one obtains a higher terminal velocity of sphere doublet in comparison to that of single sphere settling in similar conditions. When the separation between the two spheres increases, the drag force experienced by trailing sphere increases

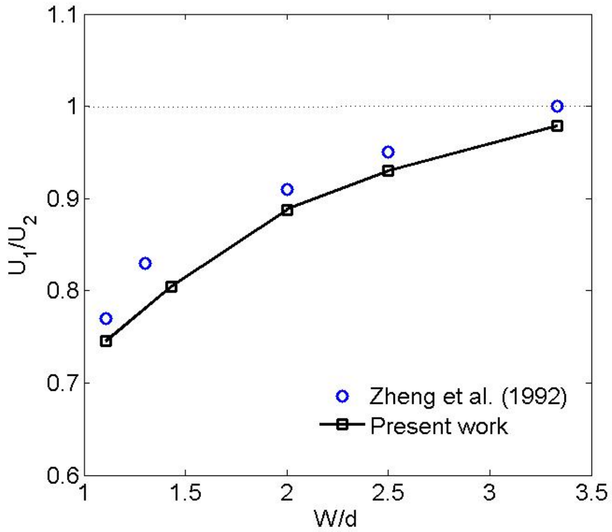

Figure 5.4: Velocity ratio U_1/U_2 as a function of W/d ratio; U_1 is the settling velocity of a single sphere in finite size medium; U_2 is the settling velocity of sphere doublet in finite size medium; Comparison with literature result (Zheng et al. [18])

but still less than the drag force experienced by a single sphere. When the two spheres move with a very large separation distance, they do not affect the motion of each other (no hydrodynamic interaction) and their individual motions are similar to that of single sphere.

We compare our results (see Figure 5.4) with data obtained by Zheng et al. [18] who used circular cylinder as container with ratio $d/b = 0.17$ where b was the diameter of cylinder (we use a square cylinder with $d/L = 0.17$). In order to understand the deviations between our results and those obtained by Zheng et al., we tabulate these data in Table 5.1 along with the theoretical solutions obtained by Stimson and Jeffrey [2] using Equation 5.3. Before going further, let us define parameters $U_1, U_2, U_{1\infty}$ and $U_{2\infty}$ first. U_1 and U_{1_∞} are the terminal velocities of a single sphere settling in a finite size medium and unbounded medium, respectively. Similarly U_2 and $U_{2\infty}$ are the terminal velocities of a sphere doublet settling in a finite size medium and unbounded medium, respectively. Considering all the studies mentioned in Table 5.1 separately, ratio of U_1/U_2 (or $U_{1\infty}/U_{2\infty}$) increases with separation distance (W/d ratio) which we have discussed already. Now choosing a certain separation distance, say $W/d \approx 1.1$, and comparing

Stimson and Jeffery [2] (unbounded medium)		Present results (square cylinder $d/L = 0.17$)		Zheng et al. [18] (circular cylinder $d/b = 0.17$)	
W/d	$U_{1\infty}/U_{2\infty}$	W/d	U_1/U_2	W/d	U_1/U_2
1.128	0.663	1.11	0.745	1.11	0.770
1.543	0.702	1.43	0.804	1.25	0.830
2.352	0.768	2.5	0.930	2.5	0.950
3.762	0.836	3.33	0.979	3.33	1.00

Table 5.1: Ratios of terminal velocity of single sphere to terminal velocity of sphere doublet (in similar conditions) presented by various studies.

the results of Stimson and Jeffrey [2] and Zheng et al. [18], it is observed that as the wall effects increase, ratio of terminal velocity of single sphere to that of two sphere (in similar conditions) also increases ($U_1/U_2 > U_{1\infty}/U_{2\infty}$). Similar observation is made for other W/d ratios. This indicates that retardation effect due to walls is much stronger for two spheres settling one above the other. The force balance equation for a single sphere settling in a finite size container is written as

$$F_G = F_D + F_B + F_W \tag{5.8}$$

where F_G, F_D, F_B, and F_W are gravitational force, drag force, buoyancy force and force due to wall effects on a single sphere, respectively. In case of two identical spheres (one above the other) sedimentation, force balance equation is

$$2F_G = F_D^{'} + 2F_B + F_W^{'} \tag{5.9}$$

with $F_D^{'}$ and $F_W^{'}$ being the drag force and force due to walls, respectively on sphere doublet. Combining the Equations 5.8 and 5.9 we obtain

$$F_W^{'} = 2F_W + 2F_D - F_D^{'} \tag{5.10}$$

If the two spheres are not very far from each other, the drag force on sphere doublet $F_D^{'}$ is less than the twice of drag force on single sphere, i.e. $2F_D - F_D^{'} > 0$. Replacing this condition in Equation 5.10 we find that

$$F_W^{'} > 2F_W \tag{5.11}$$

Therefore it is concluded that each sphere of a sphere doublet, settling in a finite size container, experiences a higher retardation effect in comparison to a single sphere sedimenting alone in same conditions. This implies that the value of U_1/U_2 increases with stronger wall effects. Since we use a square cylinder with $d/L = 0.17$, the wall effects should be slightly milder in our numerical experiments in comparison to the experiments conducted by Zheng et al. [18] with circular cylinder. This is well supported by the fact that our values of U_1/U_2 are approximately 3% (on average) lower than the experimental data.

5.1.4 Hydrodynamic interaction at moderate Re

To investigate the hydrodynamic interaction of two settling spheres at moderate Reynolds number, we keep the physical properties of liquid and identical spheres unchanged. The Reynolds number ($Re = 6.2$) for this study is based on the terminal velocity U_∞ given by Equation 5.7. The center to center distance between the spheres is defined by W/d ratio and the grid size used is $49 \times 49 \times 1000$ ($x \times y \times z$). The spheres are placed along the axis of the symmetry with trailing sphere being at location $0.5x \times 0.5y \times 0.7z$.

In this study, the focus is set on the hydrodynamic interaction between two spheres, initially placed at a separation distance of $2d$ ($W/d = 2.0$) , which are allowed to sediment under the influence of gravitational acceleration (g). The time series of settling velocity and distance of both the spheres are displayed in Figure 5.5. Contrary to the low Reynolds number study, there exists a attraction between spheres at moderate Reynolds number. Initially the trailing sphere moves with same velocity as that of leading sphere, however after a while it starts moving faster and ultimately collides with the leading sphere. Figure 5.5 (b) shows the position of bottom point of trailing sphere and top point of leading sphere (defined by point A and B, respectively in Figure 5.1) with time. Various studies available in literature (e.g. Happel and Pfeffer [14]) have reported that the trailing sphere approaches leading sphere when $Re > 0.25$. Therefore our

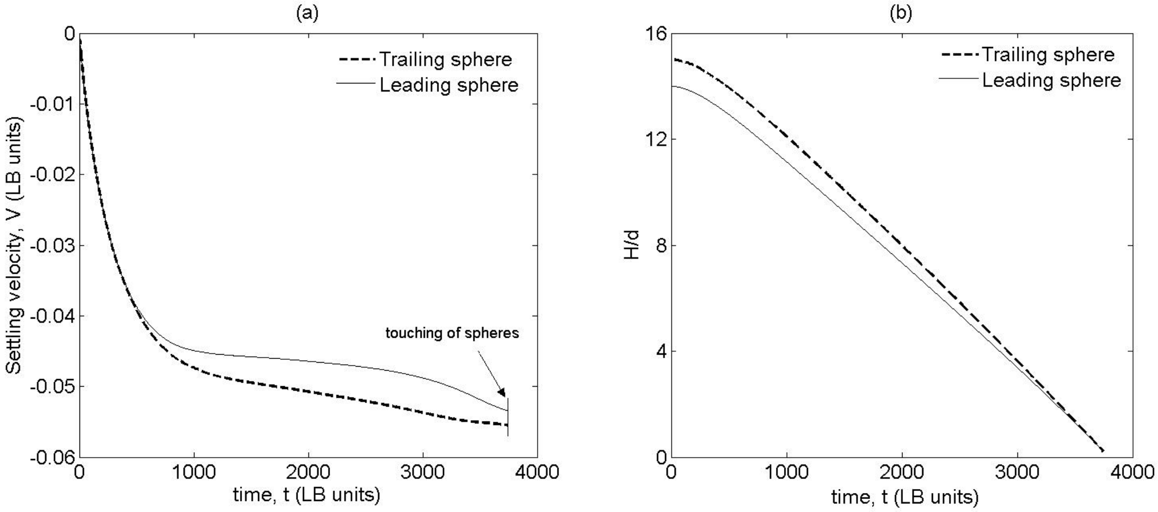

Figure 5.5: Trajectory of (a) velocity and (b) traveled distance of two settling spheres in Newtonian liquid with $d/W = 0.5$ at $Re = 6.2$.

observations are in agreement with literature.

The attraction of spheres at moderate Reynolds number is due to the interaction of the trailing sphere with the wake of the leading sphere. Figure 5.6 displays the velocity contour plots of a single sphere sedimenting in low and moderate Reynolds number flow. At moderate Reynolds number, the wake is stronger which results in a low pressure region behind the leading sphere. The trailing sphere is sucked into this low pressure region, that is why it accelerates faster than leading sphere.

The flow fields (in terms of velocity vectors) of two spheres sedimenting in a Newtonian liquid at moderate Re are displayed in Figure 5.7. Initially when the two spheres are at a distance of $2d$ (5.7 (a)), they move with their own flow fields interacting little with each other. Recirculating regions at either side of both the spheres are reminiscent to those observed in Figure 5.3 (c). At this moment ($t = 100$), both the spheres settle with equal velocity. Due to the low pressure region, the trailing sphere approaches towards the leading sphere resulting in the merger of their flow fields (Figure 5.7 (b) and (c)).

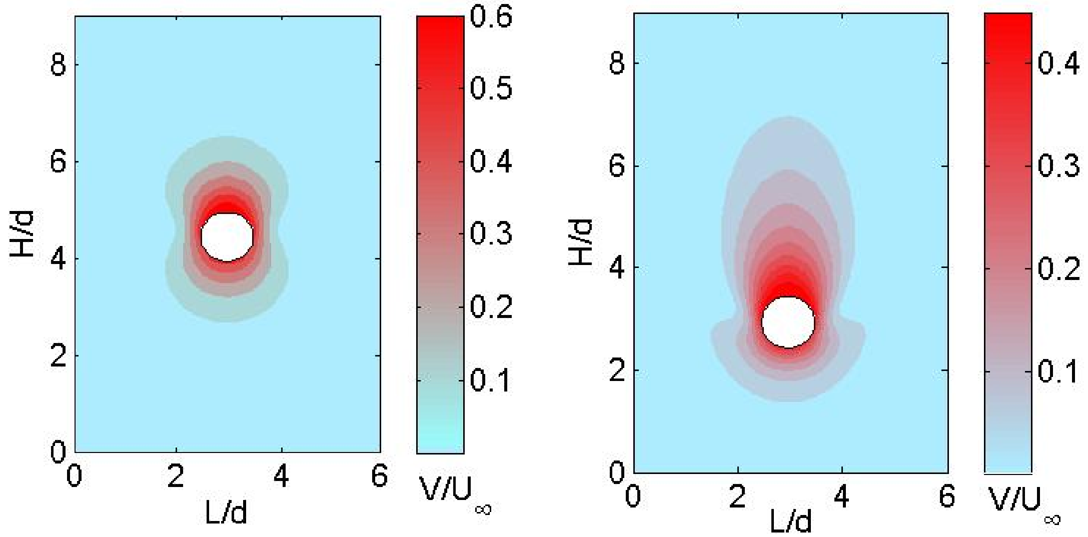

Figure 5.6: Velocity contour plot of a single sphere settling in Newtonian liquid; (a) $Re = 0.001$; (b) $Re = 6.2$.

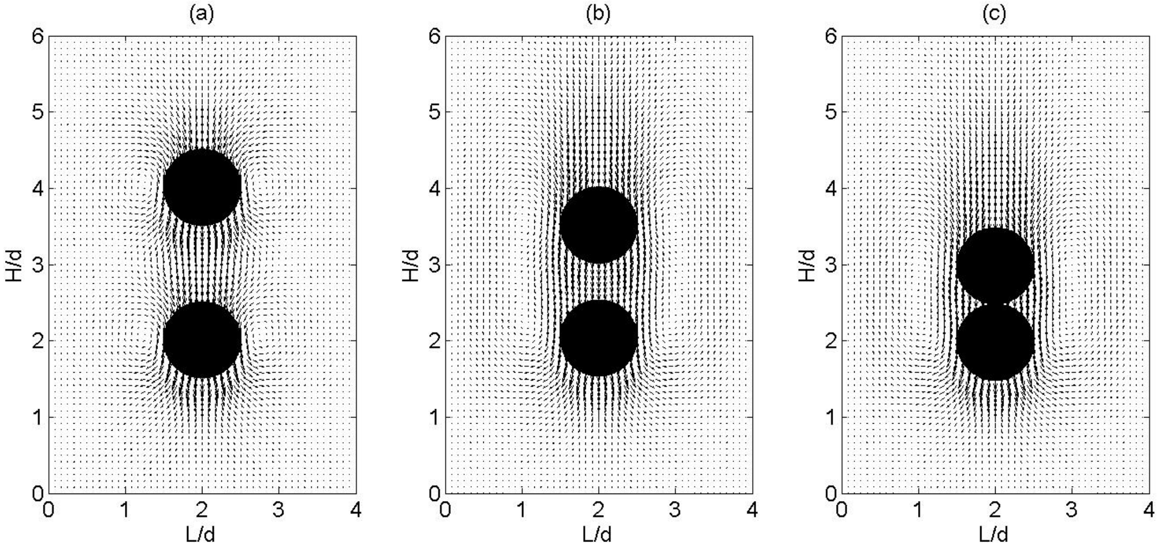

Figure 5.7: Velocity vectors of the two spheres settling in a Newtonian liquid at moderate Reynolds number; (a) $t = 100$ (b) $t = 2400$ (c) $t = 3800$.

5.2 Two sphere sedimentation in Bingham liquid

5.2.1 Introduction

The hydrodynamic interaction of two or more spheres in viscoplastic liquids plays a vital role in handling the various industrial processes involving gelled liquids like slurry. Therefore it is important to understand the basic mechanism of hydrodynamic interaction between spheres at low as well as high Reynolds number. Though there are numerous studies available in literature related to two sphere sedimentation in Newtonian liquids (refer subsection 5.1.1), one finds few results for viscoplastic liquids, probably due to the complexity associated with two sphere motion coupled with discontinuous nature of viscoplastic liquid models.

Liu et al. [22] numerically investigated the creeping flow of two identical spheres falling collinearly along the axis of a circular cylinder in Bingham liquid. They calculated the yield surfaces as a function of ratio of center to center distance to the radius of sphere and further predicted a plug like (unyielded) region between the two spheres along the symmetry axis. They also investigated the case of two approaching spheres falling in a line and predicted qualitatively different yield surfaces. In their experimental work, Merkak et al. [23] reported an appreciable hydrodynamic interaction between two spheres falling one above over other. They proposed the drag coefficient correlations and showed that yield effect of viscoplastic liquids reduces the degree of interaction compared to sedimentation in Newtonian liquid. Jie et al. [24] used finite element method coupled with regularization model to determine the yield surfaces and drag force on two or more spheres placed co-axially in a viscoplastic liquid. Yu and Wachs [25] examined the motion of two spheres translating along the axis of tube at low Reynolds number and predicted the faster velocity of two spheres than a single sphere due to the hydrodynamic interaction.

In the studies related to bubbles and drops, Potapov et al. [26] investigated the motion of multiple deformable Newtonian drops in a tube filled with Bingham liquid. They concentrated on the shape and extent of yielded region along with velocities and deformation of the drops and predicted a substantial increased yielded region and accelerated motion due to the hydrodynamic interaction of drops. In their numerical work, Singh and Denn [27] demonstrated that the yield effect of Bingham liquid is softened due to the hydrodynamic interaction of multiple drops which is similar to the results reported by Yu and Wachs [25]. In the following study, we investigate the hydrodynamic interaction between the two spheres falling along the axis of symmetry at low and moderate Reynolds number. Hydrodynamic interaction is interpreted in terms of settling velocity, flow field and attraction between the spheres.

5.2.2 Flow definition and dimensionless numbers

Flow definition for two sphere sedimentation study with Bingham liquid remains same as with Newtonian liquid (see Figure 5.1). The flow is governed by two dimensionless numbers namely Reynolds number and Bingham number which are based on the terminal velocity (U_∞) in an infinite medium. The definition of Reynolds number is given by Equation 5.4 while the Bingham number is expressed by the notion

$$Bn = \frac{\tau_0 d}{\mu_p U_\infty} \tag{5.12}$$

where τ_0 and μ_p are the yield stress and plastic viscosity of the Bingham liquid, respectively. For low and moderate Reynolds number, U_∞ is defined by Equations 5.5 and 5.7 (with $\mu = \mu_p$), respectively. Zero velocity boundary conditions are applied on cylinder walls. A detailed explanation can be seen in appendix C.

5.2.3 Hydrodynamic interaction at low Re

This subsection deals with the sedimentation of two spheres translating along the axis of square cylinder filled with Bingham liquid. The inertial effects are considered low i.e. $Re = 1$. We use the identical spheres with physical properties similar to those used with Newtonian liquid study. Bingham liquid is defined by the properties; density $\rho_l = 8.0$, plastic viscosity $\mu_p = 0.8$ and viscosity ratio $\mu_r = 10^5$. The yield stress (τ_0) of liquid is related to the Bingham number which has a (arbitrarily chosen) fixed value

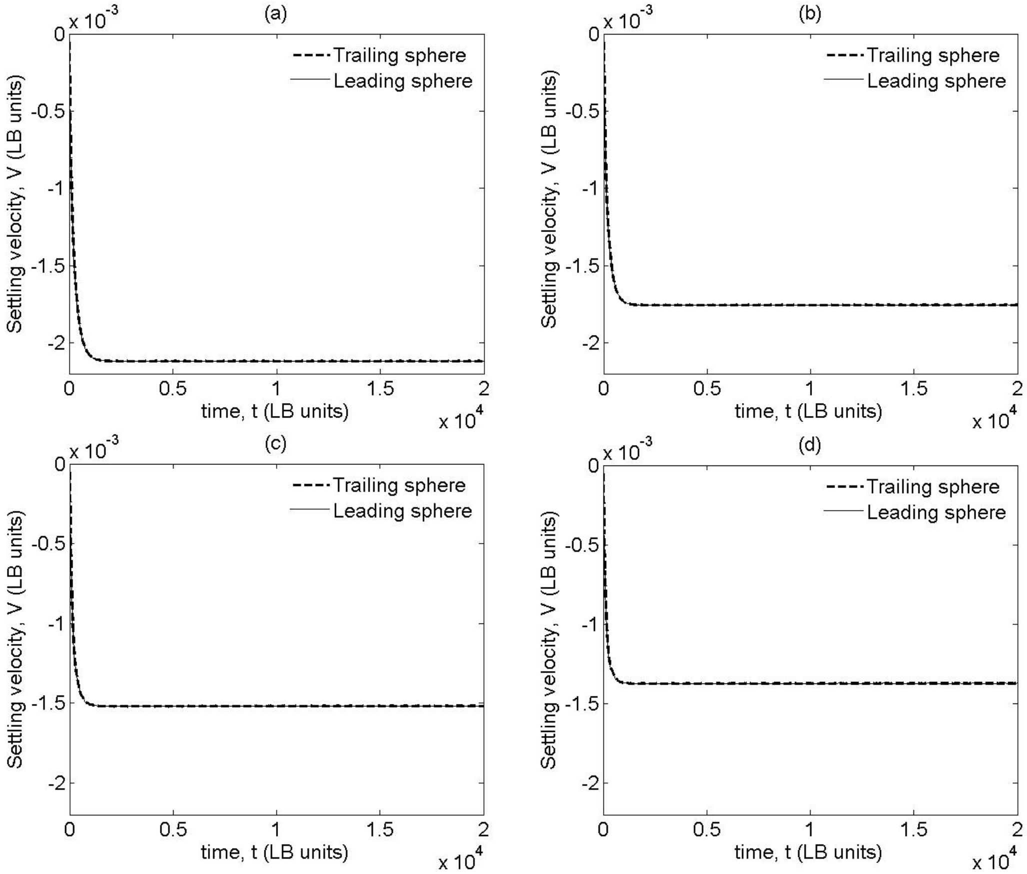

Figure 5.8: Time series of settling velocity of the two spheres settling in a Bingham liquid with different W/d ratios; (a) $W/d = 1.5$ (b) $W/d = 2.0$ (c) $W/d = 2.5$ (d) $W/d = 3.0$

($Bn = 0.36$) and the grid size chosen for simulations is $49 \times 49 \times 199$ ($x \times y \times z$). Initially the spheres are placed along the axis of symmetry with trailing sphere's location reading $0.5x \times 0.5y \times 0.6z$.

To examine the hydrodynamic interaction, the numerical experiments are performed with a range of center to center distance ($W/d = 1.0, 1.25, 1.5, 2.0, 2.5, 3.0, 3.5$) between the two spheres. The settling velocity of falling spheres is plotted against time in Figure 5.8 for some W/d ratios to demonstrate the steady state condition. It is obvious from the figure that both the spheres initially accelerate with equal rate and ultimately move with equal terminal velocity. Therefore it is concluded that both the spheres maintain the initial distance throughout their motion and the trailing sphere does not approach the leading sphere. Though the spheres do not attract, their flow fields interact with each other and the interaction depends upon the separation distance. Figure 5.8 also

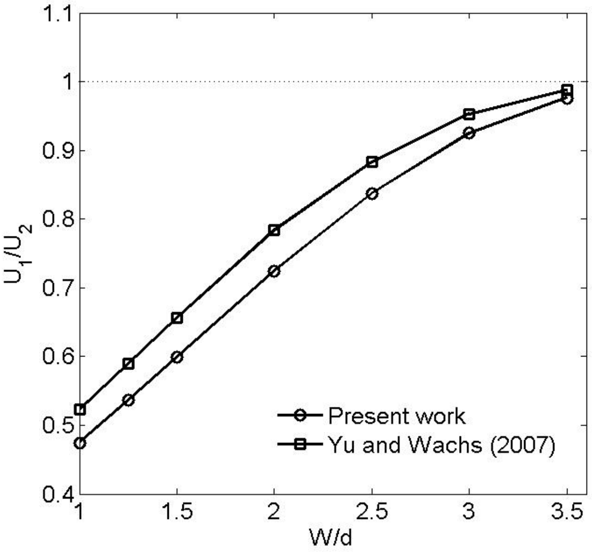

Figure 5.9: Velocity ratio as a function of W/d ratio; U_1 is the settling velocity of a single sphere; U_2 is the settling velocity of sphere doublet; Comparison with literature result (Yu and Wachs [25])

reveals that the terminal velocity of spheres becomes higher as their separation distance decreases. A quantitative depiction of hydrodynamic interaction (in terms of terminal velocity of two spheres) with W/d ratio is shown in Figure 5.9 where U_1 and U_2 are the terminal velocities of single sphere and two spheres, respectively settling in a finite size container filled with Bingham liquid under same conditions. When the two sphere are at a large distance ($W/d > 3.5$) , they hardly interact with each other and the terminal velocity of either sphere is equal to the terminal velocity of single sphere settling in same conditions. Our results show the same pattern as observed by Yu and Wachs [25]. The deviations appearing in the figure are due to the difference in geometry. Yu and Wachs [25] used a cylinder with circular cross-section whose diameter is four times the diameter of sphere while we have used a cylinder with square cross-section whose one side is four time the diameter of sphere. Due to this geometry difference, we observe less pronounced wall effects. As discussed in subsection 5.1.3, the value of U_1/U_2 is greater with stronger wall effects (circular cylinder). The average deviation observed in this study (7%) is relatively higher than that observed with Newtonian liquid.

In Figure 5.10 we display the steady state velocity vectors coupled with yielded and unyielded regions for various W/d ratios. When the two spheres are at distances of $2.5d$ (Figure 5.10 (c)) and $3d$ (Figure 5.10 (d)), the flow field and yielded envelope around a sphere is quite similar to those observed with single sphere (Figure 4.8). Apart from the islands of unyielded regions appearing on either side of a sphere, there are other unyielded regions noted in the yielded envelop. They include the regions along the mid plane; along the axis of symmetry between the spheres and on the poles of the spheres. The unyielded regions along the mid plane and symmetry axis are caused due to the re-circulation which is essential for mass conservation with in the yielded envelope. The re-circulation zones, being generated due to motion of two spheres have been shown in Figure 5.3 (b). We do not observe the polar caps on both side of spheres which are expected because of the stagnation points. Liu et al. [22] and Yu and Wachs [25] also reported the disappearance of polar caps in their numerical results. The reason, as pointed out by Liu et al. [22], may be that the polar caps region are too small to be detected in the simulations with present grid size. Use of a finer grid size may shed some insight into the problem. The size of unyielded regions along the planes decreases with the decrease of separation distance. The unyielded regions situated between the spheres along the axis of symmetry also decreases in size with decreasing separation distance. However, it becomes larger after bringing the spheres closer after a certain limit (e.g Figure 5.10 (a)). The small islands of unyielded regions at either side of spheres vanish with decreasing separation distance. The terminal velocity of spheres with less separation distance is higher (see Figure 5.9), they are confined by a larger unyielded region. In other way, the yielded envelope around the spheres reduces in size with decreases of separation distance. The flow field and yielded/unyielded regions reported in present work are in good agreement with the results obtained by Liu et al. [22] and Yu and Wachs [25].

5.2.4 Hydrodynamic interaction at moderate Re

The physical properties of liquid and solid spheres remain unchanged for study with moderate inertial influences. The characteristic velocity (U_∞) is determined using Equation

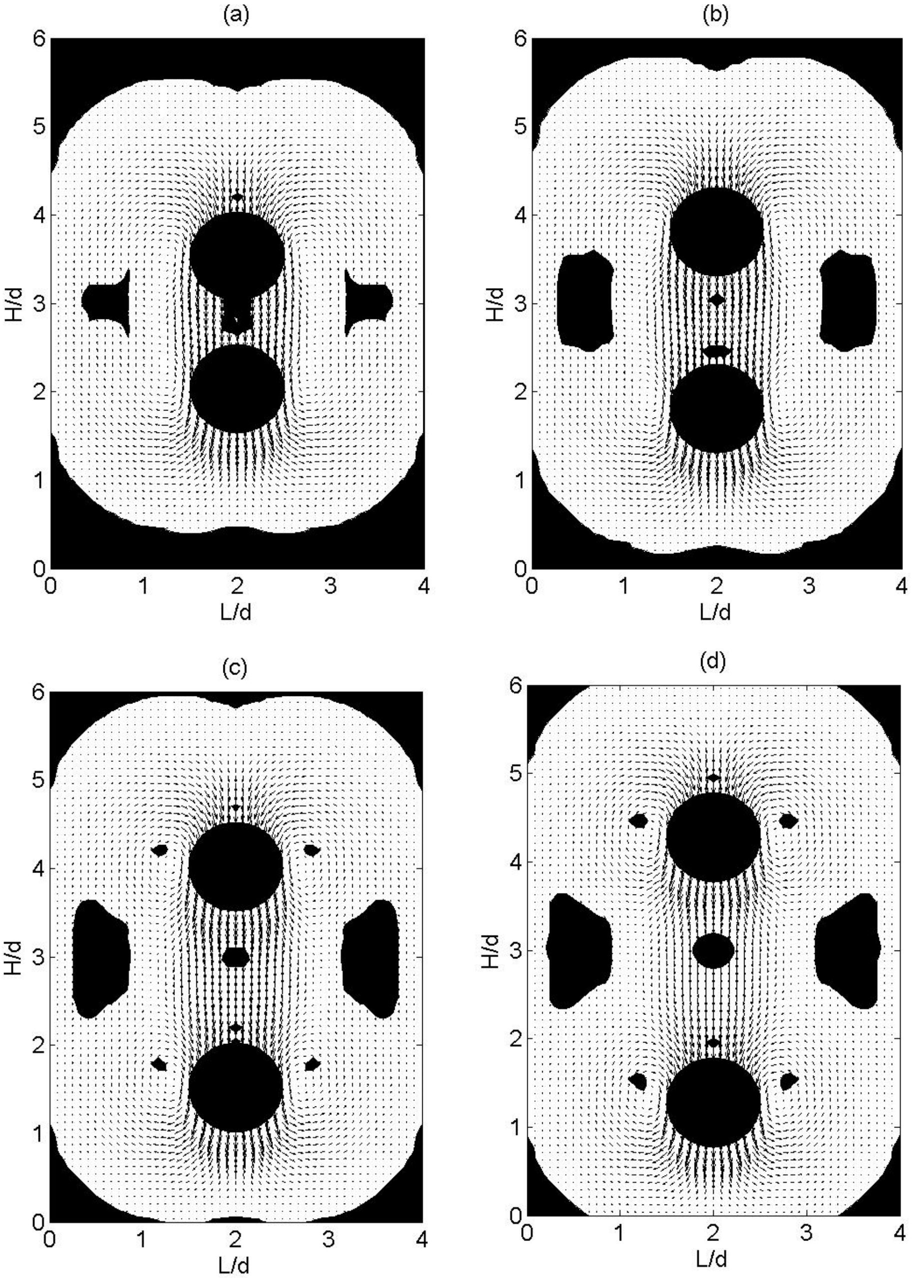

Figure 5.10: Steady state velocity vectors coupled with yielded (white)/unyielded (black) regions for settling of the two spheres in a Bingham liquid with different W/d ratios at $Bn = 0.36$ and low Reynolds number; (a) $W/d = 1.5$ (b) $W/d = 2.0$ (c) $W/d = 2.5$ (d) $W/d = 3.0$

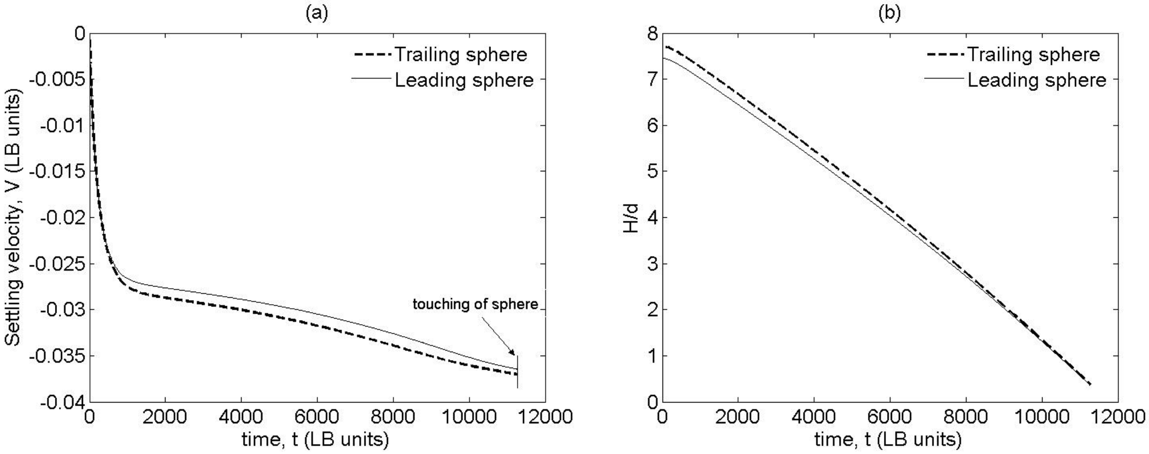

Figure 5.11: Time series of (a) settling velocity and (b) traveled distance of the two spheres settling in a Bingham liquid with $W/d = 2.0$.

5.7 (μ being equivalent to μ_p) and the Reynolds number for this case is 6.2. The Bingham number is 0.36 and the grid size used is $49 \times 49 \times 1000$ ($x \times y \times z$). The two spheres, placed initially at a center to center distance of $2d$ along the axis of symmetry fall in Bingham liquid under the influence of gravity. The starting position of the trailing sphere is kept as $0.5x \times 0.5y \times 0.7z$. The trajectories of settling velocity of spheres and distance covered by them are displayed in Figure 5.11. It is obvious from the figure that trailing sphere moves faster than the leading sphere at moderate Reynolds number. However the trailing sphere takes significantly greater time to touch the leading sphere in comparison to Newtonian liquid study ($Bn = 0$). The reason of this is attributed to the yield forces which retard the motion caused by the inertial forces. Therefore the attraction rate of spheres, falling along the axis, decreases with the increase of yield stress of Bingham liquid.

The velocity vectors coupled with yielded/unyielded regions are drawn at three different times ($t = 100, 5900, 11250$) and shown in Figure 5.12. Initially ($t = 100$) the spheres move with identical velocity and as the time progresses ($t = 5900, 11250$), the velocity of trailing sphere increases gradually and it approaches the leading sphere. During the initial stages (e.g $t = 100$) when flow is partially developed and spheres are far from each other, the unyielded regions appear along the mid plane, along the axis of symmetry between the spheres and at either side of each sphere. As the flow develops, the yield

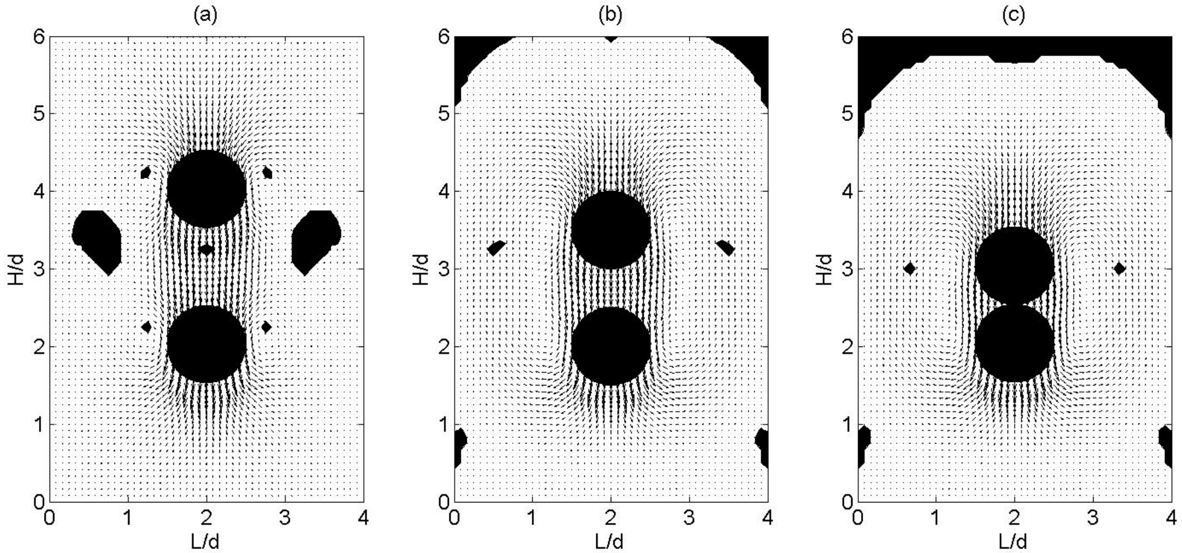

Figure 5.12: Velocity vectors coupled with yielded (white)/unyielded (black) regions for settling of the two spheres in a Bingham liquid at moderate Reynolds number.

effects are softened due to the inertial forces and the unyielded regions along the axis of symmetry and either side of sphere vanish. At this moment this system behaves like two sphere sedimentation in Newtonian liquid where the low pressure region in the vicinity of leading sphere's wake draws the trailing sphere towards itself. In case of low Reynolds number study with Bingham liquid (Figure 5.10), there exists an unyielded region along the axis of symmetry between the spheres which prevents the trailing sphere to approach leading sphere.

5.3 Two sphere sedimentation in thixotropic liquid

5.3.1 Introduction

An understanding of particle interaction in thixotropic liquid is necessary since it is involved in many industrial processes such as oils sands processing and drilling liquids, an important parameter in successful completion of oil and gas wells. It has been observed in some polymeric liquid studies that two identical spheres settling one above the other, form an aggregate due to the shear-thinning property of the liquid in which first sphere leaves a corridor of reduced viscosity behind itself (Riddle et al. [28], Liu and Joseph

[29], Joseph et al. [30]). There are few studies available in literature which probe the multi-particle sedimentation in thixotropic liquid exhibiting memory/time dependency, yield and shear-thinning together. In a experimental study of two or more particle sedimentation in a shear-thinning liquid (Carbolpol), Gheissary et al. [31] reported that the interaction between two particles not only depends upon the bulk rheology of liquid but also considerably influenced by the time of observation. They predicted the time effects due to the non-homogeneity of liquid structure.

Yu et al. [32] coupled Carreau model with thixotropic model (to include memory effect) to numerically investigate the multi-particle sedimentation in a shear-thinning liquid at low Reynolds number and they found memory of shear-thinning liquid accountable for the aggregation of settling spheres. Gueslin et al. [33] investigated the qualitative behavior of two identical spheres of two different materials settling along their line of center in a Laponite suspension which predominantly exhibits yield stress, shear-thinning and memory effect. They reported that two spheres of same material aggregate with their initial separation distance less than 15 radii and the phenomenon of negative wake is predicted to be dependent on particle Reynolds number. They also observed a side-by-side movement of the settling spheres in presence of negative wake. In the present work, we study the sedimentation of two spheres in a thixotropic liquid which exhibits memory, yield stress and shear thinning properties.

5.3.2 Flow definition and dimensionless numbers

The system of two spheres sedimenting along the axis of a square cylinder has been shown in Figure 5.1. In this study the cylinder is filled with a thixotropic liquid whose viscosity model has been defined by Equation 2.27. The flow is governed by a number of thixotropic parameters ($k_1, k_2, \mu_\infty, \alpha$ and λ) which are combined together to express dimensionless numbers such as Reynolds number, Deborah number, (pseudo) Bingham number and viscosity ratio. The Reynolds number (Re) is defined by Equation 5.4 with viscosity μ being equal to infinite shear viscosity μ_∞. Purely viscous Deborah number (Db), pseudo Bingham number and viscosity ratio are defined by notions

$$Db = \frac{U_\infty}{dk_2} \tag{5.13}$$

$$(pseudo)\ Bn = \alpha \frac{k_2 d}{k_1 U_\infty} \tag{5.14}$$

$$\alpha = \frac{\mu_0}{\mu_\infty} - 1 \tag{5.15}$$

with U_∞ being the terminal velocity of a sphere in infinite medium (calculated with $\mu = \mu_\infty$), μ_0 and μ_∞ being the zero and infinite shear viscosity, respectively. Zero velocity boundary conditions imposed on the cylinder walls can be seen in appendix C.

5.3.3 Hydrodynamic interaction in thixotropic liquid

The studies available in literature (Yu et al. [32], Gueslin et al. [33]) concerning the hydrodynamic interaction between two spheres sedimenting in time dependent shear-thinning liquid or yield stress-shear thinning liquid suggest that two spheres aggregate irrespective of the inertial forces exerted by them. Once the trailing sphere enters the corridor of reduced viscosity created by the motion of leading sphere, it starts moving faster and eventually collides with the leading sphere. To compare our results with experimental study done by Gueslin et al. [33] (who dealt with two systems of different Reynolds number of same order with one being slightly higher than other), we investigate the two systems whose Reynolds numbers are 0.83 and 2.25, respectively. The value of thixotropic parameter k_2, also the inverse of characteristic build up time scale, is chosen as 6.944×10^{-7}. The Deborah numbers for these systems turn out to be 825 and 2210, respectively. By choosing such a low value of k_2 (i.e. a high build up time scale), it is made sure that the trailing sphere reaches the region of low viscosity with in a adequate time period before this region becomes highly viscous due to the aging of the liquid. Speculatively we write that

$$\frac{W}{V_{tr}} < \frac{1}{k_2} \tag{5.16}$$

where W is the initial separation distance between the spheres and V_{tr} is the average settling velocity of trailing sphere. The initial value of network integrity parameter is arbitrarily set to $\lambda = 0.25$. The value of breakdown parameter k_1 is 400 which results in pseudo Bingham numbers 0.25 and 0.08 for $Re = 0.83$ and $Re = 2.25$ systems, respectively. The viscosity ratio is $\alpha = 99999$ while the grid size used for these simulations is $97 \times 97 \times 1000$ $(x \times y \times z)$. Initially, the sphere doublet is placed along the axis of symmetry with separation distance being $2d$ and location of the trailing sphere reads $0.5x \times 0.5y \times 0.7z$.

Figure 5.13 displays the time series of various quantities (settling velocity, separation distance and distance travelled) related to two systems ($Re = 0.83$ and $Re = 2.25$). The qualitative behavior of mentioned quantities is same for both the systems except the fact that drafting and kissing mechanism happen faster in case of higher Reynolds number system. In both the systems, initially spheres move with equal velocity, thereby maintaining a constant separation between them. After a certain time period (depending upon Reynolds number) the velocity of the leading sphere becomes higher than that of the trailing sphere. This is in contrast to the behavior observed with Newtonian liquid as well as Bingham liquid where the velocity of the leading sphere is either equal (initially) or less than that of the trailing sphere (refer Figures 5.5 (a) and 5.11 (a)). Due to this unexpected phenomenon, the separation distance between the spheres also increases and it becomes substantially higher than initial separation distance of $2d$ (Figures 5.13 (b) and (e)).

To explain this phenomenon, first of all we divide the total time period of numerical experiments in two parts; $t \leq t^{'}$ and $t > t^{'}$ where $t^{'}$ is the time when the bottom most point of the trailing sphere (point A in Figure 5.1 (a)) reaches the very initial position of upper most point of the leading sphere (point B in Figure 5.1 (a)). The time t' is shown in Figures 5.13 (c) and (f) too. Since the qualitative behaviors of both the systems are same, the focus is set on the system with $Re = 2.25$ only ($t^{'} = 31000$). Initially, when the flow is partially developed, both the spheres move with equal velocity. Since the thixotropic liquid considered in this study possesses the yield effects, we expect an

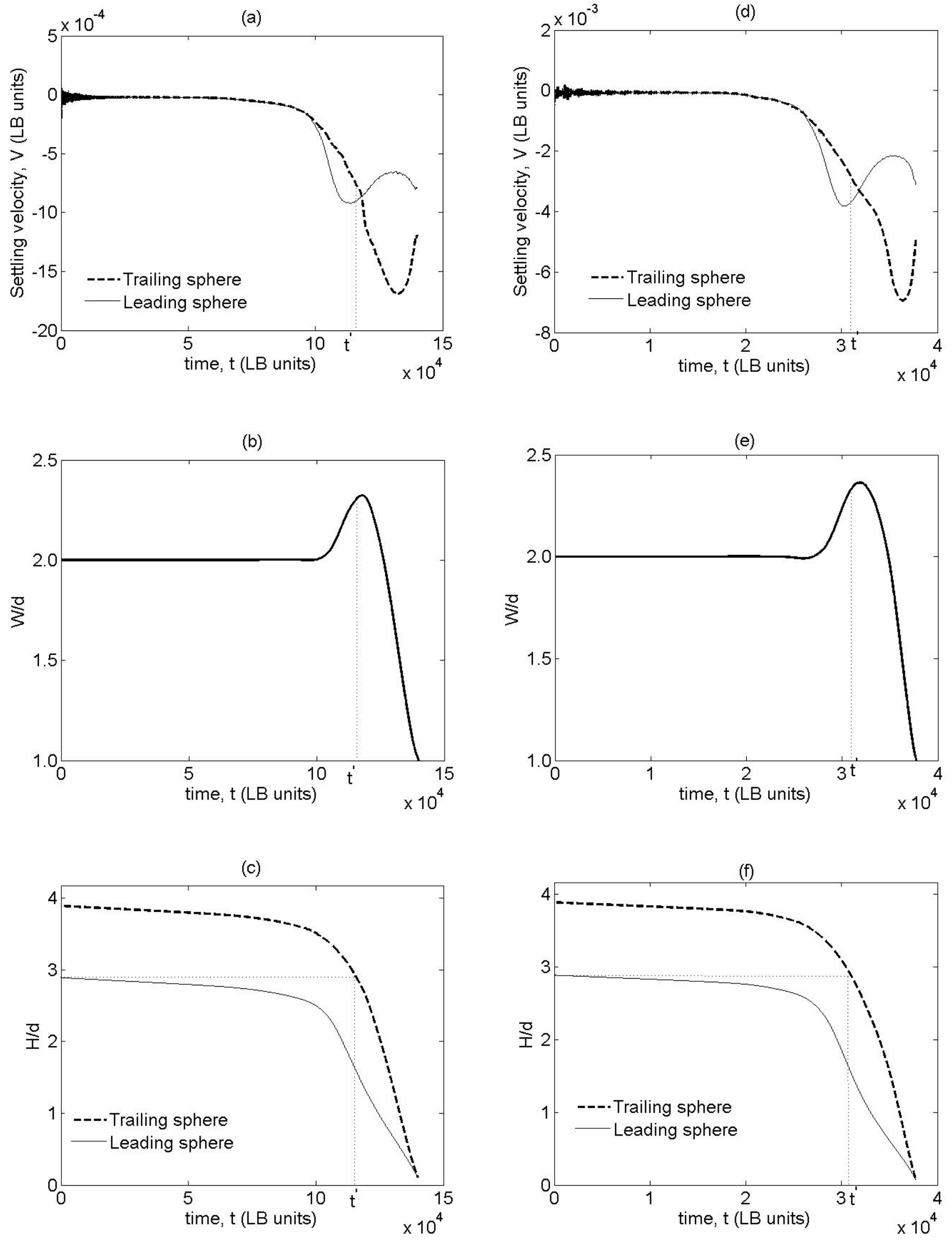

Figure 5.13: Time series of settling velocity (top panel), separation distance (middle panel) and traveled distance (bottom panel) for settling of the two spheres in a thixotropic liquid at $Re = 0.83$ (left) and 2.25 (right).

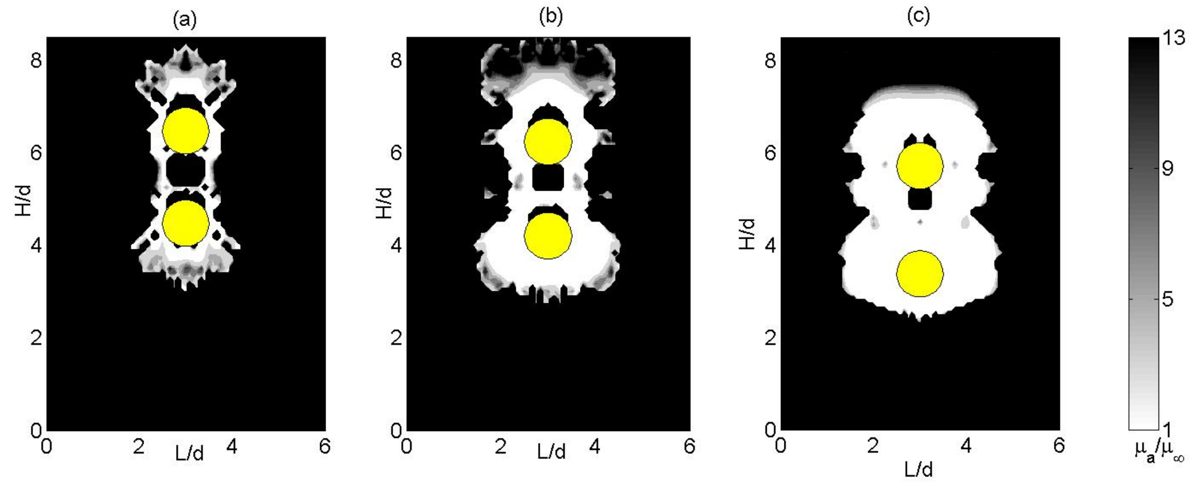

Figure 5.14: Viscosity contour plots for settling of the two spheres in a thixotropic liquid at time periods (a) $t = 25000$, (b) $t = 28000$ and (c) $t = 31000$.; $Re = 2.25$

unyielded region along the axis of symmetry between the spheres due to re-circulation as observed in case of Bingham liquid. It is important to point out here that in true manner this unyielded region is a highly viscous region. Apart from this as the time increases, the viscosity of the liquid region between the spheres increases due to aging. These two effects combine together and make the liquid region in front of the trailing sphere highly viscous.

On the other hand, the liquid region in front of the leading sphere is affected by aging only. Due to this difference in viscosity, the settling velocities of two spheres differ and the leading sphere moves faster than the trailing sphere. The contour plot of viscosity at different time periods ($t = 25000, 28000, 31000$) are shown in Figure 5.14. It is obvious from the figure that there exists a region of high viscosity ($\mu_a > 13\mu_\infty$) along the axis of symmetry between the spheres. The size of this region decreases with time because the trailing sphere approaches the region of low viscosity created by the motion of leading sphere. The shear thinning property of the liquid starts negating the combined effect of liquid aging and yield effects. However the region in front of the trailing sphere is still highly viscous as compared to the region confronted by leading sphere. Therefore the leading sphere moves faster and the separation distance increases.

As the trailing sphere reaches the initial position of leading sphere ($t = t'$), the

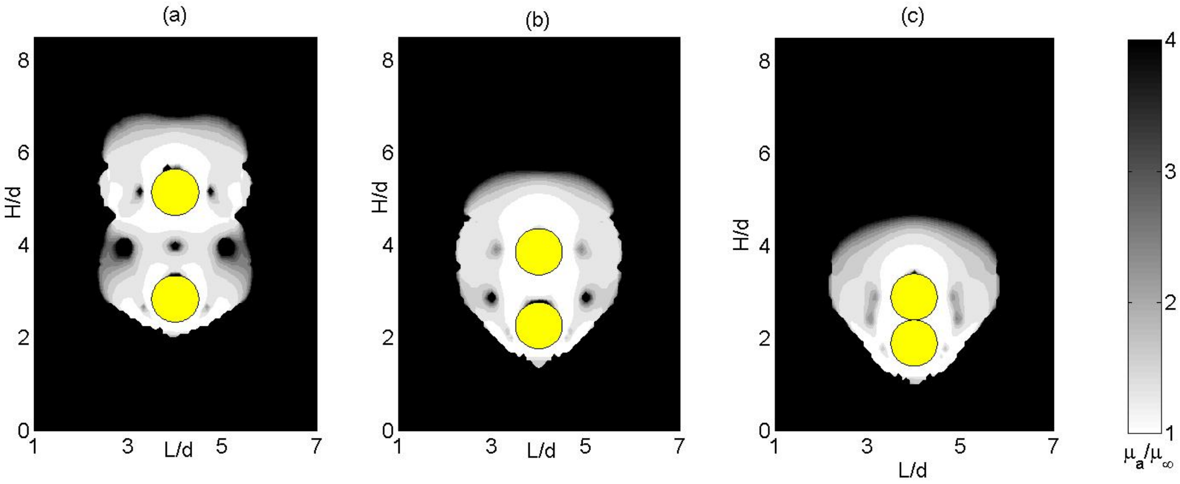

Figure 5.15: Viscosity contour plots for settling of the two spheres in a thixotropic liquid at time periods (a) $t = 33000$, (b) $t = 36000$ and (c) $t = 37800$.; $Re = 2.25$

shear thinning properties of liquid become more pronounced. There starts a competition between the yield+aging (tend to make system more viscous) and shear-thinning properties (tend to make system less viscous) and soon their effects counterbalance each other. At this juncture the velocity of both the spheres become equal and separation distance remains constant (momentarily). Further this point, the yield+aging effects are dominated by shear-thinning effects and the trailing sphere accelerates in low viscosity region. On the other hand, the upstream liquid region of leading sphere is comparatively more viscous now. Figure 5.15 displays the contour plots of viscosity at various time steps ($t = 33000, 36000, 37800$). The range of viscosity displayed in this figure is narrowed down to demonstrate the minor variations in viscosity of different regions around the spheres. The flow fields in terms of velocity vectors are shown in Figure 5.16 and their behavior qualitatively agree with the viscosity contour plots (Figure 5.14 and 5.15). Having a close look at Figure 5.16 suggests that flow fields in thixotropic liquid are closer to the moving spheres in comparison to Bingham liquid. Though both the spheres influence each others motion, they posses their own recirculation zones at either side.

The attraction of two spheres settling along the symmetry axis is observed in this study and this is in qualitative agreement with literature (Yu et al. [32], Gueslin et

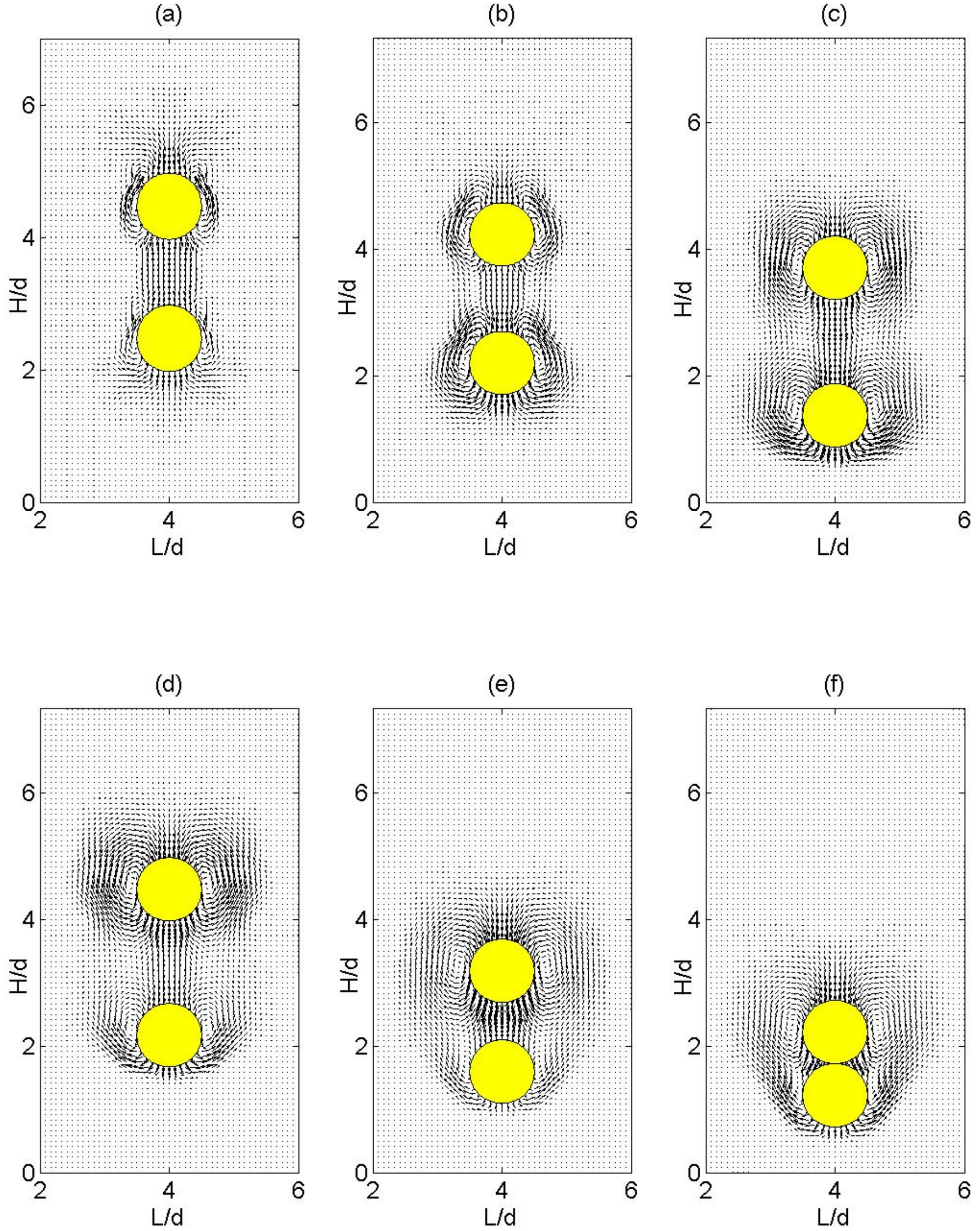

Figure 5.16: Velocity vectors of the two spheres settling in a thixotropic liquid at time periods (a) $t = 25000$, (b) $t = 28000$, (c) $t = 31000$, (d) $t = 33000$, (e) $t = 36000$ and (f) $t = 37800$; $Re = 2.25$.

al. [33]). Gueslin et al. [33] reported a lateral movement of settling spheres whenever a negative wake is observed in the flow field. Since the existence of negative wake has been largely reported in literature with liquids possessing elastic properties, it is not expected from our purely viscous model to exhibit negative wake. Therefore lateral movement not observed in our numerical experiments is not in disagreement with Gueslin et al. [33].

Bibliography

[1] M. S. Smoluchowski, On the practical applicability of Stokes' law of resistance, and the modifications of it required in certain cases, *5th Intern. Congr. Mathematicians*, 2 (1912) 192.

[2] M. Stimson, G. B. Jeffery, The motion of two spheres in a viscous fluid, *Proc. Roy. Soc. (London)*, A111 (1926) 110.

[3] H. Faxen, Die geschwindigkeit zweier kuglen, die unter einwirkung der schwere in einer zahen flussigkeit fallen, *Z. Angew. Math. Mech.*, 7 (1927) 79.

[4] J. Happel, H. Brenner, Low Reynolds number hydrodynamics, *Noordhoff International Publishing* (1973).

[5] G. J. Kynch, The slow motion of 2 or more spheres through a viscous fluid, *J. Fluid Mech.*, 5 (1959) 193.

[6] P. Mazur, W. van Sarloos, Many sphere hydrodynamics interactions and mobilities in a suspension, *Physica*, 115A (1982) 21.

[7] P. Ganatos, R. Pfeffer, S. Weimbaum, Numerical-solution technique for 3-dimensional Stokes flows, with application to motion of strongly interacting spheres in a plane, *J. Fluid Mech.*, 84 (1978) 79.

[8] G. K. Batchelor, Sedimentation in a dilute dispersion of spheres, *J. Fluid Mech.*, 119 (1982) 379.

[9] G. K. Batchelor, C. S. Wen, Sedimentation in a dilute polydisperse system of interacting particles, part 2. Numerical results, *J. Fluid Mech.*, 119 (1982) 495.

[10] B. Cichocki, B. U. Felderhof, R. Schmitz, Hydrodynamic interactions between two spherical particles, *Physiochemical Hydrodynamics*, 10 (1988) 383.

[11] M. S. Ingber, Numerical simulation of the hydrodynamic interaction between a sedimenting particle and a neutrally buoyant particle, *Int. J. Numer. Methods in Fluids*, 9 (1989) 263.

[12] T. Tran-Cong, T. N. Phan-Thien, Stokes problems of multiparticle systems: A numerical method for arbitrary flow, *Phys. Fluids A*, 1 (1989) 453.

[13] L. Durlofsky, J. F. Brady, Dynamic simulation of bounded suspensions of hydrodynamically interacting particles, *J. Fluid Mech.*, 200 (1989) 39.

[14] J. Happel, R. Pfeffer, The motion of two spheres following each other in a viscous fluid, *AIChE J.*, 6 (1960) 129.

[15] G. Kasper, T. Niida, M. Yang, Measurements of viscous drag on cylinders and chains of spheres with aspect ratios between 2 and 50, *J. Aerosol Sci.*, 16 (1985) 53.

[16] T. Kumagai, M. Muraoka, On the motion of spheres in a fluid at low Reynolds-numbers - (2 equal-sized spheres moving along their center lines), *JSME Inter. J. Series II*, 32 (1989) 309.

[17] E.H. Steinber, H. R. Pruppach, An experimental determination of drag on a sphere at low Reynolds numbers, *J. Applied Physics*, 39 (1968) 4129.

[18] G. H. Zheng, R. L. Powell, P. Stroeve, Settling velocities of two equal-sized spheres following each other in viscous fluids contained in cylinders, *Chem. Eng. Comm.*, 117 (1992) 89.

[19] S. Leichtberg, R. Pfeffer, S. Weinbaum, Stokes flow past finite coaxial clusters of spheres in a circular cylinder, *Int. J. Multiphase Flow*, 3 (1976) 147.

[20] F. Abraham, Functional dependence of drag coefficient of a sphere on Reynolds number, *Phys. Fluids*, 13 (1970) 2194.

[21] A. ten Cate, C. H. Nieuwstad, J. J. Derksen, H. E. A. Van den Akker, Particle imaging velocimetry experiments and lattice-Boltzmann simulations on a single sphere settling under gravity, *Phys. Fluids*, 14 (2002) 4012.

[22] B. T. Liu, S. J. Muller, M. M. Denn, Interactions of two rigid spheres translating collinearly in creeping flow in a Bingham material, *J. Non-Newtonian Fluid Mech.*, 113 (2003) 49.

[23] O. Merkak, L. Jossic, A. Magnin, Spheres and interactions between spheres moving at very low velocities in a yield stress fluid, *J. Non-Newtonian Fluid Mech.*, 133 (2006) 99.

[24] P. Jie, K. Zhu, Drag force of interacting coaxial spheres in viscoplastic fluids, *J. Non-Newtonian Fluid Mech.*, 135 (2006) 83.

[25] Z. Yu, A. Wachs, A fictitious domain method for dynamic simulation of particle sedimentation in Bingham fluids, *J. Non-Newtonian Fluid Mech.*, 145 (2007) 78.

[26] A. Potapov, R. Spivak, O. M. Lavrenteva, A. Nir, Motion and Deformation of Drops in Bingham Fluid, *Ind. Eng. Chem. Res.*, 45 (2006) 6985.

[27] J. P. Singh, M. M. Denn, Interacting two-dimensional bubbles and droplets in a yield-stress fluid, *Phys. Fluids*, 20 (2008) 040901-1.

[28] M. J. Riddle, C. Narvaez, R. B. Bird, Interactions between 2 spheres falling along their line of centers in a viscoelastic fluid, *J. Non-Newtonian Fluid Mech.*, 2 (1977) 23.

[29] Y. J. Liu, D. D. Joseph, Sedimentation of particles in polymer-solutions, *J. Fluid Mech.*, 255 (1993) 565.

[30] D. D. Joseph, Y. J. Liu, M. Poletto, J. Feng, Aggregation and dispersion of spheres falling in viscoelastic liquids, *J. Non-Newtonian Fluid Mech.*, 54 (1994) 45.

[31] G. Gheissary, B. H. H. A. Van den Brule, Unexpected phenomena observed in particle settling in non-Newtonian media, *J. Non-Newtonian Fluid Mech.*, 67 (1996) 1.

[32] Z. Yu, A. Wachs, Y. Peysson, Numerical simulations of particle sedimentation in shear-thinning fluids with a fictitious domain method, *J. Non-Newtonian Fluid Mech.*, 136 (2006) 126.

[33] B. Gueslin, L. Talini, B. Herzhaft, Y. Peysson, C. Allain, Aggregation behavior of two spheres falling through an aging fluid, *Physical Review E*, 74 (2006) 042501-1.

Chapter 6

Concluding remarks

6.1 Summary of results

The primary goal of this research project is to develop a direct simulating strategy for solving the motion of spherical particles in non-Newtonian liquids under the influence of gravity and validate the simulation tool with available experimental/numerical data of single/multi sphere sedimentation. We develop the simulating strategy step by step, first validating the simulation tool for single phase and then proceeding to two phase systems (solid-liquid). The summary of results is given in pointwise manner starting from single phase to two phase systems.

6.1.1 Single phase results

- The channel flow test is done with Bingham liquid and profile of steady state velocity at the center of channel is obtained through simulation. The result obtained through simulation is found in excellent agreement with the analytical solution.

- In the case of lid driven cavity flow with Bingham liquid, the flow is governed by the yield stress of the liquid at low Reynolds number. Primary quantities of interest, position of primary vortex and vortex intensity at vortex centers, are distinct functions of Bingham number (i.e. yield stress of liquid). At high Reynolds number, the flow behavior is different due to the high inertial forces. However as the yield stress inceases, inertial effects are softened and behavior shows the similar trend as observed with low Re.

- The flow evolution of thixotropic liquid in a lid driven cavity is studied with two different Deborah numbers ($Db = 0, 1$). As Deborah number increases, the liquid time scale ($1/k_2$) also increases resulting in slower flow response. Position of primary vortex and vortex intensity at vortex centers, are distinct functions of pseudo Bingham number. The results obtained with thixotropic liquid ($Db = 1$) at low Reynolds number were compared to pseudo Bingham rheology ($Db = 0$) and variations in position of primary vortex and vortex intensity were consistent with theoretical explanations.

6.1.2 Two phase (single sphere sedimentation) results

- The terminal velocity of a sphere, settling in a finite size container, is influenced by the retardation effects due to walls. In study with Newtonian liquid, the wall factors are determined for settling of a sphere in cylinders of different square cross-sections at low Reynolds number. As the walls come closer to settling sphere, its terminal velocity decreases due to the increasing retardation effects.

- The interaction of a sphere with Bingham liquid at low Reynolds number is strongly affected by the yield stress of the liquid. The drag force calculated in case of Bingham flow past a fixed sphere increases with increase of yield stress. Similarly terminal velocity of a sphere settling in Bingham liquid is a distinct function of liquid's yield stress. It decreases with the increase of yield stress.

- In study with thixotropic liquid, we examine the effect of aging and Reynolds number on the sedimentation of single sphere.

- The settling velocity of a sphere depends upon the age of liquid. It decreases with liquid's age as the liquid gains higher network strength with time. A heavy particle settles faster in comparison to a lighter particle. Higher inertial forces (higher Re) soften the aging effects of liquid which results in increased settling velocity. Irrespective of liquid's age and Reynolds number, the fore-aft symmetry is found to be broken at creeping flow of a sphere in thixotropic liquid.

6.1.3 Two phase (two sphere sedimentation) results

- In study with Newtonian liquid, the hydrodynamic interaction between the spheres increases with decrease in separation distance between their centers at low Reynolds number. The spheres maintain a constant distance and move with equal settling velocity which is always equal or greater (depending upon the separation distance between two spheres) than the settling velocity of single sphere sedimenting in same conditions.

- Two spheres (one above the other) sedimenting in a Newtonian liquid at moderate Reynolds number were found to attract each other due to the interaction of trailing sphere with the wake of leading sphere.

- Low Reynolds number study of two sphere sedimentation in Bingham liquid suggests the increased hydrodynamic interaction with decrease in separation distance between their centers. There exists an unyielded region between the two spheres due to which the spheres do not approach each other. The spheres move with equal settling velocity which is always equal or greater (depending upon the separation distance between two spheres) than the settling velocity of single sphere sedimenting in same conditions.

- With the increase of inertial forces (higher Re), the unyielded region between the two spheres sedimenting in Bingham liquid vanishes and due to the interaction with wake, the trailing sphere approaches the leading sphere.

- In study with thixotropic liquid, an intriguing behavior is observed in which the leading sphere moves faster than the trailing sphere. This effectively increases the separation distance beween the spheres. This behavior is due to the yield effects of thixotropic liquid. After a certain time period, the leading sphere decelerates while the trailing sphere starts accelerating due to the memory and shear-thinning behavior of thixotropic liquid. Finally the trailing sphere approaches the leading sphere irrespective of the Reynolds number. This peculiar behavior helps in demonstrating the aging, yield, memory and shear-thinning behavior of thixotropic liquid in a single experiment.

6.2 Future directions

In Chapter 5, we have demonstrated the drafting and kissing of two spheres sedimenting in thixotropic liquid. It would be interesting to implement a collision model which allows for a proper resolution of particle-particle interaction and then examine the tumbling behavior of the two spheres whether they aggregate or not. Another interesting case study would be to investigate the hydrodynamic interaction between two particles initially placed side by side along the mid-plane.

The hydrodynamic interaction between more than two particles is a desirable condition to asses the role of multi-particle interactions on the settling velocity. Therefore it is required to carry out the simulations with more than two particles with different orientations. Further as a generalization of numerical tool, various particle shapes can be considered and the impact of their hydrodynamic interactions over the setting velocity can be determined.

Appendix A

Simulation procedure

The simulation procedure, based on the formulation of lattice-Boltzmann scheme given by Eggels and Somers [1], is timeloop of following sequential steps considering Equation 2.15.

- Determine solution vector $\beta_k^-(\mathbf{x},t)$ from the known distribution of dimensionless mass densities N_i, using the inverse of matrix E (E^I).

$$\beta_k^-(\mathbf{x},t) = \sum_{i=1}^{n} E_{ki}^I N_i(\mathbf{x} - \tfrac{1}{2}\mathbf{c_i}, t - \tfrac{1}{2}) \qquad \text{(A.1)}$$

- Determine β_k^+ from β_k^- using the difference between the two vectors which is known. The third-order terms displayed in Equation 2.17 are manipulated in such a way that $T_s^+ = -\gamma_3 T_s^-$ ($s = 1.....6$) where γ_3 is a relaxation factor of order unity ($\gamma_3 = 0.8$ in present work). This approach is used to suppress the deviation caused by third-order terms. Since the magnitudes of fourth-order terms are small, we impose $F_{1,2}^+ = 0$ in simulations. The solution vector β_k^+ now reads as

$$\beta_k^{+}(\mathbf{x},t) = \begin{bmatrix} \rho,\ \rho u_x + \frac{1}{2}f_x,\ \rho u_y + \frac{1}{2}f_y,\ \rho u_z + \frac{1}{2}f_z, \\ \rho(u_x u_x) + \rho(\dfrac{+1-6\nu}{6})(2\partial_x u_x), \\ \rho(u_x u_y) + \rho(\dfrac{+1-6\nu}{6})(\partial_x u_y + \partial_y u_x), \\ \rho(u_y u_y) + \rho(\dfrac{+1-6\nu}{6})(2\partial_y u_y), \\ \rho(u_x u_z) + \rho(\dfrac{+1-6\nu}{6})(\partial_x u_z + \partial_z u_x), \\ \rho(u_z u_y) + \rho(\dfrac{+1-6\nu}{6})(\partial_z u_y + \partial_y u_z) \\ \rho(u_z u_z) + \rho(\dfrac{+1-6\nu}{6})(2\partial_z u_z) \\ -\gamma_3 T_1^{-}, -\gamma_3 T_2^{-}, -\gamma_3 T_3^{-}, -\gamma_3 T_4^{-}, -\gamma_3 T_5^{-}, -\gamma_3 T_6^{-}, 0, 0 \end{bmatrix} \tag{A.2}$$

- Determine the distribution of dimensionless mass densities $N_i(\mathbf{x} + \frac{1}{2}\mathbf{c_i}, t + \frac{1}{2})$ with the help of Equation 2.15.

- Impose boundary conditions (see appendix B and C).

- Shuffle dimensionless mass densities such that $N_i(\mathbf{x} + \frac{1}{2}\mathbf{c_i}, t + \frac{1}{2})$ associated with position $\mathbf{x}$ becomes $N_i(\mathbf{x} - \frac{1}{2}\mathbf{c_i}, t - \frac{1}{2})$ associated with position $\mathbf{x} + \mathbf{c_i}$ for the next time step.

- Solve scalar transport equation for thixotropic liquids

$$\frac{\partial \lambda}{\partial t} + u_i \frac{\partial \lambda}{\partial x_i} = -k_1 \dot{\gamma} \lambda + k_2 (1 - \lambda) \tag{A.3}$$

The discrete version of this equation is written using Euler explicit scheme. Right hand side is treated semi-implicitly.

$$\frac{\lambda^{(t+1)} - \lambda^{(t)}}{\triangle t} + \left(u_i \frac{\partial \lambda}{\partial x_i} \right)^{t} = -k_1 \dot{\gamma}^{(t)} \lambda^{(t+1)} + k_2 (1 - \lambda^{(t+1)}) \tag{A.4}$$

The network parameter λ is associated with apparent dynamic viscosity of thixotropic liquid μ_a as

$$\mu_a = \mu_\infty (1 + \alpha \lambda) \tag{A.5}$$

The apparent kinematic viscosity ν_a, determined by expression μ_a/ρ, is used to calculate various elements of solution vector β (Equation A.2) with $\nu = \nu_a$.

- Apply external force on the liquid.
- Update velocity of the solid sphere(s) using force balance expression

$$m\frac{d\mathbf{v}}{dt} = \sum \mathbf{F} \tag{A.6}$$

with m being the net mass of sphere, $\mathbf{v}$ is velocity vector of sphere, and $\sum \mathbf{F}$ is the net force vector acting on the sphere. In our simulations, a sphere geometry is defined by control points (surface of sphere) and the sphere contains liquid inside. The net mass of sphere in presence of internal liquid is given by notion

$$m = (\rho_s - \rho_l)V \tag{A.7}$$

where ρ_s is the density of solid sphere, ρ_l is the density of liquid and V is the volume of sphere. The velocity of a sphere is obtained by writing Equation A.6 in discrete form as

$$\mathbf{v}(t) = \mathbf{v}(t-1) + \triangle t[\frac{\mathbf{F_{ext}} + \mathbf{F_b} + \mathbf{F_h}}{(\rho_s - \rho_l)V}] \tag{A.8}$$

$\mathbf{F_{ext}}, \mathbf{F_b}, \mathbf{F_h}$ are the external force (e.g. gravity), buoyancy force and hydrodynamic force vectors, respectively,

- Update position of the solid sphere(s).

$$\mathbf{P}(t) = \mathbf{P}(t-1) + \mathbf{v}(t)\triangle t \tag{A.9}$$

$\mathbf{P}$ is the position vector of center of solid sphere.

Appendix B

Boundary condition for a curved geometry

Bounce-back boundary condition is a general scheme to approximate the no-slip boundary condition at a solid boundary. However, to obtain a satisfactory approximation of no-slip boundary condition using bounce-back scheme, it is required that bounce-back collision takes place at the location one-half lattice spacing ($\Delta = \frac{1}{2}$) outside of a boundary node. The implementation of this technique is straightforward with simple boundaries parallel to the lattice grid. However for a curved geometry, placing the boundary halfway between the lattice nodes will change the actual geometry. To overcome this problem, Derksen et al. [2] developed a method for Eggels and Somers LB scheme to simulate the spheres on a cubic grid. This method is known as adaptive force-field technique and based on work by Goldstein et al. [3].

In this method the geometry of a sphere at time t is represented by a set of M control points $\mathbf{r}_j(t)$ $(j = 1, 2, ...M)$. These points do not coincide with lattice nodes necessarily and can be anywhere in the lattice grid (see Figure B.1 for a $2D$ representation). The velocity of control points $\mathbf{v}_j(t)$ is calculated using the translational and rotational velocities of sphere. For a no-slip boundary condition, the velocity of liquid (at control points) should be the same as that of control points. The difference $\mathbf{d}_j(t)$ between the velocities of a control point and liquid velocity at control point is computed

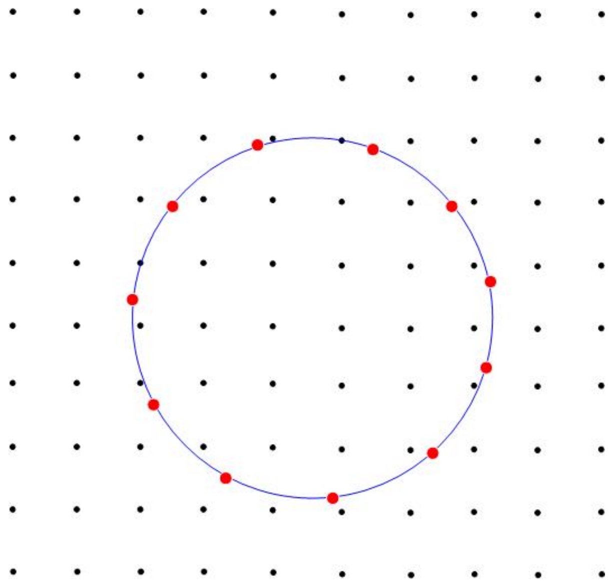

Figure B.1: $2D$ representation of a sphere defined by a set of control points (red dots) on top of a cubic grid (black dots)

by the expression

$$\mathbf{d}_j(t) = \mathbf{v}_j(t) - \sum_{1}^{k} c_k \mathbf{u}_k(t) \tag{B.1}$$

where the sum represents an interpolation of the liquid velocity of nearby lattice points weighted by coefficients c_k which are different for every control point.

For a satisfactory implementation of no-slip boundary condition, the difference $\mathbf{d}_j(t)$ should be as least as possible. To reduce $\mathbf{d}_j(t)$, a force is applied on the fluid at points near the curve boundary using force vector $\mathbf{f}(\mathbf{x}, t)$ which is already included in lattice-Boltzmann scheme. This force is determined by the expression

$$\mathbf{f}_k(t) = \phi \mathbf{f}_k(t-1) + \psi \sum_{1}^{j} c_j \mathbf{d}_j(t) \tag{B.2}$$

The constants ϕ and ψ are relaxation factors which determine how fast the difference is reduced. The default values of these relaxation factors used in present work are $\phi = 0.95$ and $\psi = 1.8$.

Appendix C

Boundary condition for cylinder walls

In present work, square cylinders with varying dimensions are used as containers to study the sedimentation of spherical particles. To consider a cylinder effectively a closed container, all of its walls should be stationary (i.e. zero velocity) with no-slip condition. This can be achieved by imposing bounce-back boundary condition at walls. However during the initial stages of this work, the results obtained with single sphere sedimentation in Bingham liquid having bounce-back boundary conditions deviated a lot from literature. Therefore an alternative method is employed to obtain the satisfactory results with desired boundary conditions.

A 2D projection of 3D grid is displayed in Figure C.1. The physical wall (dotted line) is considered at one-half lattice spacing ($\triangle$) outside of actual flow domain (black dots). The lattice-Boltzmann scheme used in present work contains a solution vector β consisting $n = 18$ elements ($D3Q18$ scheme) which are various properties of liquid. In order to explain conveniently, here we consider $D2Q9$ scheme (shown in Figure C.2) for 2D grid. Now solution vector β contains 9 elements out of which $2nd$ and $3rd$ elements of solution vector treats the velocities in x and y directions, respectively. While programming in Fortran, the structure of solution vector reads as β: $beta(q, i, j)$ where q runs from 1 to 9. We explicitly set the velocities (linked to $2nd$ and $3rd$ elements of

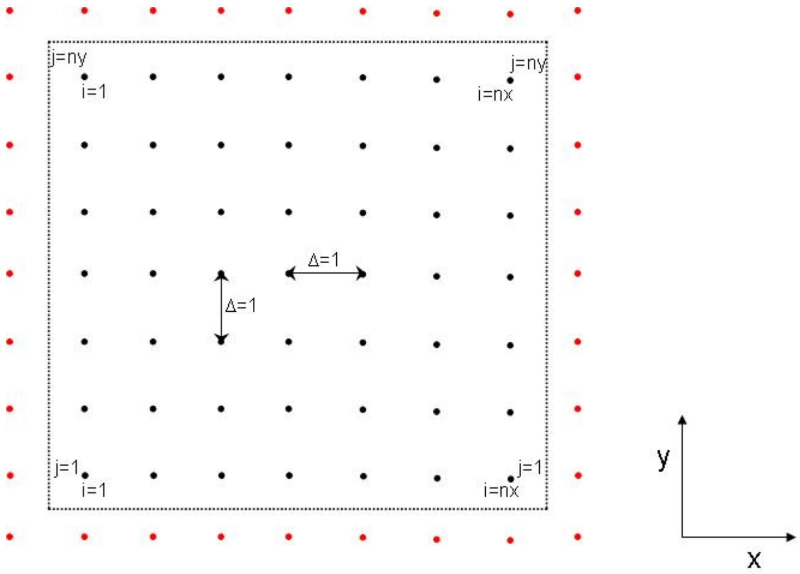

Figure C.1: $2D$ projection of a $3D$ cubic grid; black dots represent actual flow domain; red dots are virtual points; dotted lines denote physical walls.

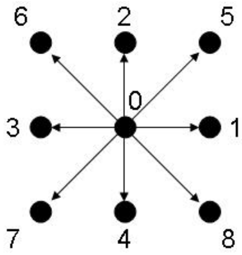

Figure C.2: D2Q9 scheme

β) zero at four boundaries of flow domain (shown by Figure C.1) by doing following operation

```
do j=1,ny
    i=1
    beta(2,i,j)=0
    beta(3,i,j)=0
    i=nx
    beta(2,i,j)=0
    beta(3,i,j)=0
enddo
```

```
do i=1,nx
    j=1
    beta(2,i,j)=0
    beta(3,i,j)=0
    j=ny
    beta(2,i,j)=0
    beta(3,i,j)=0
enddo
```

with nx and ny being the number of grid points of flow domain in x and y directions, respectively. In order to obtain the zero velocity at physical walls, the virtual points (red dots) outside of physical walls are used to apply the zero gradient condition over mass density vector $\mathbf{N}$ at walls such that

$$\frac{d\mathbf{N}}{d\hat{\mathbf{n}}}|_{wall} = 0 \tag{C.1}$$

where $\hat{\mathbf{n}}$ is the unit normal vector. In perspective of Figures C.1 and C.2, Equation C.1 is coded as

```
do j=1,ny
    i=0
    beta(6,i,j)=beta(6,i+1,j)
    beta(3,i,j)=beta(3,i+1,j)
    beta(7,i,j)=beta(7,i+1,j)
    i=nx+1
    beta(5,i,j)=beta(5,i-1,j)
    beta(1,i,j)=beta(1,i-1,j)
    beta(8,i,j)=beta(8,i-1,j)
enddo


do i=1,nx
```

```
    j=0
    beta(7,i,j)=beta(7,i,j+1)
    beta(4,i,j)=beta(4,i,j+1)
    beta(8,i,j)=beta(8,i,j+1)
    j=ny+1
    beta(6,i,j)=beta(6,i,j-1)
    beta(2,i,j)=beta(2,i,j-1)
    beta(5,i,j)=beta(5,i,j-1)
enddo
```

Bibliography

[1] J. G. M. Eggels, J. A. Somers, Numerical simulation of free convective flow using the lattice-Boltzmann scheme, *Int. J. Heat fluid flow*, 16 (1995) 357.

[2] J. Derksen, H. E. A. Van den Akker, Large eddy simulations on the flow driven by a rushton turbine, *AIChE Journal*, 45 (1999) 209.

[3] D. Goldstein, R. Handler, L. Sirovich, Modeling a no-slip boundary with an external force field, *J. Comp. Physics*, 105 (1993) 354.